ADVANCED ELECTRONIC MATERIALS
www.advelectronicmat.de

2D WS_2: From Vapor Phase Synthesis to Device Applications

Changyong Lan, Chun Li,* Johnny C. Ho, and Yong Liu*

The discovery of graphene has triggered the research on 2D layer structured materials. Among many 2D materials, semiconducting transition metal dichalcogenides (TMDs) are widely considered to be the most promising ones due to their excellent electrical and optoelectronic characteristics. Tungsten disulfide (WS_2) is a kind of such TMDs with fascinating properties, such as the high carrier mobility, appropriate band gap, strong light–matter interaction with the large light absorption coefficient, very large exciton binding energy, large spin splitting, and polarized light emission. All these interesting properties can make the 2D WS_2 being highly favorable for applications in memristors, light-emitting devices, optical modulators, and many others. Here, the comprehensive review on the properties, vapor phase synthesis, electronic and optoelectronic applications of 2D WS_2 is presented. This review does not only serve as a design guideline to elevate the material quality of 2D WS_2 films via enhanced synthesis approaches, but also provides valuable insights to various strategies to improve their device performances. With the fast development of wafer-scale synthesis methods and novel device structures, 2D WS_2 can undoubtedly be a rising star for the next-generation devices in the near future.

1. Introduction

The rising of 2D materials research is ignited by the discovery of graphene, a one-atom-thick carbon sheet, in 2004.[1] Due to the excellent physical and chemical properties of 2D materials, they become a hot topic in many disciplines, such as physical science, chemical science, materials science, and engineering.[2–4] Until now, there are already a large number of 2D materials developed, including graphene,[1] transition metal dichalcogenides (TMDs),[5] black phosphorene,[6] Germanane,[7,8] GeTe,[9] 2D covalent organic frameworks,[10] etc. In theory, it is predicted to have more than 5000 different kinds of 2D materials,[11] which cover a wide range of material categories in insulators, semiconductors, semimetals, metals, superconductors, etc., making them possible to construct various 2D materials devices with novel functions. Particularly, graphene is the most intensively studied material. Although it possesses superior properties with the large carrier mobility,[12,13] flat light absorption in a wide spectrum,[14,15] and strong mechanical strength,[16,17] the lack of a band gap would greatly limited its applications in electronics and optoelectronics. For example, transistors made from graphene cannot be effectively turned off,[1] while graphene-based photodetectors always have a substantially large dark current.[18] In this case, semiconducting 2D materials with suitable band gaps, rather than graphene, are highly desired for high-performance electronic and optoelectronic devices.

Among many semiconducting 2D materials, TMDs are the most promising alternatives because of their appropriate band gaps, good stability in ambient, excellent electrical, and optoelectronic characteristics.[19–21] WS_2 is one of the TMD materials that has superior properties as compared with other TMDs. It has the relatively high carrier mobility,[22] large exciton binding energy,[23] large spin–orbit splitting,[24] and strong photoluminescence (PL).[25] These properties make it idle for a wide range of applications, such as transistors,[26] photodetectors,[27] light-emitting devices (LEDs),[28] etc. Despite the fact that there are numerous reports focused on the synthesis, properties, and applications of 2D WS_2, there is still a lack of the comprehensive review on 2D WS_2. In this review article, we would focus on the vapor phase synthesis, property assessment, and electronic and optoelectronic applications of 2D WS_2. At first, the fundamental properties of 2D WS_2 are introduced in details. Then,

Prof. C. Lan, Prof. C. Li, Prof. Y. Liu
State Key Laboratory of Electronic Thin Films and Integrated Devices
University of Electronic Science and Technology of China
Chengdu 610054, China
E-mail: cylan@uestc.edu.cn; lichun@uestc.edu.cn
Prof. C. Lan, Prof. C. Li, Prof. Y. Liu
School of Optoelectronic Science and Engineering
University of Electronic Science and Technology of China
Chengdu 610054, China
Prof. C. Li
Wuhan National Laboratory for Optoelectronics
Huazhong University of Science and Technology
Wuhan 430074, China
Prof. J. C. Ho
Department of Materials Science and Engineering
City University of Hong Kong
Hong Kong 999077, China
Prof. J. C. Ho
Key Laboratory of Advanced Materials Processing & Mold
(Zhengzhou University)
Ministry of Education
Zhengzhou University
Zhengzhou 450002, China
The ORCID identification number(s) for the author(s) of this article can be found under https://doi.org/10.1002/aelm.202000688.

DOI: 10.1002/aelm.202000688

various kinds of wafer-scale synthesis methods of 2D WS_2 are presented with the emphasis on vapor phase techniques. Subsequently, the device applications of 2D WS_2 on different electronic and optoelectronic applications would be thoroughly discussed, followed by the challenges and future opportunities compiled in the community. With the rapid development of these materials, this review can provide significant insights to further extend the novel 2D WS_2 devices into practical applications in the near future.

2. Properties

WS_2 is a kind of 2D TMD materials that has many interesting physical properties, such as the transition of indirect to direct band gap at a single-layer limit, layer-dependent band gap, large exciton binding energy, strong spin–orbit splitting, valley selection rule, etc. As a result, WS_2 has promising potentials for a wide range of applications in transistors, diodes, LEDs, photodetectors, pulsed lasers, and many others.

2.1. Crystal Structure

As shown in **Figure 1**a, WS_2 has a layered crystal structure.[29] In the structure, each layer consists of three atomic planes. Each of the atomic planes has the hexagonally packed atoms (Figure 1b), where the W metal atom plane is sandwiched between two planes of S atoms, forming the S-W-S structure. The distance between each layer is about 0.65 nm. There are no dangling bonds existed on the surfaces of each layer, which makes the surface very stable and nonreactive. These layers are hold together by van der Waals interaction. Due to the weak interlayer van der Waal interaction, the WS_2 crystal can be mechanically exfoliated by scotch tape. The stable coordination of W is trigonal prismatic as given in Figure 1c, which is the case for 2H phase WS_2 (for single layer, it is 1H phase). While it can also have the octahedral coordination (Figure 1d), which can be seen in the meta-stable 1T phase

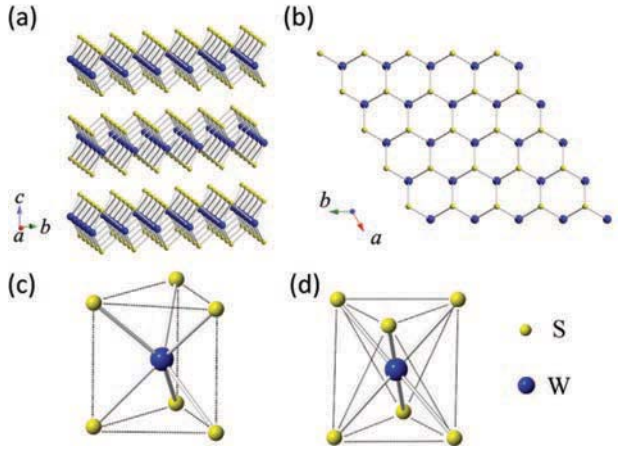

Figure 1. Crystal structure of WS_2. a) Schematic view of the layered structure. b) Schematic view from the *c*-axis. c) Unit cell of the trigonal prismatic structure. d) Unit cell of the octahedral structure.

WS_2. Due to the stacking difference and lattice distortion, other polymorphs are formed. Detailed discussion about the polymorphs can be found elsewhere.[30] The crystal lattice of 2H WS_2 belongs to the nonsymmorphic hexagonal space group $P6_3/mmc$ (D^4_{6h}) that has the space inversion symmetry.[31] The unit cell of 2H WS_2 is extended over two layers with the S atoms of the second layer sitting on top of the W atoms of the first layer and vice versa. When 2H WS_2 is thinned down to a single layer, the unit cell of which would contain only one layer, known as 1H WS_2. Monolayer 1H WS_2 (the "1H" term will be omitted for the following discussion) is composed of one S-W-S stacking unit, which has a threefold rotational axis, i.e., *c*-axis. The W atoms plane would become the mirror plane for single-layer WS_2. The crystal lattice of monolayer WS_2 belongs to $P\bar{6}m2(D^1_{3h})$.[31] As compared with the bulk WS_2, monolayer counterparts lack of the space inversion symmetry. Furthermore, it can be inferred that even layer-number WS_2 has the space inversion symmetry while odd layer-number WS_2 lacks of the space inversion symmetry from the crystal structure.

2.2. Layer-Dependent Band Structure, Band Gap, and PL

Similar to other types of semiconducting TMDs, WS_2 shows a layer-number-dependent band structure as presented in **Figure 2**a.[32] In fact, monolayer WS_2 has a direct band gap. The conduction band minimum (CBM) and the valance band maximum (VBM) are both located at K point. When the layer number of WS_2 increases, the VBM shifts to Γ point, while the CBM locates between K and Γ points (called Q point). In addition, the band gap value would decrease with the increase of the layer number (Figure 2b).[33] The band edge states at K_c and K_v (the subscripts c and v stand for the K point at conduction and valance band, respectively) have dominant contributions from the W $d_{x^2-y^2}$, d_{xy}, and d_{z^2} orbitals with an admixture of the S p-orbitals.[24] For the states at Q_c and Γ_v, the contribution from the S p_z orbitals become significant, which plays an important role for the transition from direct to indirect band gap from monolayer to bilayer and multilayer. The close distance between S p_z orbitals from neighboring layers leads to the large hopping that significantly changes the energy of Q_c and Γ_v.[34] Thus, the transition from a direct band gap (monolayer WS_2) to an indirect band gap (bilayer and multilayer WS_2) is a consequence of the interlayer hopping.[35]

Due to the large spin–orbit coupling (SOC), the valance band near the K point shows a large spin–orbit splitting (≈400 meV, Figure 2a).[24,32,36] The spin–orbit splitting near the K_v point is dominated by the W d_{xy} and $d_{x^2-y^2}$ orbitals, which are largely localized in individual layers.[37] Because of the low interlayer hopping of orbitals, the spin–orbit splitting energy has little changes with the layer number. It should be noted that the splitting of the VBM of monolayer is purely associated with the spin–orbit effect and the lack of inversion symmetry, while the same splitting for bilayer is caused by the combination of the interlayer interaction and SOC.[35]

In this fashion, the indirect-to-direct transition of the band structure would lead to the strong PL in monolayer WS_2 as depicted in the inset of Figure 2c.[32] With the decreasing

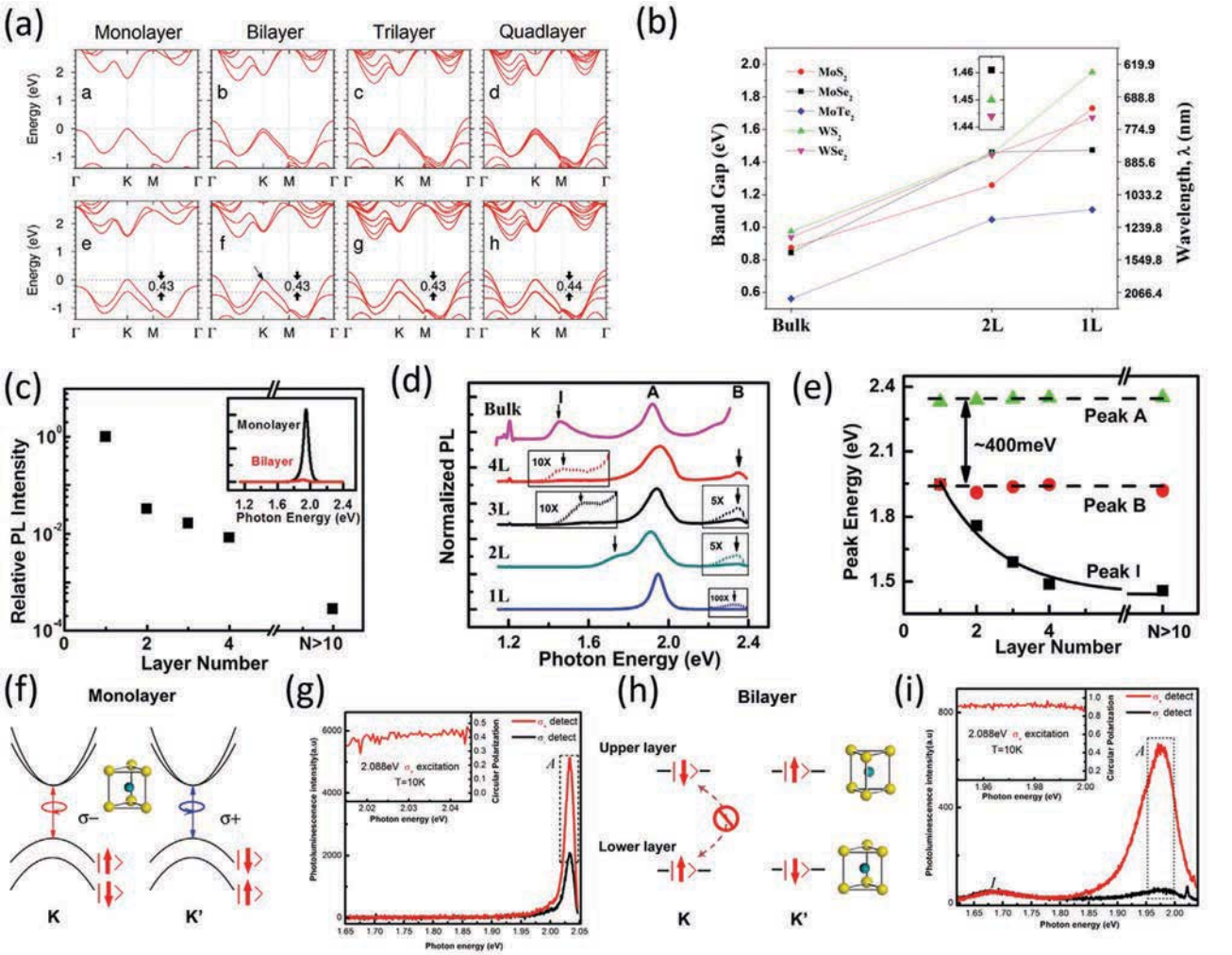

Figure 2. Layer-dependent band structure and related optical properties of WS_2. a) Layer-dependent band structure without and with the spin–orbit coupling. b) Layer-dependent band gap. c) Layer-dependent PL intensity. d) Layer-dependent PL spectra. e) Layer-dependent PL peak positions. f) Valley-dependent optical selection rule for monolayer WS_2. g) Polarized PL spectra of monolayer WS_2. h) Spin-layer-valley coupling in bilayer WS_2. i) Polarized PL spectra of bilayer WS_2. a) Reproduced with permission.[32] Copyright 2013, Springer Nature. b) Reproduced with permission.[33] Copyright 2012, American Physical Society. c–e) Reproduced with permission.[32] Copyright 2013, Springer Nature. f–i) Reproduced with permission.[38] Copyright 2014, National Academy of Sciences.

layer number of WS_2, the PL intensity from direct interband transition increases dramatically and reaches the maximum with monolayer WS_2, where the intensity is more than three orders of magnitude stronger than that from the bulk (Figure 2c). The PL intensity is about one order of magnitude higher than that from the bilayer counterparts (Figure 2c inset). Except PL emission from the direct transition at K point (A exciton), the weak PL peak (B) is also observed at the higher energy (Figure 2d). The splitting between the A and B peaks is almost the same for different layer numbers of WS_2 (Figure 2e) with a value of about 400 meV. The A and B emissions are a result of valance band splitting at the K points arising mainly from SOC.[32,36] The peak originating from the indirect band gap transition (I peak) shifts gradually toward the higher energy and fades to null at the monolayer limit, being consistent with theoretical result.[32]

Attributed to the giant SOC, the VBM of monolayer WS_2 shows the spin index locked with the valley index, i.e., valley K (–K) has only the spin up (down) electrons, leading to the valley-dependent optical selection rules (Figure 2f). The rule dictates that the photoexcitation is able to selectively excite the ±K valley electrons from the spin-polarized bands with the circularly polarized light.[38,39] Actually, the polarization-resolved PL spectrum can reflect the optical selection rule (Figure 2g), where the monolayer WS_2 exhibits polarization dichroism under the circular polarized light excitation. Owing to intervalley scattering, the PL is not fully polarized.[38] The large spin–valley coupling strength in WS_2 (≈0.4 eV) is significantly higher than the interlayer hopping energy (≈0.1 eV), which induces the suppressed interlayer coupling at K and K' (–K) valleys (Figure 2h).[38] As a result, bilayer WS_2 can be regarded as the decoupled layers, leading to polarized light emission when excited by the circular polarized light excitation (Figure 2i).

2.3. Doping- and Strain-Dependent PL of Monolayer WS_2

The light emission from monolayer WS_2 can be effectively tuned by electrical doping. As presented in **Figure 3**a, the PL spectra measured from a field-effect transistor (FET) made with exfoliated monolayer WS_2 channel exhibit an obvious gate-dependent characteristic.[40] In fact, the emission consists of two components, namely, the low energy and the high energy peaks, assigned to an exciton (X_A) and a negative trion (X_A^-), respectively. When the gate voltage sweeps from negative to positive, the peak position of X_A^- would exhibit a red shift while the X_A one slightly blueshifts (Figure 3b). This way, the energy difference between X_A and X_A^- increases. The energy difference is defined as the dissociation energy of trion, which consists of the trion binding energy (E_{tb}, a constant) and the Fermi energy (E_f).[40] In this case, the increase of the dissociation energy of trion with electron doping is mainly due to the rise of Fermi energy (Figure 3b). On the other hand, the exciton energy is defined as the difference between band gap and exciton binding energy, which shows a blueshift with increasing electron doping. This shift is attributed to the decrease of exciton binding energy with electron doping. Furthermore, the overall integrated intensity and intensity of X_A decrease with the increasing electron doping, but the intensity of X_A^- first increases from −40 to 0 V, then remains stable between 0 and 30 V, and finally decreases after 30 V (Figure 3c). Because the PL spectrum evolution is basically due to interconversion between neutral exciton and trion by modulating the doping-induced carrier density,[41] the PL spectrum of monolayer WS_2 can also be tuned by the excitation light power, i.e., optical doping.[40] As shown in Figure 3d, the overall emission band profile evolves from two-component feature at low excitation powers into a single peak at high powers. The variation is mainly ascribed to the photo-induced electron doping.[40]

At the same time, the density functional theory (DFT) calculation indicates that monolayer WS_2 undergoes a transition from direct to indirect band structure when the in-plane strain is larger than 2.6%.[42] This transition would affect the PL spectrum of monolayer WS_2. To be specific, the PL emission shows a redshift with almost unchanged line shape with the increase of the strain. The broadening of the emission occurs when the stain reaches 2.5%. Then, the emission continues to broaden and redshift with increasing the stain. This broadening is caused by the appearance of indirect band gap emission (I peak). The I peak intensity tends to increase with the stain, whereas the excitonic X_A and X_A^- peaks decrease with the strain. Both the X_A, X_A^-, and I peak energies exhibit a linear redshift with the strain. The I and X_A peaks do not converge at the strain of 2.5% (near the threshold for direct-to-indirect band structure transition), which is in contrast with the expectation. This discrepancy is caused by the larger exciton binding energy of the indirect transition as compared with the direct one.[42] The trion dissociation energy decreases with the increase of the strain. The increase of strain can reduce the effective exciton mass and enlarge the polarizability,[43] leading to the reduction of the trion dissociation energy.[44]

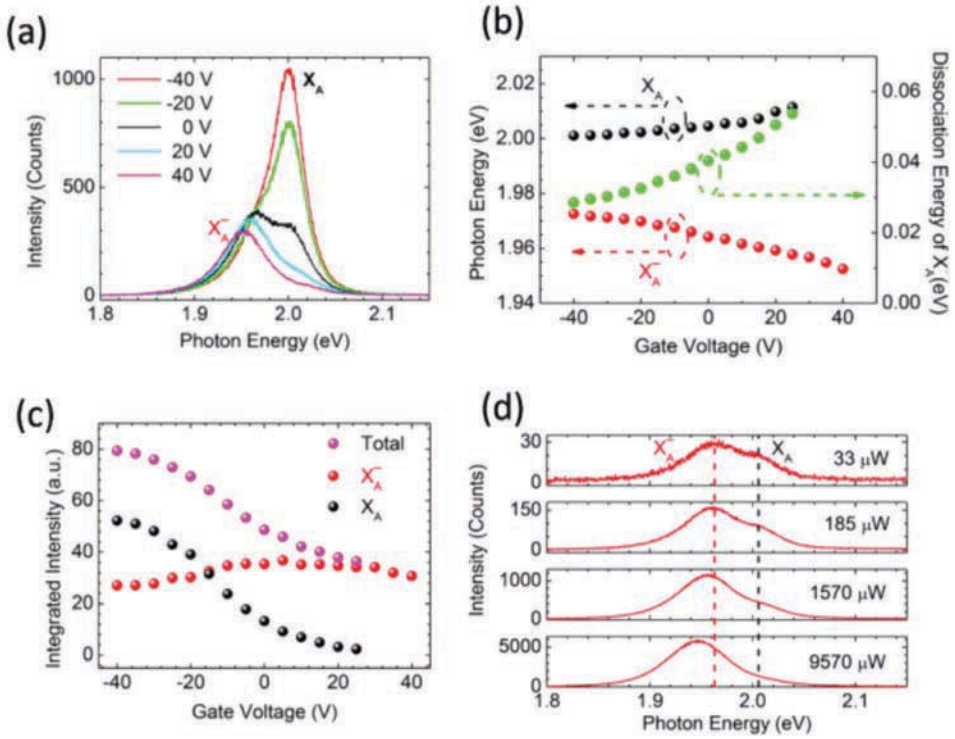

Figure 3. Doping- and strain-dependent PL of monolayer WS_2. a) PL spectra under different gate voltages. b) Excitonic emission peak energies and dissociation energies of trion as a function of gate voltage. c) Integral intensity of the excitonic peaks as a function of gate voltage. d) PL spectra under different excitation powers. Reproduced with permission.[40] Copyright 2015, American Chemical Society.

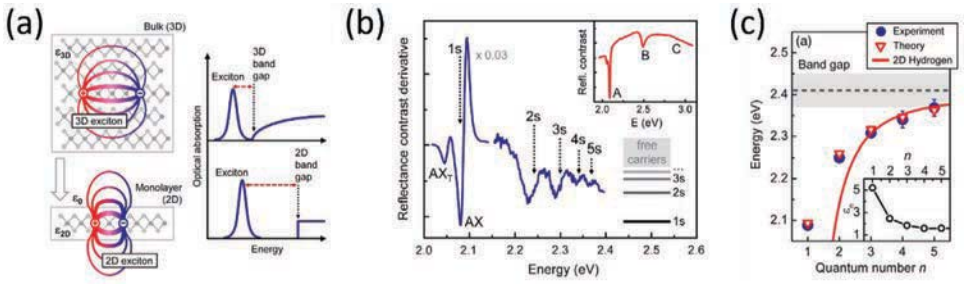

Figure 4. Exciton binding energy. a) Schematic of the exciton and related absorption spectrum in bulk and 2D materials. b) Derivative of the reflectance contrast spectrum. Inset shows the reflectance contrast spectrum. c) Experimental and theoretical transition energies of the exciton states. Reproduced with permission.[45] Copyright 2014, American Physical Society.

2.4. Exciton Binding Energy

The excitons in 2D WS_2 are very different from the ones in bulk materials. Actually, the electron and hole forming an exciton in monolayer WS_2 are strongly confined to the plane of the monolayer.[45] In addition, the electron and hole experience the reduced screening due to the change in dielectric environment (**Figure 4**a). These effects have two major implications. One is that the quasi-particle band gap is expected to increase for monolayer WS_2. Another is that the enhanced electron–hole interaction is anticipated to increase with the exciton binding energy (Figure 4a).[45] Owing to the dielectric confinement, the exciton binding energy in monolayer WS_2 is much larger than that of conventional materials. In order to determine the exciton binding energy in monolayer WS_2, Chernikov et al. studied the Rydberg series of exciton X_A.[45] The derivative of the reflectance contrast spectrum of the monolayer WS_2 is used to determine the positions of excited states (n = 1, 2, 3, etc.) of the bound electron–hole pairs (Figure 4b). Hydrogen model is then employed to fit the measured data. However, for the low n number (n = 1 and 2), the data cannot be fitted well due to the more strongly screened electron–hole interaction at the short range. For n = 3–5, the data can be fitted perfectly due to the weakly screened electron–hole interaction at the long range, from which a quasi-particle band gap of 2.41 eV is obtained (Figure 4c). By subtracting the 1s transition energy (2.09 eV), an exciton binding energy of 0.32 eV is determined.

For the case of WS_2, it is also noted that each excitonic state has a specific parity, which the incident photons can excite. In other words, the one-photon excitation only induces the even parity excitonic states (i.e., bright excitons), while the two-photon excitation causes the odd parity excitonic states (i.e., dark excitons).[39] Consequently, two-photon luminescence (TPL) can be used to determine the exciton binding energy of monolayer WS_2. For instance, Ye et al. estimated the positions of dark excitonic states by using TPL. Two prominent dark excitonic peaks labeled as 2p and 3p states are observed, which are located at 2.28 and 2.48 eV, respectively. The ab initio GW method is employed to calculate the quasi-particle band structure, whereas the ab initio GW plus Bethe-Salpeter equation approach is utilized to evaluate the excitonic states and optical spectrum of monolayer WS_2. The calculated positions of 2p and 3p states of the X_A exciton as well as the 1s state of the X_A exciton and X_B exciton are in good agreement with the experimental spectrum. The quasi-particle band gap is found to be ≈2.7 eV from the calculation. Thus, the exciton binding energy of ≈0.7 eV is obtained. **Table 1** lists the quasi-particle band gap and exciton binding energy of monolayer WS_2 reported in literature, which confirms the relatively large quasi-particle band gap and exciton binding energy of monolayer WS_2.

2.5. Raman Spectrum

Raman spectrum is a powerful nondestructive technique to study 2D materials. For Raman spectrum of bulk WS_2 in a backscattering geometry, it contains first-order modes at the Brillouin zone center ($E^1_{2g}(\Gamma)$ and $A_{1g}(\Gamma)$) plus a zone-edge mode, which is activated by disorder, being identified as the longitudinal acoustic mode at the M point (LA(M)).[46] LA(M) mode are in-plane collective movements of the atoms in the lattice, similar to the sound waves. Additional Raman peaks are attributed to the multi-phonon combinations of these modes. Similar to the bulk WS_2, the Raman spectrum of monolayer WS_2 depends on the excitation wavelength (**Figure 5**a).[47] For excitation wavelength of 488 nm, the Raman spectrum is dominated by the first-order modes: LA(M) at 176 cm^{-1}, $E^1_{2g}(\Gamma)$ at 356 cm^{-1}, and $A_{1g}(\Gamma)$ at 418 cm^{-1}. However, under the excitation at 514.5 nm laser, the Raman spectrum becomes richer (Figure 5a). Many second-order peaks get stronger than those observed in the bulk WS_2. The strongest Raman peaks excited at 514.5 nm is the 2LA(M) mode at 352 cm^{-1}, which is almost twice of that of the $A_{1g}(\Gamma)$ mode. Moreover, $E^1_{2g}(\Gamma)$ peak at 356 cm^{-1} overlaps with 2LA(M) peak. Multi-peak Lorentzian fitting has then been used to separate the individual peaks. The rich Raman peaks excited with 514.5 nm are caused by enhanced second-order

Table 1. Quasi-particle band gap (E_g) and exciton binding energy (E_b) of monolayer WS_2.

Methods	E_g [eV]	E_b [eV]	Ref.
DFT	2.88	1.04	[253]
DFT + reflectance spectrum	2.41	0.32	[45]
DFT + TPL	2.7	0.7	[23]
TPL	2.73	0.71	[254]
Optical reflectivity/absorption spectra	3.01	0.83	[255]

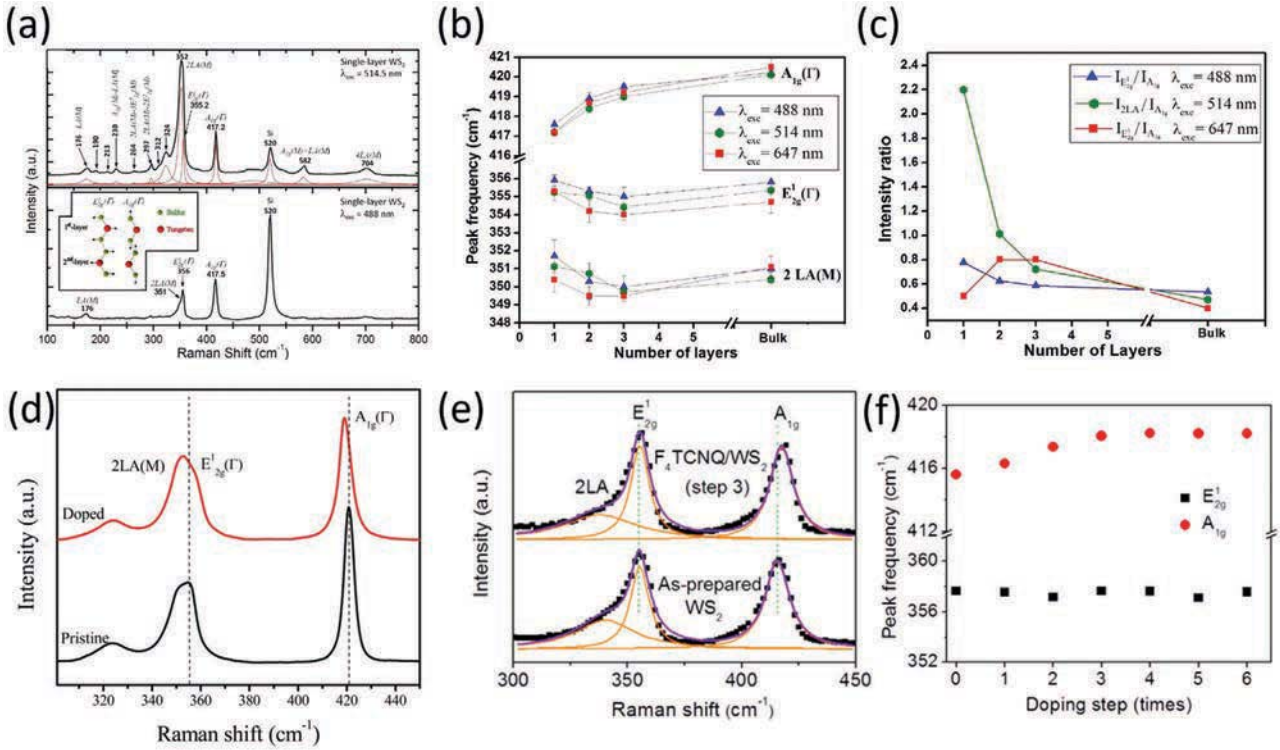

Figure 5. Raman spectra of WS_2. a) Raman spectra of monolayer WS_2 excited by light with 514.5 and 488 nm wavelengths. b) Peak frequencies as a function of number of layers. c) Relative Raman peak intensity under different light excitations. d) Raman spectrum of monolayer WS_2 with and without n-doping. e) Raman spectrum of monolayer WS_2 with and without p-doping. f) Raman peak frequencies as a function of doping step. a–c) Reproduced with permission.[47] Copyright 2013, Springer Nature. d) Reproduced with permission.[52] Copyright 2015, American Chemical Society. e,f) Reproduced with permission.[54] Copyright 2014, American Chemical Society.

Raman peaks arising from the double-resonance Raman process.[46,47] Rich Raman peaks are as well observed when excited with 532, 647 nm wavelengths.[47–49]

The positions and relative intensities of the Raman peaks are sensitive to the number of layers of WS_2.[32,47,50] As shown in Figure 5b, $A_{1g}(\Gamma)$ mode exhibits blueshifts with increasing the layer number of WS_2. The hardening of the $A_{1g}(\Gamma)$ mode is ascribed to the increased restoring force due to van der Waals interactions established among the layers. Nevertheless, the $E^1_{2g}(\Gamma)$ and 2LA(M) phonon modes display subtle redshifts with the increase of layer number of WS_2. It should be noticed that the error of the positions of 2LA(M) and $E^1_{2g}(\Gamma)$ modes increases because of the close proximity of the two modes. The frequency difference of $A_{1g}(\Gamma)$ and $E^1_{2g}(\Gamma)$ modes increases with the increasing layer number, which is usually used to determine the thickness of WS_2.[50] The relative intensity of the prominent Raman peaks depends on the number of layers as depicted in Figure 5c. The most interesting feature is that the intensity ratio of 2LA(M)/$A_{1g}(\Gamma)$ enhances dramatically for double- and single-layer WS_2 with 514.5 nm excitation line. The intensity ratio of 2LA(M)/$A_{1g}(\Gamma)$ is larger than 2 for single-layer WS_2, which provides a fingerprint to determine the monolayer WS_2.[47]

Besides, the characteristics of Raman spectrum of monolayer WS_2 is highly depended on the applied strain.[42] The E^1_{2g} mode is very sensitive to the strain, while the A_{1g} mode is inert to the in-plane strain. The E^1_{2g} mode evolves in-plane opposite displacements of W and S atoms, whereas the A_{1g} mode corresponds to the vibration of S atoms perpendicular to the plane.[51] This way, E^1_{2g} is sensitive to the in-plane strain but A_{1g} does not. With the increase of the stain, E^1_{2g} would have a redshift phenomenon and then split into two sub-modes: E^{1+}_{2g} and E^{1-}_{2g}. A_{1g} does not show any change under low strain; however, it gives a slight redshift at high strain, which is attributed to the laser-induced heating.[42]

Apart from strain, the A_{1g} mode of WS_2 is also sensitive to doping but the E^1_{2g} mode does not. The A_{1g} mode has a strong coupling with electron, which softens and broadens with the increase of electron doping (Figure 5d).[52,53] Upon p-type doping, the A_{1g} mode shows a blueshift whereas the E^1_{2g} mode remains unchanged (Figure 5e). The blueshift of the A_{1g} mode increases with the p-type doping level (Figure 5f). In particular, the saturation of the blueshift can be caused by saturated p-type doping by 2,3,5,6-tetrafluoro-7,7,8,8-tetracyanoquinodimethane molecules.[54] All these findings demonstrate the usefulness of Raman spectroscopy for the detailed characterization of WS_2.

2.6. Tunable Refractive Index by Electrical Field

The refractive index of WS_2 can be tuned by electrical field, which makes it useful for photonic applications. As shown

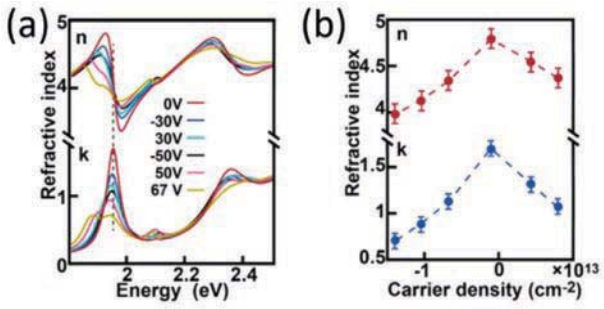

Figure 6. Tunable refractive index of monolayer WS_2. a) Refractive index under different gate voltage. b) Refractive index as a function of charge carrier density. Reproduced with permission.[55] Copyright 2017, American Chemical Society.

in **Figure 6**a, both the real (n) and imaginary (k) parts of the refractive index of monolayer WS_2 can be manipulated by gate voltage.[55] The refractive index near the X_A exciton shows the substantial tenability such that the n value can be varied from 4.8 to 3.97, while the k value can be changed from 1.7 to 0.7. The variation of the n value at 1.92 eV and the k value at 1.95 eV as a function of charge density are then presented in Figure 6b. Both the real and imaginary parts of the refractive index have their corresponding maximum values at the charge neutrality point and decrease with the increasing charge density. The tunability of the refractive index of monolayer WS_2 is attributed to the spectral broadening and the interconversion of the neutral and charged excitons caused by the injected charge carriers.[55] Moreover, the refractive index near the optical communication band (≈1.55 μm) can also be changed by electrical gating.[56] The Δn reaches 0.53 ± 0.06 RIU (refractive index units) for a maximum doping of (7.2 ± 0.8) × 10^{13} cm^{-2}, whereas the value of Δk is only 0.004 ± 0.002. This result indicates that monolayer WS_2 has a unique combination of strong electro-refractive response and small electro-absorptive response at near-infrared (NIR) wavelengths. In this case, the propagating light would undergo a large phase change with low loss, which is useful for optical modulators in optical communications.[56]

2.7. Strong Light–Matter Interaction

Theoretical calculation indicates that the density of states and the joint density of states of TMD materials show strong peaks in the visible range associated with Van Hove singularities in the density of states.[57] These Van Hove singularities in the density of states guarantee the enhanced light–matter interaction, resulting in the improved photon absorption and electron–hole pair creation. Both theoretical and experimental results reveal that a single layer of WS_2 can absorb more than 10% of the incident light, suggesting the strong light–matter interaction in a monolayer WS_2.[58,59] This strong light–matter interaction would lead to a very large absorption coefficient of ≈1.5 × 10^6 cm^{-1}.[58] All these findings demonstrate the promising potential of WS_2 for applications in various optoelectronic devices.

2.8. Mobility

Theoretically, monolayer WS_2 possesses superior electrical properties with a high carrier mobility for both electrons and holes. The interaction of these carriers with lattice vibration, known as phonons, actually dictates the intrinsic transport properties of WS_2.[60] When considering all phonon branches, the room temperature electron and hole mobilities of monolayer WS_2 are found to be 320 and 540 cm^2 V^{-1} s^{-1}, respectively. The effective electron and hole masses are determined to be $0.31m_0$ and $0.42m_0$ (m_0 is the mass of a free electron), accordingly.[60] The larger effective mass and mobility of hole designate that the hole transport experiences less scattering with phonons. In addition, WS_2 has the highest electron and hole mobilities among all MX_2 (M = Mo, W; X = S, Se) materials. When only long wave acoustic phonons are considered, monolayer WS_2 would have a room temperature electron mobility of 1103 cm^2 V^{-1} s^{-1}.[22] These calculated results suggest that WS_2 has huge potentials as channel materials for high-performance FETs.

3. Synthesis

Until now, various kinds of synthesis methods were developed for TMDs.[19,61,62] Because vapor phase synthesis is a versatile method to achieve large-area high-quality 2D materials, we only focus on the vapor phase synthesis techniques for 2D WS_2 in this review. For other methods, the readers can find some excellent reviews on TMDs.[63–65] In fact, there are diverse kinds of vapor phase synthesis methods that have been developed. They can be classified into three main classes according to the precursor sources employed, including the sulfurization of seed films, vapor source methods, and solid-state source method. The following discussion will be based on this classification after the introduction of basic growth mechanisms.

3.1. Basic Growth Mechanisms

The detailed growth mechanisms of 2D materials utilizing chemical vapor deposition (CVD), a major type of vapor phase synthesis techniques, are intensively studied in the past years.[66–68] Generally, the growth of a material there includes nucleation and crystal growth. The growth of 2D WS_2 also conforms this principle; however, there are still some differences for synthesizing 2D layered materials. Because of the passivated in-plane surface, the surface adatoms can easily migrate, while the adatoms have large possibility to incorporate into the 2D lattice at the edges. As a result, lateral growth is usually preferred. However, it is difficult for 2D layered materials directly nucleating on a smooth surface due to the weak interaction of the passivated in-plane surface with the substrate. Thus, two general growth mechanisms are proposed for the growth of 2D layered materials. The first one is the direct nucleation at a substrate in imperfect sites with the subsequent lateral growth (growth model 1 in **Figure 7**).[69,70] The second one is the formation of nanoparticles, e.g., WO_3 nanoparticles, accompanied by the formation of a layered material shell, followed by the lateral

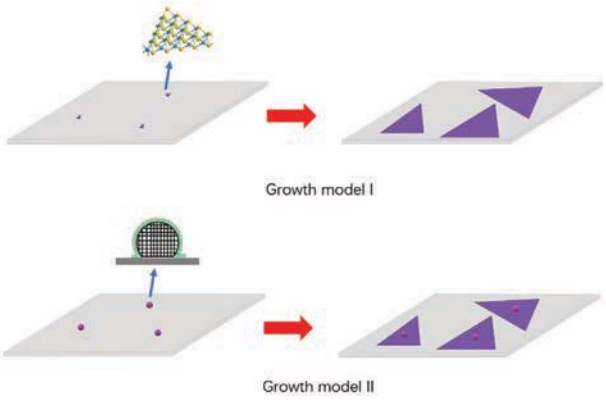

Figure 7. General growth model for 2D WS_2.

growth of 2D material (growth model II in Figure 7).[67] These difference growth models usually result in the different morphology of the grown films, particularly that nucleation nanoparticles are observed for the growth model II.[67] Furthermore, multilayer growth may get initiated if the metal precursor concentration is too high, leading to the multilayer domain near the center of single-domain flakes.[71] Typically, the presence of nanoparticle or multilayer domain can be reduced with the introduction of H_2 gas due to the etching effect.[72,73] It should also be noted that the growth mechanisms introduced here are invalid for sulfurization of seed film methods, which depends on the seed film formation.

3.2. Sulfurization of Seed Films

The sulfurization of seed films is a convenient method to obtain wafer-scale atomically thin 2D WS_2 films, with the quality of which depends highly on the quality of the seed film and sulfurization process. At present, various methods were used for the preparation of the seed films. These methods can be divided primarily into two types as: vacuum deposition and spin-coating. Among the vacuum deposition methods, they can be further divided into thermal/electron-beam evaporation, magnetron sputtering, and atomic layer deposition (ALD). The following discussion is arranged based on the seed film preparation methods, from vacuum deposition to spin-coating methods.

3.2.1. Thermal/Electron-Beam Evaporation

Thermal evaporation method is a simple technique for the deposition of metal oxide films with controlled thickness, which can be used to deposit WO_x as the seed films for the preparation of WS_2 films.[74–78] For example, Elías et al. synthesized 2D WS_2 by the sulfurization of thermally evaporated WO_x films.[74] The basic setup for the sulfurization process is shown in **Figure 8**a. With appropriate sulfurization procedures, large-area 2D WS_2 films can be easily obtained (Figure 8b). The thickness of WS_2 films is mainly determined by the thickness of starting WO_x seed films. Monolayer, bilayer, and trilayer WS_2 film can then be obtained through the sulfurization of a 1, 2, and 2.8 nm thick WO_x films, respectively. The quality of grown WS_2 films is also closely related with the WO_x seed films. Although this method is highly scalable, the quality of obtained WS_2 films is relatively poor with small domain size and many defects. Furthermore, the uniformity of resulting WS_2 films is not good as well. At the same time, electron-beam evaporation is often used for the deposition of metal films. It has the ability to evaporate high melting point metals, such as W, due to the high energy of electron beam utilized in the process. In this regard, Mutlu et al. tried to synthesize WS_2 film by sulfurization of W metal films deposited by electron-beam evaporation.[79] However, due to the island-like morphology of the W metal seed layer, the resulting WS_2 film is discontinuous with nonuniform thickness. Further optimization is needed.

3.2.2. Magnetron Sputtering

Magnetron sputtering is widely used in the deposition of various kinds of films, such as metal films and metal oxide films. This way, it has also been commonly used for the preparation of seed layers for the synthesis of 2D WS_2 films.[80–84] Hussain et al. realized the wafer-scale WS_2 film preparation through the sulfurization of a radio frequency-magnetron sputtered WO_3 film.[81] By tuning the sputtering time to change the film thickness of WO_3, the thickness of WS_2 films could be well controlled from 1.8 to 5 nm. Nevertheless, the obtained WS_2 had a nanocrystalline structure and composed of different layers. Magnetron sputtered W metal films were as well exploited as seed layers for the preparation of WS_2 films as demonstrated by Orofeo et al.[80] The grown film is polycrystalline with domain sizes ranging from 20 to 200 nm as shown in Figure 8c. Later, Jung et al. found that the orientation of obtained WS_2 films was strongly related to the sputtered W metal film thickness as given in Figure 8d.[82] The layer orientation of WS_2 is vertical to the substrate for thick W seed films (15 nm), while it is parallel to the substrate for very thin W seed films (2 nm), and the mixed orientation of WS_2 film is found for intermediate thick W seed films (5 nm). These orientation changes of WS_2 films upon the thickness of W metal films can be understood via the competition between surface energy and strain energy. In specific, there is a significant volume expansion for the conversion of W seed to WS_2 film due to the insertion of S atoms. When the seed layer is very thin and discontinuous, the growth of 2D horizontal film is energetically favorable. The reason is that the basal planes with low surface energy are exposed for the horizontal grown film, while the high surface energy edge sites are exposed for the vertical grown film. Notably, the surface energy of the edge sites is almost two orders of magnitude higher than that of the basal plane.[85] Furthermore, the horizontal volume expansion can be accommodated because the seed layer is discontinuous (Figure 8e). For thick continuous W films, the horizontal volume expansion cannot be accommodated upon sulfurization due to the anchor of the film by the substrate. Thus, significant amount of strain is induced in the film, which is not energetically favorable. For films with the vertically aligned orientation, the volume expansion can be accomplished in the vertical direction freely without any strain even though

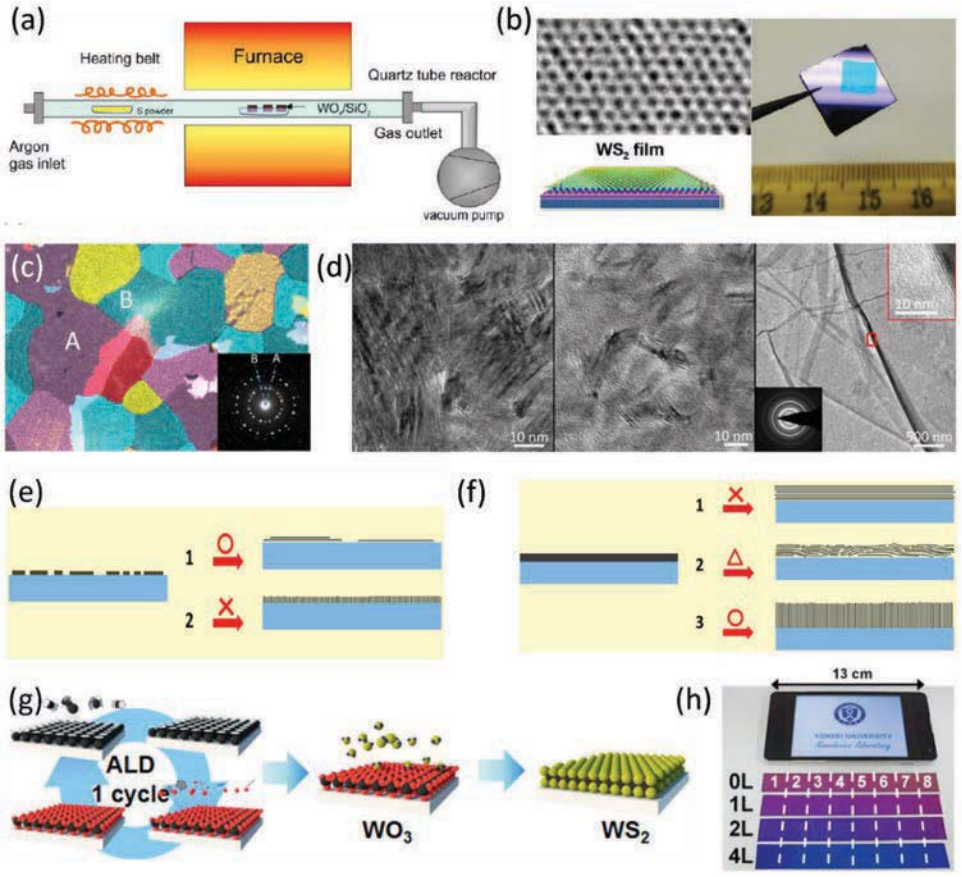

Figure 8. Sulfurization of seed films. a) Schematic of the setup for sulfurization of WOx films. b) Transmission electron microscopy (TEM), schematic, and photograph of the resulting WS_2 films. c) Dark TEM image with faked color showing different domains. Inset shows the selected area electron diffraction from the labeled areas. d) TEM images of the WS_2 grown with different W metal seed film thicknesses. The seed thicknesses of the W metal film from left to right are 15, 5, and 2 nm. e,f) Schematics to show the vertical-to-horizontal growth transition initiated with the thin metal seed and thick metal seed layers, respectively. g) Schematic for the sulfurization of ALD-deposited WO_3 films. h) Photograph of the WS_2 films with different thicknesses. a,b) Reproduced with permission.[74] Copyright 2013, American Chemical Society. c) Reproduced with permission.[80] Copyright 2014, AIP Publishing. d–f) Reproduced with permission.[82] Copyright 2014, American Chemical Society. g) Reproduced with permission.[86] Copyright 2013, American Chemical Society.

the surface energy is increased due to the exposure of the edge sites. For W films with intermediate thickness, both vertical and horizontal growth can occur in order to minimize the total energy of the material system (Figure 8f).

3.2.3. ALD

As compared with thermal/electron-beam evaporation and magnetron sputtering, ALD gives more precise control on the WO_3 seed film thickness due to its self-limited growth mechanism. As a result, the thickness and uniformity of resulting WS_2 films can be well controlled.[86,87] Song et al. used ALD to deposit WO_3 films and subsequently sulfurization was performed to convert it into WS_2 films (Figure 8g).[86] Utilizing this method, they could get large-area uniform WS_2 films with thickness from monolayer to four layers (Figure 8h). Due to the high quality of seed layers the resulting WS_2 films also exhibit good quality although it still had small crystal domains. The fabricated top-gated FETs based on these monolayer WS_2 showed an electron mobility of 3.2 $cm^2\ V^{-1}\ s^{-1}$, which is already much higher than the value previously reported for the CVD grown WS_2 transistor (≈0.01 $cm^2\ V^{-1}\ s^{-1}$),[88] indicating the decent material quality of WS_2 here.

3.2.4. Spin Coating

Spin-coating method is widely used for the deposition of thin films. For the preparation of seed layers, dissoluble W-containing salts are employed. Currently, there are various kinds of W-containing materials suitable for the preparation of precursor solutions, such as $(NH_4)_2WS_4$,[89,90] H_2WO_4,[91] Na_2WO_4,[92–95] and $(NH_4)_6H_2W_{12}O_{40}$.[96] Due to the differences of wettability of the substrate with different precursors, the seed layer preparation procedure is somewhat different among various process schemes. Kwon et al. found that ethylene glycol is a good coordinated solvent for $(NH_4)_2WS_4$ to obtain uniform precursor seed

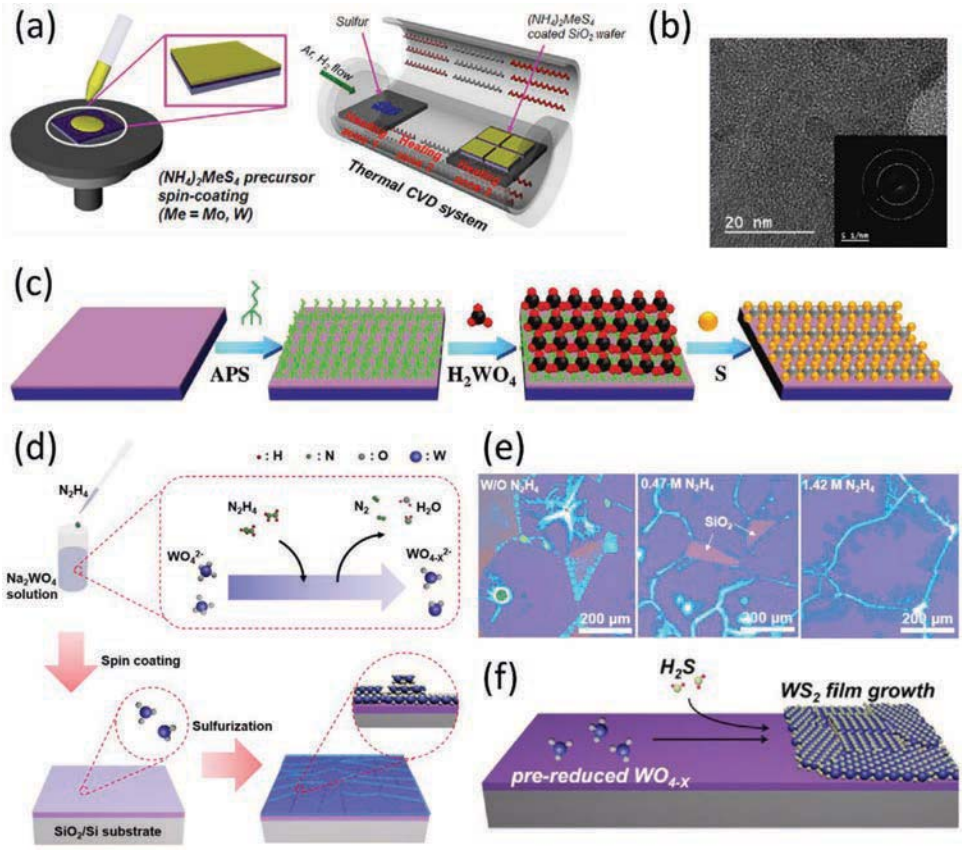

Figure 9. Solution processed seed films. a) Schematic for the preparation of WS_2 films with $(NH_4)_2WS_4$ precursor solution. b) TEM image and selected area electron diffraction of the resulting WS_2 films. c) Schematic for the synthesis of WS_2 films with APS processed substrate. d) Schematic for the conversion of tungsten suboxide films into continuous WS_2 films. e) Morphology evolution of the WS_2 film with different amount of N_2H_4. f) Schematic illustration for the growth of WS_2 films with pre-reduced tungsten suboxide films. a,b) Reproduced with permission.[89] Copyright 2015, American Chemical Society. c) Reproduced with permission.[91] Copyright 2017, John Wiley and Sons. d–f) Reproduced with permission.[92] Copyright 2017, American Chemical Society.

films.[89] The SiO_2/Si substrate is first cleaned with a piranha solution, acetone, isopropyl alcohol, and deionized water for 10 min in a regular sequence. After that, the substrate is treated with O_2 plasma and UV-O_3 for 15 min. The precursor solution is then spin coated onto the substrate. After the formation of a uniform seed layer, two-step thermolysis process is performed (**Figure 9**a). The thermolysis at 500 °C under N_2 atmosphere can convert the spin-coated $(NH_4)_2WS_4$ seed films into WS_x thin layers. The complete conversion of WS_x into WS_2 would occur at 950 °C with sulfur gas and H_2. Through this method, large-area WS_2 film can be obtained. The obtained film has polycrystalline structure with nonuniform thickness distribution as shown in Figure 9b. Abbas et al. further optimized the three parameters and created uniform large-area atomically thin WS_2 layers by a two-step thermal decomposition of $(NH_4)_2WS_4$ spun-coated films. In any case, the electron mobility of obtained WS_2 film is still very low of 10^{-4} to 10^{-2} cm^2 V^{-1} s^{-1}.[90] Using the H_2WO_4 precursor, Chen et al. found that the functionalization of the substrate is very important for obtaining uniform WO_3 films by spin-coating method, which significantly affect the quality of resulting WS_2 films.[91] The synthesis procedure is depicted in Figure 9c. The silanization of SiO_2/Si substrates is realized by decorating a layer of 3-aminopropyltriethoxysilane (APS) on the substrates. APS functional groups can act as a buffer layer for the H_2WO_4 precursor, resulting in the formation of uniform WO_3 seed films. As a result, uniform monolayer WS_2 films can be synthesized by the sulfurization of these uniform WO_3 seed films. Furthermore, the obtained monolayer WS_2 film has large single crystalline domains, approximately tens or even hundreds of micrometers in diameter, indicating the high quality of the obtained film. It is worth to mention that the oxidation state of W ions in solution-processed films is very important for realizing continuous WS_2 films as demonstrated by Choi et al.[92] N_2H_4 is required to be added into the $NaWO_4$ solution to manipulate the oxidation state of W ions as schematically shown in Figure 9d. With the increase of the amount of N_2H_4, the film morphology would change from discontinuous to continuous manner as illustrated in Figure 9e. It is proposed that the pre-reduced tungsten suboxides by N_2H_4 can directly participate in the growth of WS_2, ensuring to achieve a full coverage of WS_2 film on the substrate (Figure 9f). In contrast, using H_2 as reducing reagent during the conversion of Na_2WO_4 films cannot result in continuous films because of the etching effect of H_2 to WS_2. The domain size of WS_2 films obtained by the use of tungsten suboxide seed film is about 200 μm. But the film is not uniform, with multilayer WS_2 flakes grown at the

boundaries of the underlying single-layer WS_2 film (Figure 9e). The substrate used for the preparation of seed layers is as well important for the quality of WS_2 films. Lee et al. showed that single-crystal WS_2 can be epitaxially grown on BN films by spin coating $NaWO_4$ on the single-crystal BN film with subsequent sulfurization.[97]

3.2.5. Doping

Sulfurization of seed films is a powerful way to substitute doping in WS_2 because it only needs the addition of dopants in the seed film. For example, Cao et al. realized p-type doping by the sulfurization of WO_xN_y film deposited by ALD method (**Figure 10**a).[98] Accordingly, they could obtain 2 inches (") wafer-scale N-doped WS_2 film due to the scalability of ALD method (Figure 10b). The N-doped few-layer WS_2 film delivered an average hole mobility of 5.5 $cm^2\ V^{-1}\ s^{-1}$, when using Pt as device electrodes. Actually, solution precursors can be mixed well at the atomic level, leading to the homogenous and controllable doping in resulting WS_2 films. In this way, solution-prepared seed films can be used in the synthesis of doped WS_2 films with precisely controlled doping level.[95,96] Zhang et al. adopted this method for the synthesis of Fe-doped WS_2 flakes and other doped TMDs (Figure 10c).[96] The Fe dopant atoms showed a uniform distribution in the WS_2 host lattice, while the doping level could be well controlled (Figure 10d). Unfortunately, continuous films have not been realized using this method, where further optimization is needed.

3.3. Vapor Source Method

Vapor source methods do not imply that all precursor sources are existed in the vapor phase for the synthesis of WS_2 films. In fact, these methods utilize solid and liquid sources, but they are not placed in the chamber directly. They are first converted into gas phase and then introduced into the reaction chamber. Depending on the source materials used here, the vapor source methods can be classified into metal–organic CVD (MOCVD) and conventional vapor source CVD. For example, MOCVD consumes metal–organic materials as the precursor sources, which can be easily evaporated at low temperatures but most of them are toxic. In addition, vapor source methods can also be categorized into ALD and CVD based on their different growth mechanisms. In this case, this section would be divided into three sub-sections, focusing on MOCVD, ALD, and conventional vapor source CVD for the growth of WS_2 films.

3.3.1. MOCVD

Actually, MOCVD is widely considered as a scalable fabrication method for the wafer-scale synthesis of numerous thin films. Kang et al. adopted this method for the synthesis of atomically thin 2D materials for the first time.[99] With optimized conditions, monolayer WS_2 films up to 4" in size can be obtained. During the growth, precursor sources of $W(CO)_6$, $(C_2H_5)_2S$ (also known as DES) and H_2 are employed, where they are all diluted in the carrier gas of Ar. The concentration

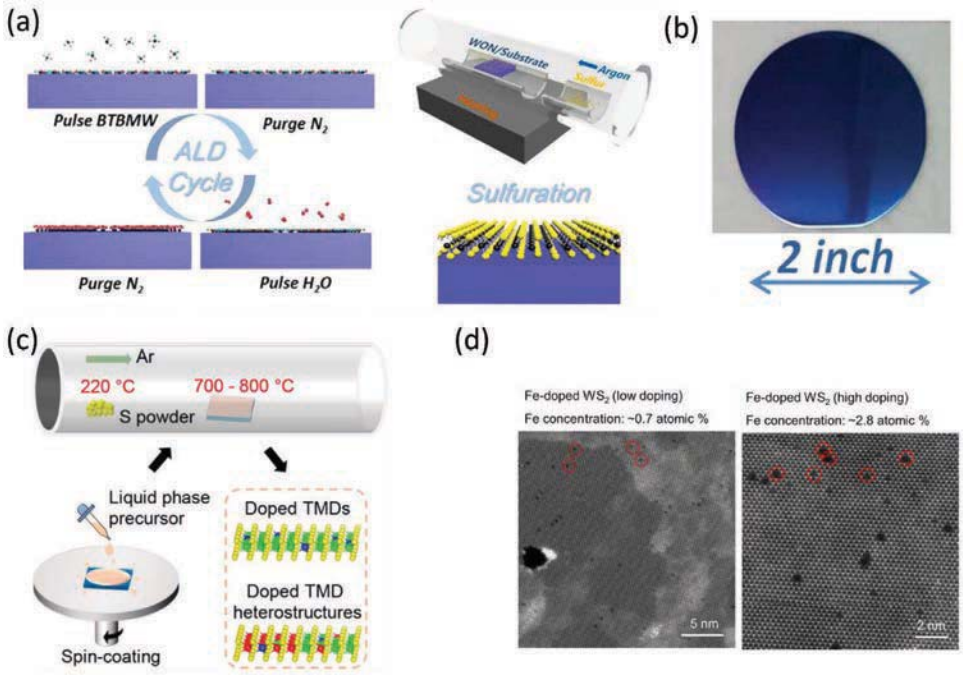

Figure 10. Doping in the seed film. a) Schematic for the synthesis of N-doped WS_2 using ALD-synthesized WOxNy as the seed film. b) Photograph of the 2" large N-doped WS_2 film. c) Schematic for the synthesis of doped WS_2 by using solution-processed seed films. d) Scanning transmission electron microscope images of the Fe-doped WS_2 with different doping concentrations. a,b) Reproduced with permission.[98] Copyright 2017, American Chemical Society. c,d) Reproduced with permission.[96] Copyright 2020, American Chemical Society.

of each reactant can be precisely controlled by regulating the partial pressure of each reactant. As a result, the nucleation density and intergrain stitching are well controlled. With a low partial pressure of the W precursor, the WS_2 film tends to grow in a layer-by-layer mode. In specific, seed nucleation is first occurred on the substrate, followed by the subsequent growth around the seed edges for the formation of monolayer film. After that, seed nucleation is concentrated to take place at the grain boundaries for the consequent bilayer growth. This way, the edge attachment is the main driving mechanism for the monolayer growth after nucleation, leading to the lateral extension of the monolayer grains. Hence, the adjacent monolayer grains are always connected by the tilt grain boundaries. This layer-by-layer growth mode would be easily destroyed when the high W precursor partial pressure is utilized, resulting in a mixture of monolayer, multilayer, and no-growth regions. It is therefore important to maintain a low W precursor partial pressure during the entire growth process in order to obtain a uniform monolayer WS_2 film. Moreover, the grain structures of WS_2 films, such as the grain size and intergrain connection, are found highly depended on the precursor concentration of H_2 and DES, as well as the amount of residual H_2O in the reaction chamber. H_2 is observed to have two functions for the synthesis here. In particular, H_2 can easily induce decomposition of DES, which in turn increases the seed nucleation due to hydrogenolysis. Also, H_2 can perform etching of the WS_2 film, preventing the intergrain connection. On the other hand, the increase of DES and residual H_2O concentration enhances the seed nucleation density with the decreased grain size. In this regard, it is necessary to have the optimal concentration of precursors to achieve continuous monolayer WS_2 with large grains and high-quality intergrain stitching. Once the synthesis is relatively optimized, the as-grown WS_2 film can exhibit an average electron mobility of 5 $cm^2\ V^{-1}\ s^{-1}$, when they are fabricated into transistors. At present, although MOCVD can produce the wafer-scale monolayer films, it still has a very low growth rate, requiring 26 h for the full coverage of a 4 in. wafer. Furthermore, the grain size is small (about 1 μm) with random orientation. Due to the similar lattice symmetry of sapphire with WS_2, Grundmann et al. found that epitaxy coalesced WS_2 layers could be obtained by tuning the growth parameters.[100] In any case, the conventional hot-wall chamber for MOCVD is highly energy consumption. The possible decomposition of precursors before reaching the substrate would make the growth process extremely complicated. In order to solve these problems, Choudhury et al. employed a cold-wall CVD chamber for the synthesis of WS_2 films as shown in **Figure 11**a.[101] In contrast to the hot-wall MOCVD, DES is not suitable to be used as the S source in a cold-wall MOCVD system because it would lead the formation of graphitic carbon, which can compete with the growth of WS_2, inhibiting the lateral extension of WS_2. Accordingly, the grain size of WS_2 is only about 50 nm (Figure 11b). More importantly, the contamination of WS_2 films by carbon species would lead to the quenching of the measured PL spectrum (Figure 11d). H_2S is found to be a good S precursor in the cold-wall MOCVD system. Using H_2S, the fabricated WS_2 films have a relatively large grain size (≈200 nm, Figure 11c) without any contamination associated

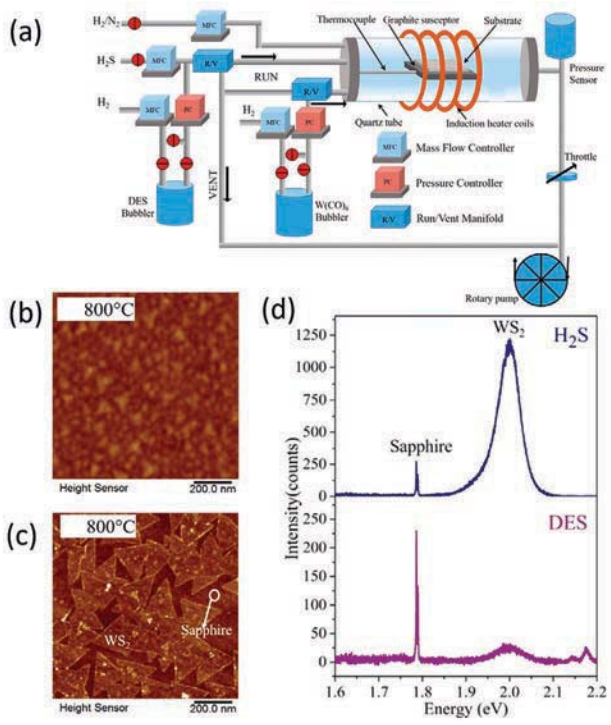

Figure 11. MOCVD synthesis of WS_2. a) Schematic of the cold-wall MOCVD system. b,c) AFM image of the WS_2 film grown with the precursors of DES and H_2S, respectively. d) PL spectra of the WS_2 films grown with the precursors of H_2S and DES. Reproduced with permission.[101] Copyright 2018, American Chemical Society.

with carbon species. The obtained WS_2 also exhibits a strong PL emission (Figure 11d). Even though the required growth time for a continuous WS_2 film is much reduced down to only ≈30 min as compared with that of the hot-wall MOCVD system, the film uniformity is still poor.

3.3.2. ALD

ALD has as well been adopted to synthesize atomically thin WS_2 films. There is a distinctive difference between ALD and CVD that ALD process relies on the alternative supply of precursors one at a time onto the substrate, which leads to a layer-by-layer growth mode of thin films.[102] This unique ALD growth mechanism would ensure excellent growth control of conformal WS_2 films at the atomic level and at low temperatures on large-area substrates, even with features of 3D structures consisting of high aspect ratio.[103] Furthermore, the process temperature of most of the ALD synthesis is compatible with back-end-of-line (BEOL) techniques (≤ 450 °C), making ALD attractive for many advanced applications.[104] Usually, WF_6 and H_2S are used as the W and S sources, respectively, for the ALD synthesis of WS_2 films.[103–106] Because W in WF_6 has an oxidation state of +6, it needs to be reduced to +4 for the formation of WS_2. H_2 plasma is hence employed as a good reducing agent to synthesize WS_2.[103–106] In principle, the synthesis of WS_2 films by ALD is based on a ternary reaction cycle as given in

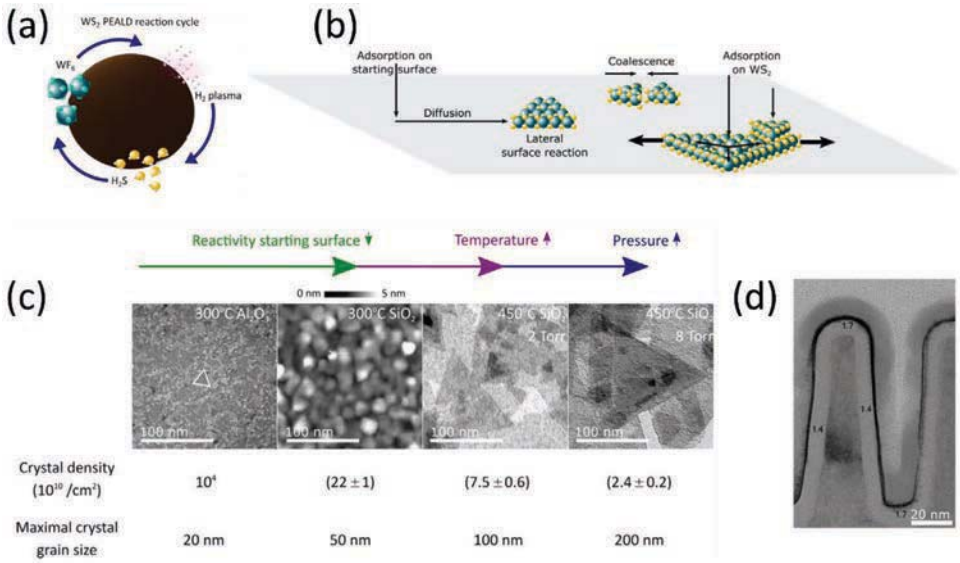

Figure 12. ALD synthesis of WS_2 films. a) Schematic of the ternary ALD reaction cycle required for the formation of WS_2. b) Schematic of the nucleation mechanism for the growth of WS_2. c) Evolution of the crystal density and grain size of WS_2. d) TEM image of WS_2 deposited on Si fins by ALD. Reproduced with permission.[104] Copyright 2018, American Chemical Society.

Figure 12a: WF_6 reaction, H_2 plasma exposure, and H_2S reaction.[104,105] Detailed investigation reveals that there are actually four mechanistic processes for the nucleation of WS_2 films by ALD (Figure 12b).[104] They are: 1) precursor adsorption on both the starting surface and WS_2 crystals; 2) adatom diffusion and surface reactions; 3) incorporation into existing WS_2 crystals; and 4) crystal ripening by migration of either adatoms or crystals, followed by coalescence. Notably, the use of H_2 plasma is essential, which is important for the formation of metallic W species or lower oxidation state of W. No WS_2 can be synthesized without the use of H_2 plasma.[104,105] In addition, the growth mode is different on different substrates due to their different surface reactivity. For example, the growth mode of WS_2 films on Al_2O_3 is layer by layer, while it shows an island-like growth mode on SiO_2.[104] The grain size of obtained WS_2 films is also sensitive to the substrate type, pressure, temperature, etc., employed for the ALD synthesis (Figure 12c). With the optimal synthesis parameters, the grain size of WS_2 can be as large as 200 nm.[104] Apart from providing the required W precursor species, the H_2 plasma-assisted ALD is also advantageous to achieve the conformal deposition of WS_2 on 3D structures. To be specific, WS_2 films can be conformally deposited onto narrow fins as shown in Figure 12d. The (0002) basal planes of WS_2 can grow along the curvature of the SiO_2 fins at both the bottom and top of the trench. The conformal deposition of WS_2 with basal planes parallel to the fin surface would make it ideal for the utilization in fin-FETs. Except using H_2 plasma as a reducing agent, Heyne et al. developed an amorphous Si sacrifice layer as a reducing agent in the ALD system.[107] Although ALD is powerful in the synthesis of atomically thin 2D WS_2 films, the fabricated films are polycrystalline and nonuniform in thickness with small grain size, significantly deteriorating their electronic and optoelectronic properties.

3.3.3. Conventional Gas Phase CVD

For conventional gas phase CVD, the precursors are introduced into the reaction chamber in the gas form with continuous feeding. For the synthesis of 2D WS_2 films, Park et al. exploited WCl_6 and H_2S as the W and S sources, respectively.[108] WCl_6 gas is generated in a bubbler-containing WCl_6 and then transferred into reaction chamber by Ar carrier gas. The reaction is performed at 700 °C. Because of the high reaction temperature, no reducing agent is needed. The growth of WS_2 is found to obey the layer-by-layer growth mode as presented in the morphological evolution with increasing growth duration (**Figure 13**a–d). In explicit, the nucleation of WS_2 is first occurred, followed by the growth of the first layer. Subsequently, the second layer growth begins after the first layer is almost completely achieved. In this manner, the WS_2 film with different number of layers can be obtained by varying the deposition time (Figure 13e–g). Since gas phase precursors are employed here, this method can be used for large-area synthesis as shown in Figure 13h. However, the grain size is still relatively small of only ≈100 nm. It was reported that alkali metal halides had the ability to suppress the nucleation and hence enlarge the domain size of 2D TMDs.[109] Remarkably, Okada et al. introduced NaCl during the CVD synthesis of WS_2 using gaseous precursors of WF_6 and H_2S.[110] The size of obtained triangle-shaped WS_2 crystals was about 10 μm after the introduction of NaCl. Although large WS_2 crystals were obtained, no continuous film was realized. Irisawa et al. synthesized WS_2 films by gas phase CVD using WF_6 and H_2S as the sources in both hot-wall and cold-wall reaction chamber.[111] Wafer-scale WS_2 films in the size of 2" could be synthesized in both cases. Furthermore, the process temperature in the cold-wall system can be set as low as 250 °C, which widens the applications of 2D WS_2, such as the utilization in flexible electronics and BEOL transistors. Very recently, Tang

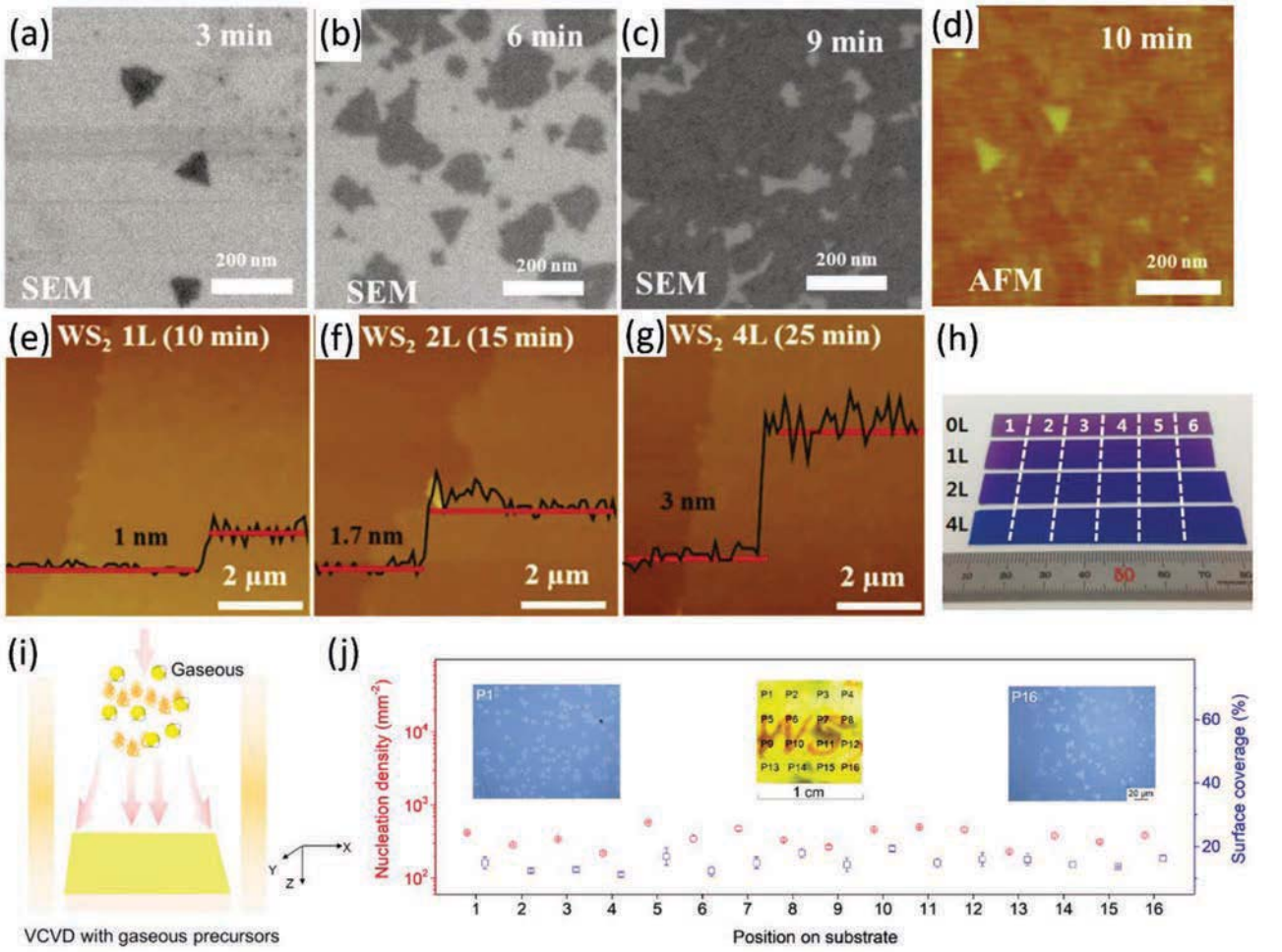

Figure 13. Conventional gas phase CVD synthesis of WS_2. a–d) Morphological evolution of the WS_2 film with growth time. e–g) Film thickness evolution with growth time. h) Photograph of the WS_2 films with different thicknesses. i) Schematic of the vertical furnace setup. j) Nucleation density and surface coverage of WS_2 as a function of position. a–h) Reproduced with permission.[108] Copyright 2015, Royal Society of Chemistry. i,j) Reproduced with permission.[112] Copyright 2020, American Chemical Society.

et al. designed a vertical furnace for the synthesis of single-layer WS_2 flakes as schematically depicted in Figure 13i.[112] Utilizing this setup, homogenous WS_2 single-layer flakes can be obtained (Figure 13j). As compared with the conventional horizontal furnace, the vertical configuration with gas flow from top to bottom can redistribute the temperature and gas field more effectively to eliminate any position dependence in the growth chamber, resulting in the more uniform deposition of WS_2 films.

3.4. CVD using Solid-State Sources

In this method, solid-state materials, such as powders and pallets, are used as the source materials or in combination with other gas phase or liquid phase precursors. Due to the diverse solid-state sources, especially for W, there would be a wide range of precursor materials and process parameters, possibly tuned to create large-area single-crystal 2D WS_2 film; therefore, this method has been one of the most intensively studied techniques. As anticipated, there are many parameters that can affect the growth of WS_2 here. In order to have a good understanding of this method, the following discussion will be arranged into several sub-sections: setup configurations, nucleation seed promoters, growth substrate, function of sulfur, function of hydrogen, and doping.

3.4.1. Setup Configurations

The basic experimental configurations for the CVD synthesis of WS_2 using solid-state sources can be classified into four types as shown in **Figure 14**a. Among all, both low pressure CVD (LPCVD) and ambient pressure CVD (APCVD) are commonly employed for these WS_2 growth. Type-I and type-II schemes are widely explored in literature owing to their setup simplicity. Type-I configuration is beneficial for the wafer-scale synthesis of 2D materials, as the substrate size is only limited by the diameter of the tube furnace. In fact, wafer-scale uniform monolayer WS_2 films (Figure 14b) have been realized by Lan

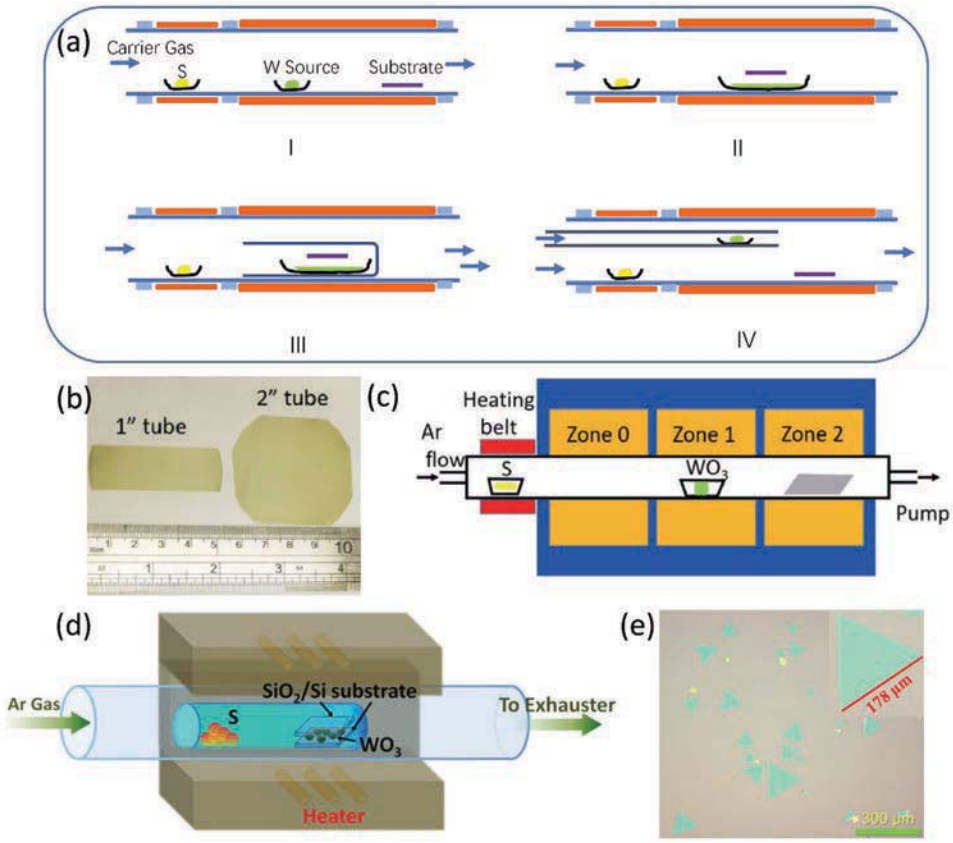

Figure 14. Setup configurations. a) Schematic illustration of four different experimental setup configurations for the CVD synthesis of WS_2 using solid-state sources. b) Photograph of the obtained wafer-scale monolayer WS_2 film. c) Schematic of the multi-zone furnace for the synthesis of WS_2. d) Schematic of the setup for the synthesis of large-area single-crystal WS_2. e) Optical microscope image of the obtained single-crystal WS_2 flakes. b,c) Reproduced with permission.[49] Copyright 2018, Springer Nature. d,e) Reproduced with permission.[48] Copyright 2014, John Wiley and Sons.

et al. utilizing the type-I scheme.[49] A schematic of their experimental setup is shown in Figure 14c. In order to independently tune the evaporation temperatures of S and WO_3 sources as well as the deposition temperature, the multi-zone tube furnace was used. LPCVD and high evaporation temperature (above 900 °C) are then employed to maintain a high partial pressure of WO_x for the growth of WS_2. For type-II configuration, it is not suitable for the scalable synthesis because the substrate size is restricted by the crucible placed below the substrate. The advantage of this configuration is that the W source is very close to the substrate such that the high partial pressure of W-containing precursor can be achieved even using APCVD and relatively low evaporation temperature (≈800 °C).[88,113] For type-III configuration, since the melting point of the precursor of WO_3 is very high, the WO_3 powder has to be placed in the sealed-end of the quartz tube to sustain a higher partial pressure of WO_x vapor during the growth.[48,114] Furthermore, when the WO_3 powder is put right next to the growth substrate (Figure 14d), very large single-crystal monolayer WS_2 films can be obtained as demonstrated by Cong et al. (Figure 14e).[48] The disadvantage of type-I to type-III configurations is that the W precursors easily get sulfurized into WS_2 during the growth, also known as precursor poisoning, which would subsequently block the continuous feeding of W-containing vapor to the substrate. As a result, type-IV scheme is proposed, where the W precursor and S precursor are independently introduced into the chamber without any mixing before reaching the substrate.[115–118]

3.4.2. Nucleation Seed Promoters

The direct nucleation of 2D WS_2 on smooth substrate is difficult because of the weak van der Waals interaction between the 2D WS_2 and the substrate. In order to promote the nucleation of WS_2 on the growth substrate, various kinds of seed materials are adopted, such as aromatic materials, WO_3, and Au nanoparticles. Perylene-3,4,9,10-tetracarboxylic acid tetrapotassium salt (PTAS) is a kind of aromatic materials that is widely used as a seed promoter for the growth of TMDs.[71,88,119–121] PTAS can offer a heterogenous nucleation site for the formation of TMD nuclei and hence increases the surface adhesive force of TMD molecules, which lead to the nucleation and lateral growth of TMDs.[120] Lee et al. illustrated the successful synthesis of high-quality monolayer WS_2 flakes by using the PTAS seed promoter as given in **Figure 15**a.[88] Moreover, WO_3 nanoparticles are also

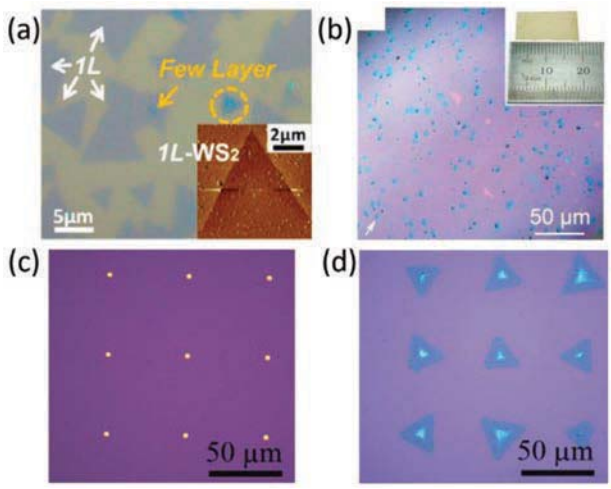

Figure 15. Nucleation seed promoters. a) Single-layer WS_2 prepared with the PTAS seed promoter. b) Monolayer WS_2 prepared with the WO_3 nanoparticle seed promoter. c) Au nanoparticle arrays and d) WS_2 flake arrays with the Au particle arrayed seed promoter. a) Reproduced with permission.[88] Copyright 2013, American Chemical Society. b) Reproduced with permission.[122] Copyright 2015, Royal Society of Chemistry. c,d) Reproduced with permission.[124] Copyright 2019, Royal Society of Chemistry.

an effective seed promoter as demonstrated by Lan et al.[122] By dip-coating a layer of WO_3 nanoparticles, large-area monolayer WS_2 film could be synthesized as displayed in Figure 15b. Likewise, carbon nanoparticles would not only act as a seed promoter but also serve as a reducing agent. In this case, the local WO_x concentration got enhanced, leading to the formation of bilayer nuclei and consequent growth of bilayer WS_2 as revealed by Liang et al.[123] At the same time, Au nanoparticles could as well be used as seed promoters.[124] Importantly, Au nanoparticle arrays could be easily realized through photolithography. These Au arrays were utilized as seed promoters for the growth of high-quality WS_2 patterns as witnessed in Figure 15c,d.

3.4.3. Growth Substrates

The substrate used for the growth can strongly affect the quality of obtained 2D WS_2 films. Till now, various kinds of substrates have been employed for the synthesis of WS_2, such as SiO_2/Si, sapphire, BN, graphene, and Au foils. The most widely used substrate is SiO_2/Si; however, WS_2 flakes grown on SiO_2/Si have random orientations.[48,88] On the other hand, sapphire, BN, and graphene have the hexagonal symmetry, similar to WS_2, which can enable the epitaxial growth of WS_2 on these substrates. Unfortunately, it is found difficult to realize the epitaxial growth of WS_2 on sapphire[122,125,126] because there is a weak interaction between WS_2 and sapphire as compared with the successful case of growing MoS_2 on sapphire.[127] As depicted in **Figure 16**a–c, high-quality epitaxial WS_2 flakes have been achieved on graphite,[128] graphene,[129–132] and BN substrates.[133] When using Au foils as growth substrates, very large single-layer WS_2 flakes can be obtained (Figure 16d).[70,134] The reason for the growth of large single-crystal monolayer WS_2 flakes is that Au can lower the barrier energies for sulfurization of WO_3 through the formation of sulfur atoms.[70] As a result, a very low concentration of WO_3 and S can lead to the formation of WS_2. Furthermore, the solubility of W in Au is very low that constrains the segregation and precipitation of W at the surface of Au foils, leading to the formation of single-layer WS_2. After the Au foil surface is fully covered by WS_2, no additional layers can be formed on WS_2 surface owing to the loss of catalytic activity of Au by the passivation of WS_2. This way, the growth of monolayer WS_2 on Au foil is a self-limiting process. In addition, the use of Au foil substrates would allow the roll-to-roll transfer of fabricated single-layer WS_2 onto flexible substrates as shown in Figure 16e,[70] which is beneficial for applications in flexible electronics and optoelectronics.

3.4.4. Halide Salts

The initial study of adding salts to the powder precursor for the synthesis of TMDs is carried out by Li et al.[135] Later, Zhou

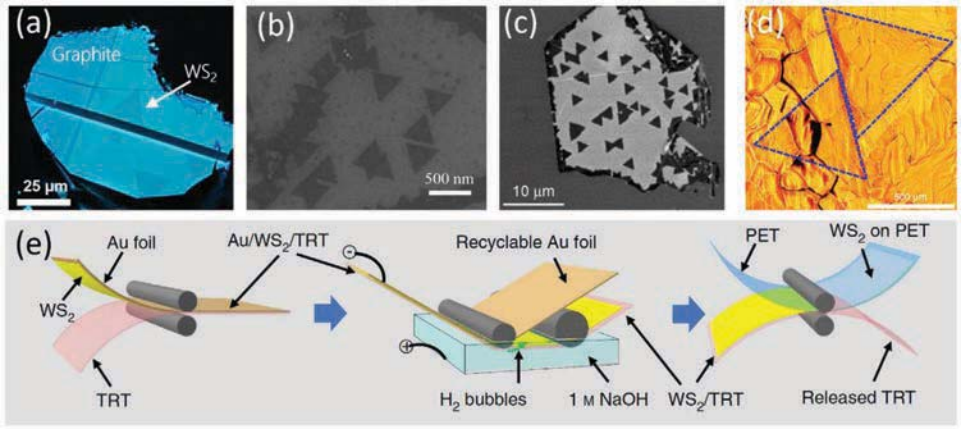

Figure 16. Growth substrates. a) WS_2 grown on graphite. b) WS_2 grown on graphene. c) WS_2 grown on BN. d) WS_2 grown on Au foils. e) Roll-to-roll transfer of WS_2 from Au foils to flexible substrates. a) Reproduced with permission.[128] Copyright 2015, American Chemical Society. b) Reproduced with permission.[129] Copyright 2015, Royal Society of Chemistry. c) Reproduced with permission.[133] Copyright 2014, American Chemical Society. d,e) Reproduced with permission.[70] Copyright 2015, Springer Nature.

et al. extended the method to the synthesis of a huge variety of TMD materials.[136] Adding salts can actually reduce the melting temperature of metal precursors, or form metal oxychlorides, facilitating the growth of 2D TMDs.[136] For WS_2, the formation of volatile WO_2Cl_2 and $WOCl_4$ species is believed to be the reason for the reduced synthesis temperature.[135,137] Except lowering the growth temperature, the crystal size is enlarged as compared with that without using salts,[137] attributable to the increased concentration of gaseous metal species. Recently, it was found that adding Na can enhance the kinetics for the chemical formation of monolayer MoS_2, which can be ascribed to the reduction of energy barrier for MoS_2 growth.[138] Considering the similarity between WS_2 and MoS_2, it may also reduce the growth barrier of growing WS_2 by incorporating Na. In the same way, fluorine is observed to have the ability reducing the energy barrier for WS_2 growth, leading to the formation of large single-crystal WS_2 flakes.[139] In this regard, the elements in the salts, such as Na and Cl, are witnessed to lower the energy barrier for the synthesis of WS_2, with further investigations needed.

3.4.5. The Function of Sulfur

For the growth of WS_2 with WO_3 and S powders, the introduction time and amount of S vapor are very important for controlling the morphology of final products. Rong et al. found that very large single-layer WS_2 triangular domains (up to 370 μm) could be grown with the suitable S introduction time.[140] Yue et al. achieved high-quality synthesis of large single-crystal monolayer WS_2 (≈233 μm) by both tuning the introduction of S and the distance between the sources and substrates.[141] Later, Zafar et al. carried out systematic investigation on the role of introduction time of S and vapor ratio between S and W precursors.[142] A conventional CVD using powder sources is employed in their work (**Figure 17**a). The feeding rate of S can be controlled by tuning its introduction time (Figure 17b). With low feeding rate of S, monolayer WS_2 can be synthesized, while multilayer WS_2 flakes are formed under high feeding rate of S as demonstrated in Figure 17b. In explicit, the S source would lead to the formation of WO_{3-x} that is volatile and further sulfurized into WO_xS_{2-y} on the substrate surface. When a low concentration of WO_xS_{2-y} species is provided to the growth of monolayer WS_2, only atomic scale WS_2 monolayer clusters are yielded on the substrate. While a higher concentration of WO_xS_{2-y} is delivered, multilayer WS_2 growth is resulted. Furthermore, the shape of WS_2 flakes can be controlled by tuning the amount of S used (Figure 17c), which is realized by changing the amount of S powder relative to that of W precursor. Triangle WS_2 flakes are obtained in the S-rich environment, whereas hexagonal WS_2 flakes are grown in the S-deficient environment. The geometrical shape of WS_2 flakes is found to be associated with their different atomic edge arrangements. Usually, the WS_2 flakes adopt a hexagonal shape with alternative S- and W- terminated edges. With the increase of S loading, the probability of S atoms meeting and bonding with W-edges increases, leading to the faster growth of W-terminated edges. As a result, the W-terminated edges become shorter and shorter, producing triangle WS_2 flakes. Also, the size of WS_2 flakes increases with the S exposure time (Figure 17d), which corresponds to the growth duration.

3.4.6. The Function of Hydrogen

Except the etching effect of H_2 on WS_2 flakes,[99] the use of H_2 can as well manipulate the shape of WS_2 flakes during the synthesis as illustrated Zhang et al.[125] Without the introduction of H_2 flow, the WS_2 flakes show the asymmetrical triangular shape with jagged edges under pure Ar carrier gas flow as shown in **Figure 18**a. Since (0001) sapphire with hexagonal symmetry is used as the substrate, the obtained shape of WS_2 flake should not be caused by the lattice anisotropy of Al_2O_3 (0001), but probably be mediated by a dynamic process. With the introduction of H_2 gas flow, nearly equilateral triangular and intersecting triangular shaped single-layer WS_2 with straight edges is grown (Figure 18b). In particular, H_2 chemically reduces WO_3 into volatile WO_{3-x}, making a WO_{3-x} rich environment for the WS_2 growth. Thus, the growth of WS_2 with H_2 flow is considered to be mediated by a kinetic effect, resulting in the thermodynamically stable geometry of a regular triangular shape.

As the (0001) sapphire has the same hexagonal symmetry with the WS_2 basal plane, it is possible to realize epitaxy growth of WS_2 flakes on (0001) sapphires. However, the interaction between WS_2 and sapphire is too weak to achieve the epitaxy growth.[127] Ji et al. revealed that high concentrations of H_2 gas (>40%) during the CVD growth could assist the alignment of triangular WS_2 grains along the *c*-plane sapphire substrate.[127] The shape evolution of WS_2 flakes as a function of H_2 concentration is compiled in Figure 18c. Without the introduction of H_2, the WS_2 flakes have a random orientation. Relatively high H_2 concentrations (>40%) can improve the WS_2 alignment. Furthermore, the introduction of H_2 can reduce the formation of multilayer WS_2 at the center of each domains due to the etching effect of H_2. In contrast, WS_2 flakes grown with pure Ar gas flow show the presence of WO_3 and/or WO_xS_y species as compared with the pure WS_2 flakes formed with the introduction of H_2 gas flow. H_2 can etch the unstable defects during the synthesis, leading to the formation of pure phase WS_2. The Al-rich sapphire surface in H_2-assisted synthesis is the reason for the well-aligned WS_2 flakes. DFT calculations further indicate that the WS_2-sapphire distance for the Al- and O-terminated surface is 0.15 and 0.29 nm, respectively, suggesting the enhanced interaction between WS_2 and Al-terminated sapphire surface for the above phenomenon observed.

3.4.7. Doping

In CVD, substitutional doping can be realized by adding doping precursors in the source materials. Usually, WS_2 exhibits the n-type conducting behavior due to defects formed during synthesis, such as S vacancies. For practical applications, p-doped WS_2 is also needed. Among many possible dopants, Nb doping is widely studies for the p-type doping in WS_2. Gao et al. utilized the $NbCl_5$ precursor for the growth of Nb-doped monolayer WS_2.[143] Due to the low melting point of $NbCl_5$, it is placed near the S powder (**Figure 19**a). As a result, Nb-doped

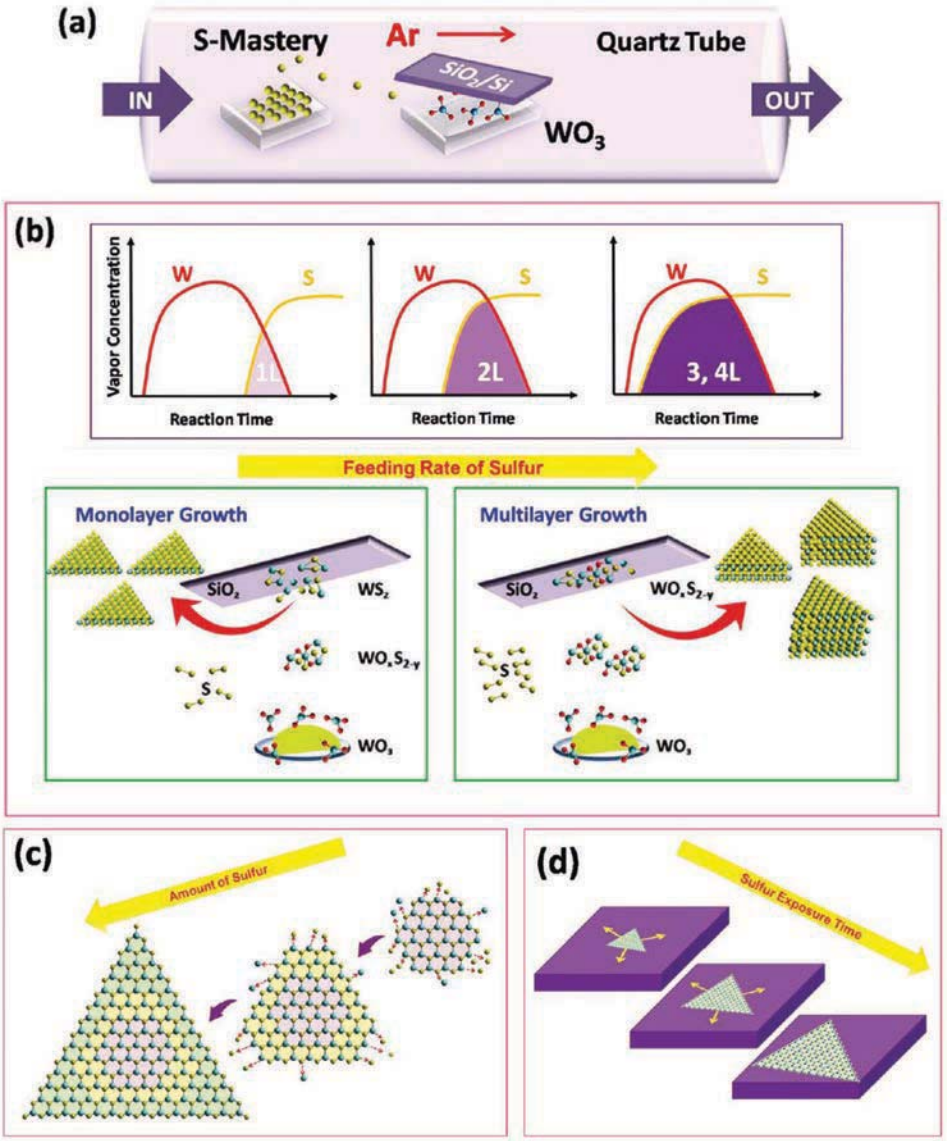

Figure 17. The function of S. a) Schematic illustration of the setup. b) Schematic demonstration of the vapor concentration with different introduction time of S and different growth modes under different feeding rate of S. c) Shape evolution as a function of S content. d) Size evolution as a function of S exposure time. Reproduced with permission.[142] Copyright 2019, John Wiley and Sons.

WS_2 flakes are grown (Figure 19b). The doping concentration is estimated to be about 6.7%. However, this doping scheme had a poor control on the doping concentration. In order to have a better control on the doping concentration, Jin et al. used WO_3, NaCl, and $NbCl_5$ mixture as the metal precursors as presented in Figure 19c.[144] Except lowering the growth temperature, NaCl can also act as a chemical trap of $NbCl_5$, preventing the premature volatilization of $NbCl_5$ before reaching the growth temperature. In addition, self-reduction reaction of Nb^{5+} to Nb^{4+} can occur in the presence of NaCl, which leads to the formation of S—Nb—S bond at low temperatures due to the small Gibbs free energy.[145] In this way, large Nb-doped WS_2 flakes can be grown with well-controlled doping concentration. Alternatively, Feng et al. adopted a three-zone tube furnace and utilized NbO_2 as the doping precursor as illustrated in Figure 19d.[146] The doping concentration of Nb in WS_2 can be varied from 0% to 15% by tuning the amount of NbO_2 and WO_2 powders. Unlike the triangular or hexagonal shape of usually observed WS_2 flakes, the as-grown WS_2 flakes show the rhomboidal shape (Figure 19e). This rhomboidal shape is considered to be originated from its special growth mechanism, where WO_2 is first nucleated on the substrates with a rhomboidal shape and the shape is maintained during the $Nb_{0.15}W_{0.85}S_2$ growth. WS_2 can also form alloy with other TMDs by CVD method, which shows promising applications in electronics and optoelectronics.[147,148] Although much progresses have been made, CVD method using solid-state sources still cannot achieve an excellent control in the doping concentration down to atomic level for WS_2 as compared with other doping schemes in high-performance electronics.

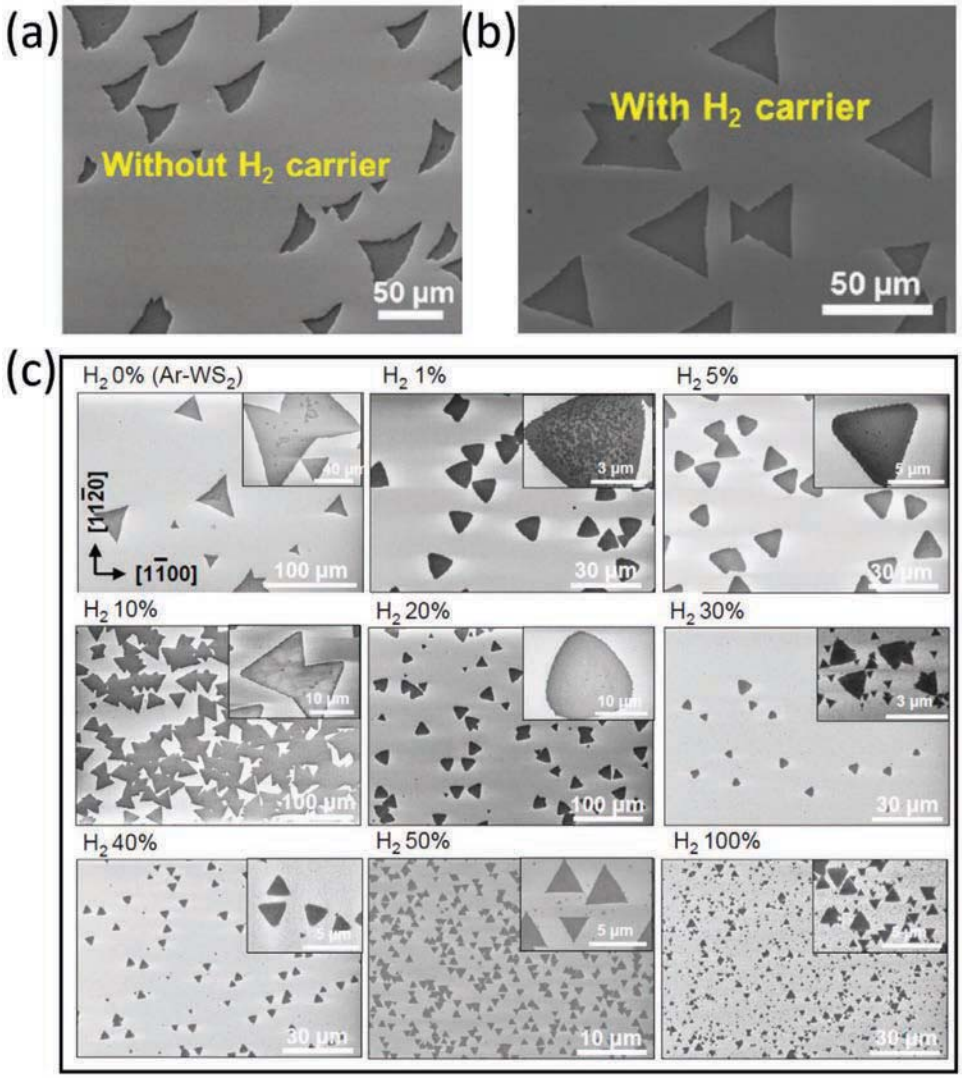

Figure 18. The function of H_2. a) WS_2 flakes grown without H_2 flow. b) WS_2 flakes grown with H_2 flow. c) Alignment evolution of WS_2 flakes as a function of H_2 concentration. a,b) Reproduced with permission.[125] Copyright 2013, American Chemical Society. c) Reproduced with permission.[127] Copyright 2018, American Chemical Society.

The advantages and disadvantages of these vapor-phase methods for the large-area 2D WS_2 synthesis are compiled in **Table 2**. The development of large single domain size and large area WS_2 film are shown in **Figure 20** as well. Apart from the recent advances, there are several unresolved issues, especially to achieve the well-controlled thickness for WS_2 films, with more detailed investigation needed.

4. Applications

4.1. FETs

FETs is the key components in modern integrated circuits (ICs). With the continuous scaling down of the characteristic length of transistors for ICs, many problems appear, such as short channel effect, which will seriously constrain the down scaling of transistors. In order to continue the Moore's law, new device structures and new materials are explored. 2D semiconductors are anticipated to be the promising channel materials than can solve the problems due to their moderate band gap and ultrathin thickness.[149,150] Furthermore, because of the ultrathin, transparent, and high mobility characteristics of 2D semiconductors, they are also promising in thin film transistors for display applications.[151] In this regard, the research on 2D semiconductors in FETs is intensively studied. Among many candidates, 2D WS_2 is predicted to have the superior electron mobility than most of the counterparts in TMDs, being advantageous for high-performance transistors.[22,60,152,153] Owing to the relatively large band gap of 2D WS_2, their transistors always show a large ON/OFF current ratio (> 10^5).[154–156] Nevertheless, the measured mobility of WS_2-based transistors is still low as compared with the theoretical prediction, especially for the CVD-synthesized 2D WS_2 channel. There are many factors that can affect the performance of WS_2 transistors, such as defects, dielectric, environmental adsorbates, etc. To further improve

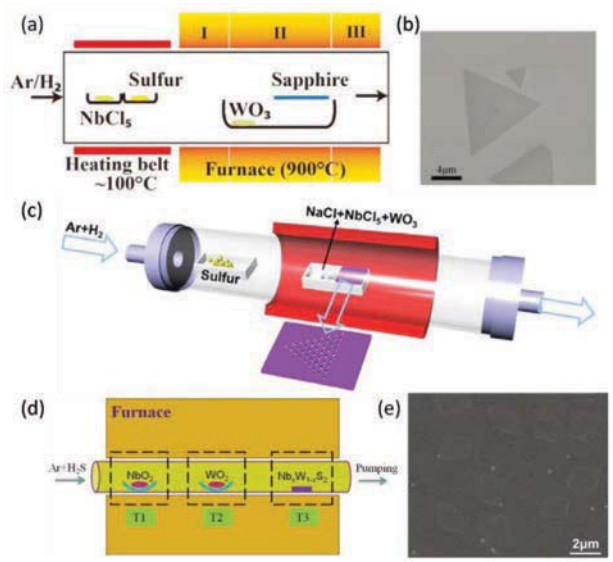

Figure 19. Doping strategies for CVD using solid-state sources. a) Schematic of the setup using $NbCl_5$ as the doping precursor. b) Nb-doped WS_2 triangular flakes. c) Schematic of the setup for doping with NaCl. d) Schematic of a multi-zone furnace for Nb doping. e) SEM image of the Nb-doped WS_2 flakes. a,b) Reproduced with permission.[143] Copyright 2016, John Wiley and Sons. c,d) Reproduced with permission.[144] Copyright 2019, American Chemical Society. e) Reproduced with permission.[146] Copyright 2016, Royal Society of Chemistry.

the performance of WS_2 transistors, various methods are implemented, including contact engineering, dielectric engineering, doping, and so on. In this section, the discussion will be divided into sub-sections to go over the details in the area of environment effect, material quality engineering, interfacial engineering, and contact engineering sequentially.

4.1.1. Environment Effect

Actually, the adsorbates from the environment can significantly affect the performance of 2D WS_2-based transistors. The absorption of H_2, O_2, and H_2O on the surface of WS_2 channels is observed to result in the p-type doping.[157] Therefore, 2D WS_2-based transistors operated in air without any passivation would give the weak n-type or p-type conducting behavior.[122,155] Moreover, the quantity of adsorbates is determined by the pressure. Ovchinnikov et al. studied the pressure-dependent electrical behavior of WS_2-based transistors in details.[155] The transfer curves of a bilayer WS_2 transistor under different pressures are shown in **Figure 21**a. Obviously, the conducting behavior changes from the weak p-type to the strong n-type as the pressure decreases, indicating the strong effect of adsorbates on the electrical properties of 2D WS_2 transistors. Due to the strong effect of ambient molecules, most of the electrical properties of 2D WS_2 transistors reported in the literature are recorded under vacuum in order to eliminate the impact of adsorbates.

4.1.2. Material Quality Engineering

The material quality of WS_2 is important for channels of high-performance transistors. The structural defects, such as S vacancy, is the intrinsic reason for drastically reduced carrier mobility.[158,159] Thus, the structural defects have to be repaired in order to realize high mobility 2D WS_2 transistors. Jiang et al. found that the S vacancy can be effectively repaired by N_2 plasma treatment.[159] With the N_2 plasma cure, N atoms preferentially fill the S vacancies and form W—N bonds due to the more stable adsorption energy. As shown in Figure 21b, the performance of the multilayer WS_2 transistor is much enhanced by N_2 plasma treatment. The corresponding electron mobility increases from 29.7 to 184.2 $cm^2\ V^{-1}\ s^{-1}$, while the ON/OFF ratio increases from 10^3 to 10^6. In addition, the electrical contact quality is improved. The untreated transistor shows the obvious Schottky contact with nonlinear I_{DS}–V_{DS} curves near 0 V (Figure 21c), whereas the N_2 plasma-treated device yields the ohm-like contact with linear I_{DS}–V_{DS} curves near 0 V (Figure 21d). The enhanced contact quality is attributed to the changes of Fermi level upon N_2 plasma treatment. The enhanced carrier mobility can be ascribed to the reduced charge scattering from S vacancies and reduced effective electron mass with N doping.[159] Moreover, this method is effective for a wide range of thicknesses as shown in Figure 21e. Thiol chemical functionalization can also be used to repair S vacancies and to improve the interface, leading to the significant reduction of charge impurities and traps.[158,160] As depicted in Figure 21f, the mobility of single-layer WS_2 transistor is much enhanced

Table 2. Comparison between different synthesis methods.

Methods		Single crystal size	Thickness control	Film uniformity
Sulfurization of seed film	Thermal/e-beam evaporation	10–50 nm	Good	Moderate
	Magnetron sputtering	10–50 nm	Good	Moderate
	ALD	10–50 nm	Excellent	Good
	Spin coating	10 nm to 200 μm	Moderate	Moderate
Vapor source method	MOCVD	200 nm	Poor	Good
	ALD	10 nm to 50 μm	Good	Moderate
	Conventional gas phase CVD	100 nm to 10 μm	Poor	Poor
Solid-state sources CVD		1 μm to 1 mm	Poor	Good

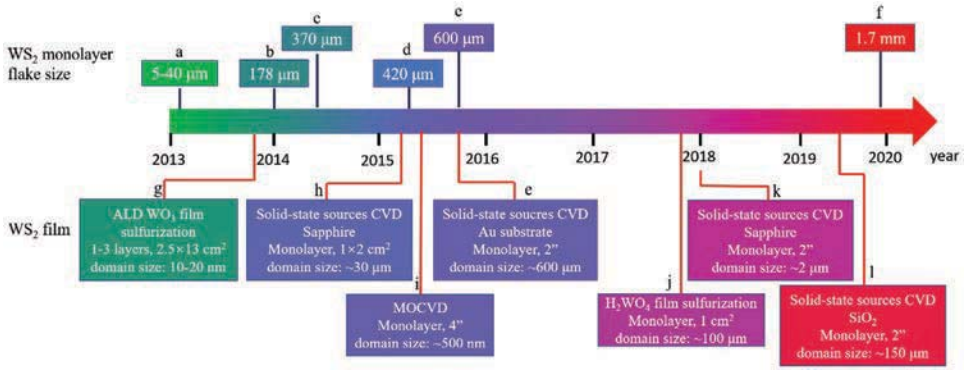

Figure 20. Schematic of the development of vapor phase synthesis of WS_2. The upper side indicates the development of single domain size, the lower side indicates the development of the growth of large area WS_2 film by various methods. a) Reproduced with permission.[125] b) Reproduced with permission.[48] c) Reproduced with permission.[140] d) Reproduced with permission.[134] e) Reproduced with permission.[70] f) Reproduced with permission.[114] g) Reproduced with permission.[86] h) Reproduced with permission.[122] i) Reproduced with permission.[99] j) Reproduced with permission.[91] k) Reproduced with permission.[49] l) Reproduced with permission.[252]

after the thiol chemical functionalization.[158] The low temperature mobility increases from 140 to 337 $cm^2\ V^{-1}\ s^{-1}$, and the room temperature mobility increases from 49 to 83 $cm^2\ V^{-1}\ s^{-1}$.

4.1.3. Interfacial Engineering

The typical mobility of 2D WS_2 transistors is always much lower than the ones of theoretical prediction and bulk materials. The defect states in the SiO_2 layer on the substrate can lead to the localization of charge carriers in TMDs, which is one of the main factors limiting the device mobility.[161] Thus, other substrates with reduced defect states are preferred. Hexagonal BN is an ideal choice here because of its atomically flat surface, large band gap, and low density of charge impurities.[162,163] In fact, the performance of 2D WS_2 transistors is much enhanced when using BN as the substrate.[164,165] Iqbal et al. systematically studied the effect of BN on the performance of monolayer WS_2 transistors.[165] Generally, three kind of structures were adopted: WS_2 on SiO_2, WS_2 on BN, and WS_2 sandwiched between two BN layers (**Figure 22**a). Even though the transistors show almost the same ON/OFF current ratio, their electron mobility values are different accordingly (Figure 22b–d). With only the BN substrate, the mobility increases from 80 to 163 $cm^2\ V^{-1}\ s^{-1}$. By sandwiching the WS_2 between two BN layers, the mobility increases to 185 $cm^2\ V^{-1}\ s^{-1}$. Temperature-dependent mobility also indicates the enhanced mobility with the sandwiched structure (Figure 22e). The sandwich structure does not only provide a flat and low-defect substrate, but also give a protection layer to minimize unwanted environmental effects. The

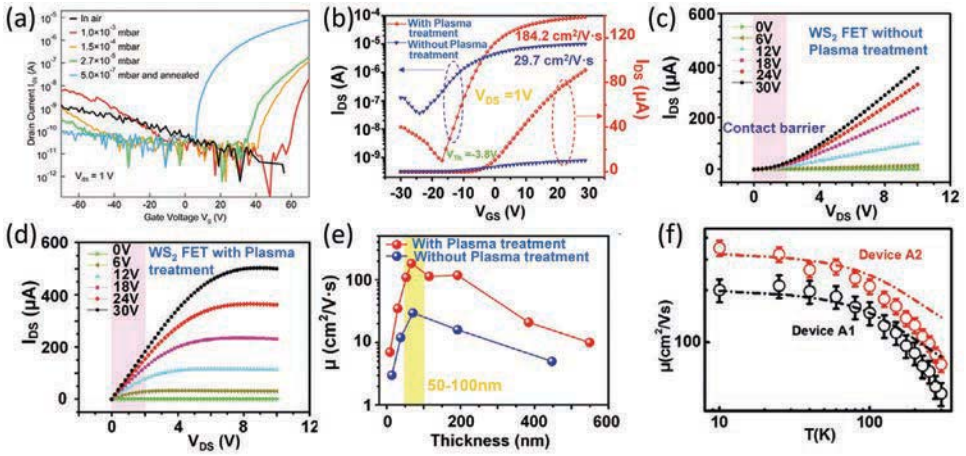

Figure 21. Pressure and WS_2 quality-dependent electrical properties of WS_2 transistors. a) Pressure-dependent transfer curves of a bilayer WS_2 transistor. b) Transfer curves of multilayer WS_2 transistors with and without N_2 plasma treatment. c) Output curves of a multilayer WS_2 transistor without N_2 plasma treatment. d) Output curves of a multilayer WS_2 transistor with N_2 plasma treatment. e) Mobility of WS_2 transistors with and without N_2 plasma treatment as a function of thickness. f) Mobility of WS_2 transistors with (device A2) and without (device A1) the thiol chemical functionalization as a function of temperature. a) Reproduced with permission.[155] Copyright 2014, American Chemical Society. b–e) Reproduced with permission.[159] Copyright 2019, John Wiley and Sons. f) Reproduced with permission.[158] Copyright 2015, John Wiley and Sons.

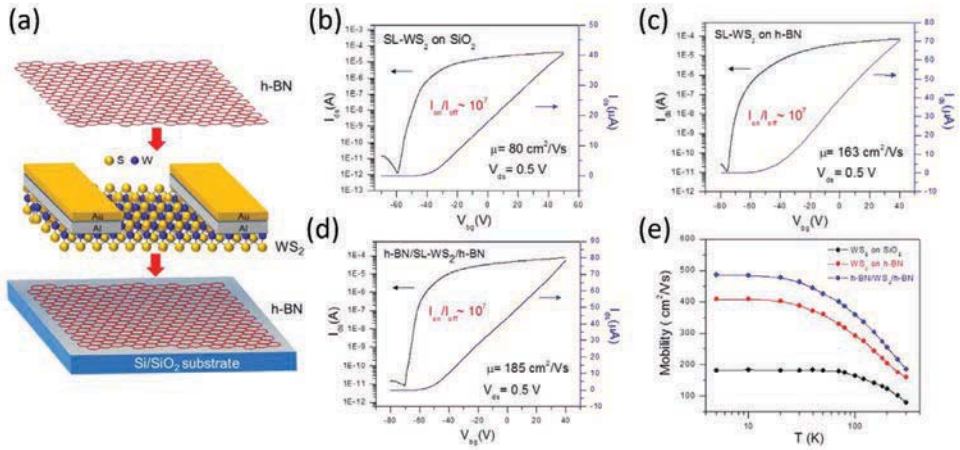

Figure 22. Interfacial engineering. a) Schematic of the sandwiched monolayer WS_2 transistor. b–d) Transfer curves of the WS_2 transistors with different structures at room temperature. e) Mobility as a function of temperature. Reproduced with permission.[165] Copyright 2015, Springer Nature.

highest mobility value of the optimal device structure is found to be 214 $cm^2\ V^{-1}\ s^{-1}$. Apart from BN, high-*k* dielectrics can also be used to reduce the interfacial charge traps, leading to the increased mobility.[158]

4.1.4. Contact Engineering

The electrical contact property is important for WS_2 transistors, which determines the efficiency of charge injection/collection between electrodes and WS_2 channels. For ideal transistors, ohmic contact is preferred. However, it is difficult to realize ohmic contact in 2D materials-based transistors.[166–169] The interfacial states always lead to Fermi pinning, which makes it impossible to match the work function of WS_2 channels by choosing metal electrodes with the appropriate work function. In this regard, various methods have been adopted to alleviate this problem.

Annealing: Annealing can improve the contact quality between 2D materials and metals, reducing the contact resistance with increased carrier mobility. Ovchinnikov et al. found that vacuum annealing can reduce the contact resistance, leading to enhanced carrier mobility.[155] As shown in **Figure 23**a, the mobility of single-layer WS_2 devices increases with the increasing annealing time for both two- and four-terminal device configuration. The four-terminal mobility reaches a saturation value of ≈40 $cm^2\ V^{-1}\ s^{-1}$ after 60 h annealing, whereas the two-terminal mobility continues to improve gradually. Kim et al. found that more than 5000 times reduction in the contact resistance of WS_2 transistors with Ti electrodes can be realized by the high pressure hydrogen annealing (HPHA).[170] After HPHA treatment, the average Schottky barrier height (SBH) reduces from 0.18 to 0.13 eV. The possible reason for the reduction of SBH is associated with the hydrogenation reaction at the Ti–WS_2 interface, which results in the Fermi-level depinning like behavior.

Graphene Electrodes: The Fermi energy of graphene can be tuned by applying a gate voltage that can be used to obtain a low SBH. In addition, graphene is a 2D material free of dangling bonds. Thus, the contact of graphene with WS_2 does not induce any interfacial states, preventing the occurrence of Fermi level pinning. Aji et al. used multilayer graphene as electrodes and the performance of such monolayer WS_2 transistors was much enhanced.[171] As compared with Ti/Au electrodes, WS_2 transistor with multilayer graphene shows much enhanced performance as given in Figure 23b–d. The average carrier mobility of the device with multilayer graphene electrodes is 27 $cm^2\ V^{-1}\ s^{-1}$ with the highest value of 50 $cm^2\ V^{-1}\ s^{-1}$. The average mobility of the device with Ti/Au electrodes is only ≈5 $cm^2\ V^{-1}\ s^{-1}$. This much-enhanced mobility is attributed to the tunable Fermi level of multilayer graphene as presented in Figure 23e.

Doping: Doping can move the Fermi level toward conduction (n-type doping) or valance (p-type doping) band edge. The effective barrier height is then reduced when metal contacts with the highly doped semiconductor due to carrier tunneling in addition to thermionic emission (Figure 23f).[172] Because the intrinsic defects of WS_2 always lead its n-type conductivity, n-type doping is hence widely utilized as a strategy to reduce the contact resistance between WS_2 channels and metal electrodes.[52,53,172,173] Khalil et al. used LiF as a n-dopant for few layers WS_2 and found that the contact resistance of subsequently fabricated devices could be much reduced as compared with the undoped ones.[52] As shown in Figure 23g, the corresponding contact resistance reduces from 31.3 to 0.9 kΩ μm. Furthermore, the mobility significantly increases from 13.2 to 34.7 $cm^2\ V^{-1}\ s^{-1}$ due to the improvement of source–drain current. Other dopants, such as KI and Cu,[53,173] can also lead to n-type doping that reduces the contact resistance with improved mobility.

Metal Interfacial Layer: The direct metal deposition can lead to the substantial damage in 2D semiconductors due to the kinetic energy transfer or chemical reaction between metal atoms and 2D semiconductors, again leading to Fermi level pinning.[174–176] In order to reduce the damage caused by direct deposition of metal, Wang et al. used low melting point metal of In as a buffer layer, which could yield the formation of clean interface between In and 2D semiconductors without any

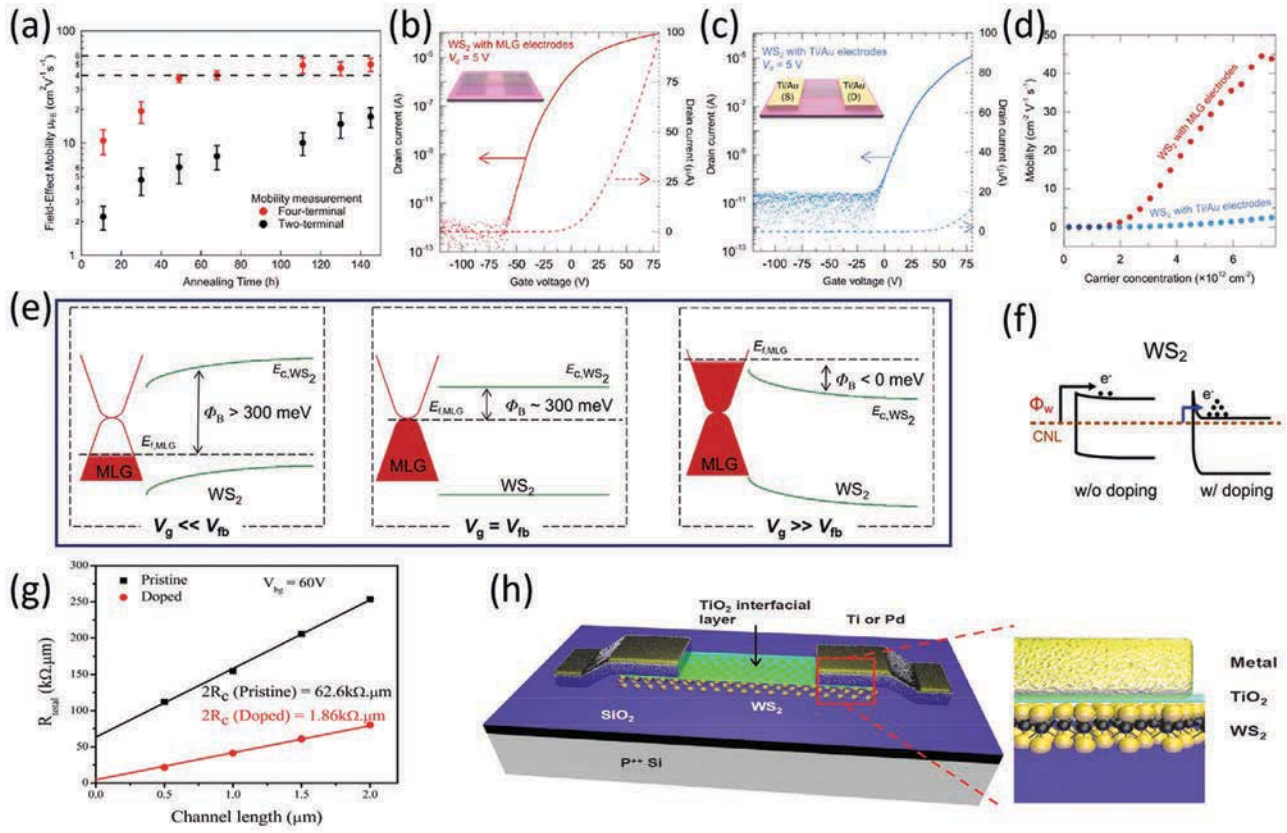

Figure 23. Contact engineering. a) Electron mobility as a function of annealing time for a single-layer WS_2 transistor. b) Transfer curves of monolayer WS_2 transistor with graphene electrodes. c) Transfer curves of monolayer WS_2 transistor with Ti/Au electrodes. d) Electron mobility as a function of carrier density for different electrical contacts. e) Schematic of the band alignment evolution with gate voltage. f) Schematic of the band alignment of metal with WS_2 with and without n-type doping. g) Resistance as a function of channel length. h) Schematic of the WS_2 transistor with a TiO_2 interfacial layer. a) Reproduced with permission.[155] Copyright 2014, American Chemical Society. b–e) Reproduced with permission.[171] Copyright 2017, John Wiley and Sons. f) Reproduced with permission.[172] Copyright 2014, American Chemical Society. g) Reproduced with permission.[52] Copyright 2015, American Chemical Society. h) Reproduced with permission.[178] Copyright 2016, John Wiley and Sons.

damage.[174] As a result, the contact resistance is much reduced as compared to conventional electrode deposition. The few layers WS_2 transistor with In electrodes shows much enhanced performance over the ones with Ti contact. The device mobility increases from 1.2 ± 1 cm^2 V^{-1} s^{-1} (devices with Ti contact) to 83 ± 10 cm^2 V^{-1} s^{-1} (devices with In contact). Furthermore, the In metal usually forms stable alloys readily with other metals, which can be used to adjust the work function of electrodes in order to facilitate efficient carrier injection. Recently, Liu et al. found that the deposition of a thin layer of Cu between WS_2 and Ti/Au metals could reduce the contact resistance because of the lowering of SBH.[173] This SBH reduction is mainly attributed to a synergetic interaction among exchange repulsion, covalent bonding, and charge redistribution near the interface. Importantly, the localized Cu contact also results in a strong n-type doping in WS_2 at the contact region, reducing the contact resistance.

Dielectric Interfacial Layer: Fermi level pinning is difficult to be avoided using the conventional metal contact.[176,177] With the aim to minimize this adverse effect, an ultrathin dielectric interfacial layer is inserted between metals and 2D semiconductors.[178–182] Park et al. used ALD TiO_2 as the interfacial layer (Figure 23h) and observed that a low SBH could be obtained after the introduction of this interfacial layer due to Fermi level depinning.[178] Because of this depinning, both n- and p-type WS_2 transistors can be obtained by simply choosing metals with the appropriate work function, such as Ti for n-type transistors and Pd for p-type transistors.

Edge Contact: Van der Waals 2D materials have layered structures; therefore, in principle, they have the passivated surface without any dangling bonds. A van der Waals gap would exist between 2D semiconductors and metals when adopting the top contact scheme, which becomes a barrier for charge injection.[166] In this case, edge contact is preferred because it can eliminate the van der Waals barrier owing to the existence of covalent bonding between 2D semiconductors and contact materials in the lateral direction.[183] In any case, the direct realization of clean edge contact for TMDs is difficult because of its ultrathin nature.[184] In order to realize this edge contact scheme, Guimarães et al. grew monolayer WS_2 between two monolayer graphene electrodes by CVD.[185] The contact resistance of the edge contacted monolayer WS_2 is only ≈30 kΩ μm that is much reduced as compared with that of top contact devices.

Table 3. Performance parameters of typical WS_2 transistors.

Thickness	Electrode	Dielectric/structure	Contact resistance [kΩ μm]	Room temperature mobility [$cm^2 V^{-1} s^{-1}$]	ON/OFF ratio	Ref.
70 nm	Ti/Au	PMMA/WS_2/Al_2O_3/SiO_2	-	29.7	10^3	[159]
				184.2 (N_2 plasma processed)	10^6	
Monolayer	Ti/Pd	SiO_2	-	25	-	[158]
		Al_2O_3/SiO_2		49	-	
		MPS/Al_2O_3/SiO_2		83	-	
Monolayer	Al/Au	SiO_2	-	80	10^7	[165]
		BN/SiO_2		163	10^7	
		BN/WS_2/ BN/SiO_2		214	10^7	
Monolayer	Au	SiO_2	-	≈40	10^5	[155]
Bilayer				≈33		
Monolayer	Ti/Au	SiO_2	-	≈5	10^5	[171]
	Graphene			27	10^8	
5.2 nm	Cr/Au	SiO_2	31.3	13.2	4.8×10^5	[52]
			0.9	34.7 (doped)	1.0×10^6	
Few-layer	Ti/Au	SiO_2	-	1.2	10^5	[174]
	In/Au		2.4	83	10^6	
Few-layer	Ni/Au	SiO_2	0.7	60 (Cl-doped)	10^7	[172]
Few-layer	Ti/Au	SiO_2	2.2×10^6	4.9	1.6×10^6	[173]
	Ti/Au		7.4×10^3	21.9 (Cu-doped)	2.5×10^6	
	Cu/Ti/Au		10^3	26.3	9.1×10^6	

To have a better understanding of these WS_2 transistors, the performance parameters are extracted from typical literatures as given in **Table 3**.

4.2. Memristors

A memristor is a two-terminal device, where its resistance depends highly on the magnitude and polarity of the applied voltage as well as the time period of the applied voltage.[186–188] The behavior of a memristor is essentially similar to biological synapses in neural networks.[186,189] Thus, it shows potential applications in neuromorphic computing.[186,190] WS_2 has been utilized in memristors, which exhibit excellent device performance.[191–193] For example, Yan et al. fabricated memristors using WS_2 flakes that give fast switching time and low program current in the ON state.[193] The structure of a memristor is depicted in **Figure 24**a, in which the Pd electrode is connected to the positive electrode and the Pt electrode is grounded. After detailed device measurement, the clear resistance switching behavior is observed (Figure 24b). The device has the fast switching speed from high resistive state (HRS) to low resistive state (LRS) (within 13 ns) and vice versa (within 14 ns). Furthermore, the energy consumptions of the device are low for both HRS to LRS (299.8 fJ) and vice versa (125.6 fJ). Notably, the device can mimic basic biological synaptic functions, showing great potentials in low power neuromorphic computing. The resistance switching behavior is proposed to be dominated by the generation of S and W vacancies and electron hopping between vacancies. The S and W vacancy defect states are located at deep levels based on the DFT calculation, which is responsible for the low leakage current. For improving the performance of memristors, hybrid structures

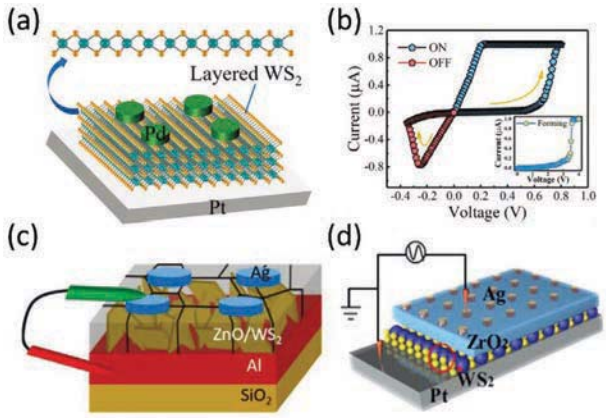

Figure 24. WS_2-based memristor devices. a) Schematic of the WS_2 flakes-based memristor. b) Current–voltage sweep. c) Schematic of the ZnO-vertical aligned WS_2 memristor. d) Schematic of the ZrO_2-WS_2 memristor. a,b) Reproduced with permission.[193] Copyright 2019, John Wiley and Sons. c) Reproduced with permission.[191] Copyright 2019, John Wiley and Sons. d) Reproduced with permission.[192] Copyright 2019, American Chemical Society.

are adopted, such as ZnO-vertical aligned WS_2 (Figure 24c)[191] and Zr_2O-WS_2 (Figure 24d).[192] In specific, the vertically aligned 2D layered structure of WS_2 confined the generation/redistribution of oxygen vacancies within the well-defined path and shape, leading to good cycle-to-cycle (≈10^4) and device-to-device reproducibility.[191] The ZrO_2-WS_2 stacked structure memristors exhibit the highly stable resistance switching and concentrated ON and OFF state voltage distribution, high speed (≈10 ns), and excellent endurance (>10^9 cycles).[192] These superior properties are mainly ascribed to the different ion transport rates of ZrO_2 and WS_2, which limits the rupture/rejuvenation of conductive filaments to the bilayer interface region, greatly reducing the randomness of conductive filaments of the memristor.

4.3. Optoelectronics

Due to the excellent optical properties of WS_2, it shows promising applications for optoelectronics, such as photodetectors, LEDs, lasers, and optical modulators.

4.3.1. Photodetectors

Photodetector is a device that converts light signals into electrical signals, which is one of the key components in optoelectronic systems. Because of the strong light–matter interaction and high carrier mobility of WS_2, it has attracted much attention for photodetectors.[194] By reason of the ultrathin nature of single-layer WS_2, the photoresponsivity of monolayer WS_2 photodetector is low, on the orders of several mA W^{-1}.[49,122,195,196] Similar to its electrical properties, the photoresponse of monolayer WS_2 is also sensitive to environment (**Figure 25**a,b).[122] The photocurrent measured under vacuum is larger than that in ambient. This reduced photocurrent in ambient is caused by the adsorbates from ambient, which drastically reduces the lifetime of photogenerated carriers. The enhanced photocurrent measured under vacuum is associated with the increased photo-carrier lifetime. However, the corresponding response speed is reduced because the response time is proportional to photo-carrier lifetime. In addition, the photocurrent can be modulated by gate voltage (Figure 25a), where this modulation of photoresponse is mainly caused by the increased carrier mobility and reduced contact barrier at the contact under large positive gate voltages.[197–199] Furthermore, photogating effect also contributes to the enhanced photoresponse that is clearly manifested from the shift of transfer curves under light illumination (Figure 25a).[194,200,201] As a result, a large photoresponsivity of 22.1 A W^{-1} can be realized in single-layer WS_2 device.[195] Because the contact barrier constrains the collection of photo-carriers in a photoconductor, a low contact barrier is highly preferred for WS_2-based photodetectors. Unlike metal contact, the work function of graphene can be well controlled by electrostatic gating such that graphene can then be employed as low contact barrier electrodes for WS_2. Tan et al. used graphene as electrodes for monolayer and bilayer WS_2 photodetectors (Figure 25c). It is evident that large photoresponsivities could be realized for both monolayer (2.5 A W^{-1}) and bilayer (3.5 A W^{-1}) WS_2 photodetectors under high illumination power density of 2.5×10^7 mW cm^{-2}.[202] The contact barrier can as well be lowered under light luminescence for short channel photodetectors.[27] Remarkably, only the photo-carriers near the contact interface would contribute to fill the traps states and lower the Schottky barrier. In this case, the longer channel length adds additional series resistance to photodetectors, leading to reduced device performance (Figure 25d). With a channel length of 200 nm, Fan et al. achieved a high photoresponsivity of 20 A W^{-1} under a large source–drain bias

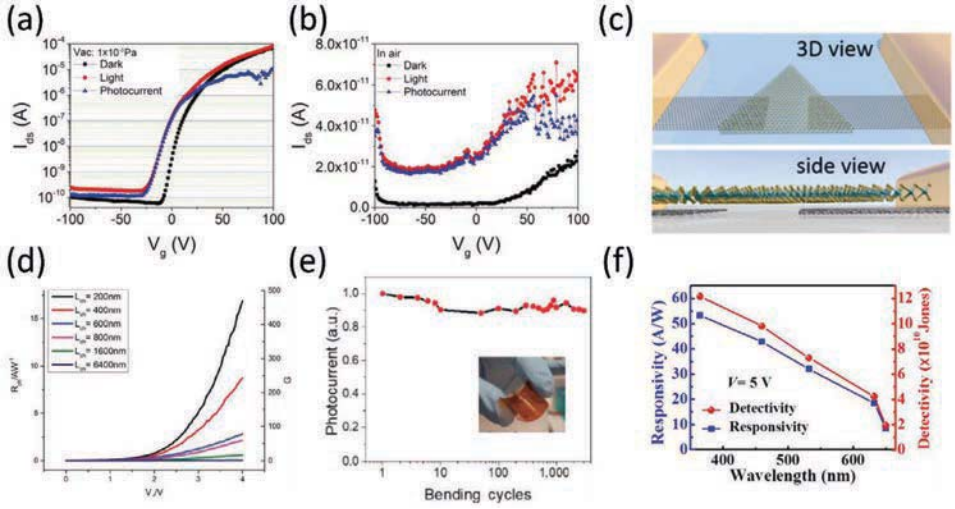

Figure 25. WS_2 photodetectors. a) Transfer curves of the monolayer WS_2 phototransistor measured under vacuum. b) Transfer curves of the monolayer WS_2 phototransistor measured in ambient. c) Schematic of the graphene contacted monolayer WS_2 photodetector. d) Responsivity as a function of bias voltage and channel length. e) Normalized photocurrent as a function of bending cycles. f) Responsivity and detectivity as a function of wavelength. a,b) Reproduced with permission.[122] Copyright 2015, Royal Society of Chemistry. c) Reproduced with permission.[202] Copyright 2016, American Chemical Society. d) Reproduced with permission.[27] Copyright 2016, John Wiley and Sons. e) Reproduced with permission.[49] Copyright 2018, Springer Nature. f) Reproduced with permission.[206] Copyright 2016, Springer Nature.

(4 V) for monolayer WS_2 photodetectors.[27] Originating from the good flexibility of monolayer WS_2, it is also suitable for flexible photodetectors. Lan et al. found that monolayer WS_2 flexible photodetectors yield the excellent robustness to bending, which can maintain 89% of their photocurrent after 3000 bending cycles (Figure 25e).[49] As compared with atomically thin WS_2, photodetectors with thick WS_2 show better photoresponse that is partly due to enhanced optical absorption and carrier mobility of thick films.[203–206] For example, Zeng et al. showed that the photodetector with the 25 nm thick polycrystalline WS_2 film exhibited a responsivity of 53.3 A W^{-1} at 365 nm (Figure 25f).[206]

In order to improve the performance of WS_2-based photodetectors, various kinds of device structures are adopted. Since WS_2 is a kind of van der Waals layered material, it can be used to fabricate heterostructures without considering the limitation of lattice mismatch between WS_2 films and substrates.[207] Thus, WS_2-based heterostructure photodetectors are widely investigated. 2D–2D heterostructures are observed to provide the excellent hetero-interface due to both of the passivated surfaces of each 2D materials, delivering excellent photoresponse.[208–212] For example, Xue et al. developed a scalable production technique for WS_2-MoS_2 stacked heterostructure arrays and achieved heterostructure photodetectors (**Figure 26**a) with good performance with a high responsivity of 2.3 A W^{-1} at 450 nm.[212] At the same time, graphene has very large mobility, which can be used as the carrier transport layer in a photodetector. Lan et al. found that graphene-WS_2 heterostructure photodetectors indeed exhibited much enhanced photoresponse with a high responsivity of 950 A W^{-1}.[130] Furthermore, with an ionic gating, the photoresponsivity of graphene-WS_2 heterostructures is even higher (10^6 A W^{-1}) with fast response as demonstrated by Mehew et al.[213] The highly mobile ions and the nanoscale Debye-length dimension of ionic polymers can screen off charge traps and tune the Fermi level of graphene, leading to the much enhanced responsivity and speed. Because of the passivated surface of WS_2, it can integrate with 3D materials as well, which can combine the excellent optoelectronic properties of both materials, leading to enhanced performance. Besides, organic–inorganic perovskite materials have excellent optical properties.[214–217] Combining the advantages of both perovskite materials and WS_2 films, high-performance photodetector can be achieved. Ma et al. fabricated WS_2-$CH_3NH_3PbI_3$ heterostructure photodetectors (Figure 26b), where they showed excellent photoresponse with the high responsivity (17 A W^{-1}), on/off ratio ($\approx 10^5$), and fast response (7.5 ms).[218] These enhanced photoresponse are anticipated to come from the improve crystallinity of $CH_3NH_3PbI_3$ directly grown on WS_2 as well as the efficient interfacial charge transfer.

To expand the photosensitive spectrum, large band gap and small band gap materials can be stacked with WS_2 to enhance its photoresponse to short wavelength and long wavelength irradiation. For instance, stacking monolayer WS_2 on ZnO films can enhance the UV photoresponse several times as compared with ZnO photodetectors.[219] This enhanced UV response is attributed to the type I heterostructure obtained so that photocarriers in ZnO can transfer effectively to the WS_2 side and get collected by the electrode. Spin coating a layer of PbS quantum dots on single-layer WS_2 can also expand the response spectrum to IR region. Yu et al. demonstrated that WS_2-PbS photodetectors (Figure 26c) exhibited a high responsivity of 14 A W^{-1} at 808 nm with a bandwidth of 396 Hz.[220] Integrating 2D materials with Si as well provides a facile approach to fabricate high-performance photodetectors by taking the advantages of both materials. In this manner, 2D-Si heterostructure photodetectors have been intensively investigated.[221] The photodetector based on WS_2-Si heterostructures (Figure 26d) has been constructed by Lan et al., which shows the excellent photodetection performance with a maximum responsivity of 5.7 A W^{-1} at 660 nm and a fast response speed of 670 μs.[84]

Moreover, to enhance the photoresponsivity and reduce the dark current, floating gate memory structure is proposed for

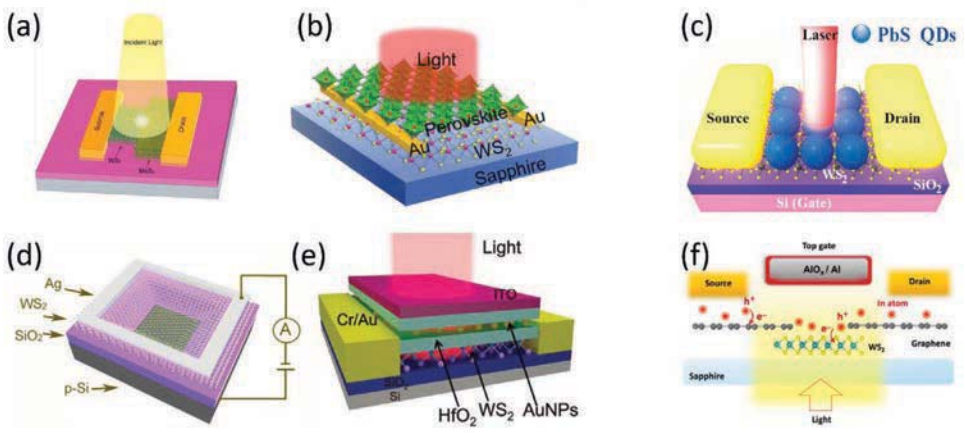

Figure 26. Schematic of different kinds of WS_2-based photodetectors. a) WS_2-MoS_2 heterostructure. b) WS_2-$CH_3NH_3PbI_3$ heterostructure. c) WS_2 decorated with PbS quantum dots. d) WS_2-Si heterostructure. e) WS_2 floating gate photodetector. f) WS_2 decorated with In atoms with edge contacted graphene electrode. a) Reproduced with permission.[212] Copyright 2016, American Chemical Society. b) Reproduced with permission.[218] Copyright 2016, John Wiley and Sons. c) Reproduced with permission.[220] Copyright 2017, American Chemical Society. d) Reproduced with permission.[84] Copyright 2016, American Chemical Society. e) Reproduced with permission.[222] Copyright 2016, John Wiley and Sons. f) Reproduced with permission.[225] Copyright 2019, American Chemical Society.

Table 4. Parameters of some typical photodetectors based on WS_2 from literatures.

Thickness	Electrode material	V_{ds} [V]	V_{gs} [V]	L [μm]	Environment	λ [nm]	R [A W^{-1}]	D^* [Jones]	Speed [s]	Ref.
Monolayer	Al	20	0	30	Ambient	532	2.4×10^{-4}	-	$<4.5 \times 10^{-3}$	[122,195]
		20	0		Vacuum		1.2×10^{-2}	-	0.15	
		20	60		Vacuum		22.1	-	0.19	
Monolayer	Ti/Au	10	0	2	Ambient	532	5.2×10^{-4}	4.9×10^{9}	$<5.6 \times 10^{-4}$	[49]
							5.0×10^{-3}	4.0×10^{10}	$<5.6 \times 10^{-4}$	
Monolayer	Graphene	5	0	0.2	Ambient	532	2.5	9.9×10^{10}	-	[202]
Bilayer							3.5	1.6×10^{10}	-	
Monolayer	Au	4	0	0.2	Ambient	532	20	-	-	[27]
Monolayer	Graphene	5	30	1	Ambient	532	121	-	-	[256]
6 nm	Ti/Au	30	0	50	Vacuum	458	2.2×10^{-5}	-	5.3×10^{-3}	[76]
20 nm	Ti/Au	0.02	−2	1	Ambient	630	0.27	-	-	[203]
60 nm	Pt	9	0	100	Ambient	635	0.51	1.9×10^{9}	4.4	[205]
					Vacuum		0.7	2.7×10^{9}	9.9	
25 nm	Ti/Au	5	0	100	Ambient	365	53.3	1.22×10^{11}	-	[206]
4 nm	Cr/Au	0.02	0	1.1	Vacuum	520	1090	3.5×10^{11}	10.7	[222]

building photodetectors.[222] As shown in the device structure in Figure 26e, Au nanoparticles are placed between tunneling and blocking dielectric layers, which act as a charge trapping layer, suppressing the dark current. As a result, the photodetector shows the excellent performance with an ultralow dark current (10^{-11} A), a high photoresponsivity (1090 A W^{-1}), and a high detectivity (3.5×10^{11} Jones). The optical absorption of WS_2 can be much enhanced by metal nanoparticle-induced plasmonic effect.[223] Thus, the photoresponse of WS_2 can be improved when incorporated with metal nanoparticles. In particular, Liu et al. found that Au nanoparticles decorated WS_2 films exhibited enhanced photoresponse with a high responsivity of 1050 A W^{-1} at 590 nm.[224] In order to reduce the contact resistance and enhance the photogating effect, Yeh et al. designed a special structure (Figure 26f), which consists of edge-connected graphene electrodes and In atoms decorated WS_2 films.[225] This device exhibits a large gain (6.3×10^3), a large responsivity (2.6×10^3 A W^{-1}), and an ultrafast response speed (40–65 μs). In atoms decorated on WS_2 can trap photogenerated holes, leading to a large photogating effect.

To have a better understanding of these WS_2 photodetectors, the performance parameters of WS_2 photodetectors and WS_2-based heterostructure photodetectors are extracted from typical literatures as given in **Tables 4** and **5**.

4.3.2. LEDs

Monolayer WS_2 is a direct band gap material with large exciton binding energy that are ideal for LEDs. Because of the extremely large gate capacitance of the ionic liquid gated FET, WS_2 transistor can be gated into n- and p-type conductivity at low gate voltages.[226] In this case, bipolar injection can be realized in ionic gated transistors as shown in **Figure 27**a. Under the bipolar injection condition, obvious electroluminescence (EL) can be observed from the optical microscope

Table 5. Parameters of some typical heterostructure photodetectors based on WS_2.

Heterostructure	Spectrum range	Responsivity [A W^{-1}]	D^* [Jones]	Speed [s]	Ref.
WS_2-MoS_2	-	2.3 (450 nm)	-	-	[212]
WS_2-MoS_2	-	2340 (532 nm)	4×10^{11}	-	[209]
WS_2-GeSe	270–740 nm	149 (410 nm)	-	3.7×10^{-5}	[208]
WS_2-graphene	340–680 nm	950 (405 nm)	-	≈100	[130]
WS_2-graphene	400–689 nm	10^6 (625 nm)	3.8×10^{11}	4.4×10^{-4}	[213]
WS_2-$CH_3NH_3PbI_3$	-	17 (505 nm)	2×10^{12}	7.5×10^{-3}	[218]
WS_2-ZnO	340–660 nm	2.42×10^{-3} (340 nm)	-	6	[219]
WS_2-PbS	-	14 (808 nm)	3.9×10^{8}	2.3×10^{-4}	[220]
WS_2-Si	340–1100 nm	5.7 (660 nm)	-	6.7×10^{-4}	[84]

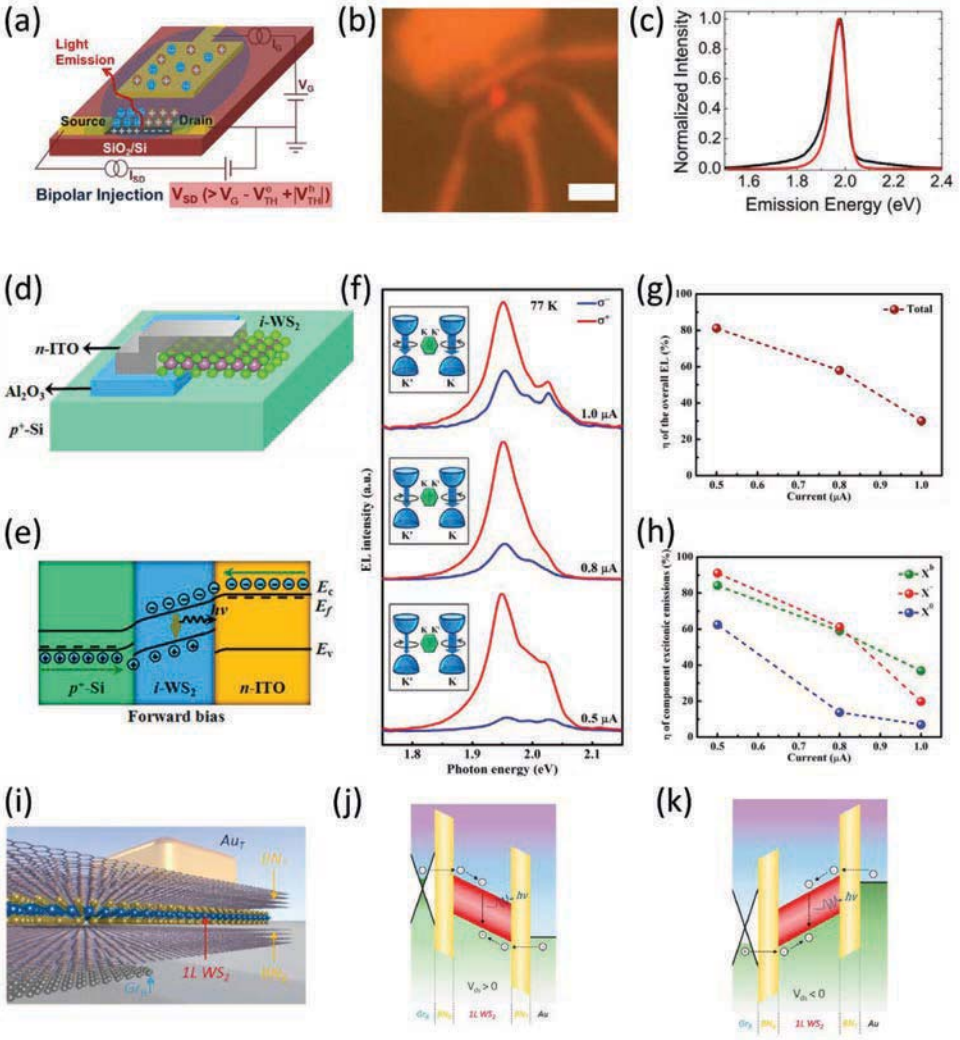

Figure 27. WS_2-based LEDs. a) Schematic of the ionic liquid gated bipolar LED. b) Optical microscope image of the LED device. The red spot is the light emission spot. c) Normalized EL and PL spectra. Black: PL, Red: EL. d) Schematic of the p-i-n LED. e) Schematic of the band alignment under forward bias. f) EL spectra under different driven currents at 77 K. g) Polarization degree of the total EL as a function of current. h) Polarization degrees of exciton (X^0), trion (X^-), and defects-related bound exciton (X^b) as a function of current. i) Schematic of an asymmetry LED structure. j) Band alignment under positive bias. k) Band alignment under negative bias. a–c) Reproduced with permission.[226] Copyright 2014, American Chemical Society. d–h) Reproduced with permission.[227] Copyright 2016, American Chemical Society. i–k) Reproduced with permission.[28] Copyright 2019, American Chemical Society.

image (the red point in Figure 27b). It is clear that EL spectrum of monolayer WS_2 coincides with the PL spectrum (Figure 27c). Furthermore, bilayer WS_2 shows very weak EL as compared with the single-layer WS_2, indicating the indirect band gap of bilayer WS_2. However, ionic gating is not suitable for the large-scale device fabrication since this device structure requires additional energy consumption. In addition, the space charge distribution resulted from the electrostatic doping is usually inhomogenous.[227] At the same time, the p-i-n structure is usually used for organic LEDs, which can also be used for WS_2-based LEDs.[227,228] Yang et al. adopted the p-i-n structure for the fabrication of WS_2-based LEDs (Figure 27d).[227] In their work, indium tin oxide (ITO) is used as the n-type material, p^+-doped Si is used as the p-type material, and single-layer WS_2 is functioned as the intrinsic material, forming a p^+-Si/i-WS_2/n-ITO heterostructure. The EL emission occurs within the region in the vicinity of ITO electrode. As shown in Figure 27e, under forward bias, the holes from p^+-Si are injected into the monolayer WS_2. The barrier, originating from the difference of electron affinities and band gaps of WS_2 and Si, would block the injected holes from leaking into the n-ITO region. Similarly, electrons are injected from n-ITO into monolayer WS_2. The injected electrons and holes give rise to efficient radiation recombination in the monolayer WS_2, leading to light emission. Furthermore, the EL spectra exhibit the current-dependent circular polarization (Figure 27f). The degree of circular polarization is defined as $\eta = [I(\sigma^+) - I(\sigma^-)]/[I(\sigma^+) + I(\sigma^-)]$, where $I(\sigma^+)$

and $I(\sigma^-)$ are the integrated intensities of σ^+ and σ^- circularly polarized EL components, respectively. The η value of the entire EL spectrum decreases with the increasing driven current (Figure 27g), whereas the η values of exciton (X^0), trion (X^-), and defects related bound exciton (X^b) components also decrease with the increasing driven current (Figure 27h). The degree of circular polarization of the total EL is very high (81%) at the low driven current of 0.5 μA, indicating the promising applications for valley photonics. The origin of the current-dependent polarization EL is attributed to the different electron–hole overlap at the K and K' valleys induced by the built-in potential associated with carrier injections and the presence of valley-polarized 2D electron gas because of carrier injections.[229,230] Due to the easy tuning of the Fermi level of graphene by electrostatic gating, Shen et al. designed an asymmetric structure by stacking monolayer WS_2, graphene and BN to fabricate LEDs (Figure 27i).[28] With this special structure, both positive and negative bias can lead to light emission (Figure 27j,k).

4.3.3. Lasers

Both passive mode-locking and Q switching fiber lasers have attracted interest in both industry and scientific research.[231] The most popular schemes for such pulsed lasers is the use of saturable absorbers (SAs). Although the band gap of WS_2 is larger than the optical communication band, it still shows the excellent saturable absorption in that band (**Figure 28**a).[232–234] The possible reasons for the saturable absorption for photons below the band gap of WS_2 are defect-induced band gap reduction and coexistence of semiconducting and metallic states.[232,235,236] The most common setup for mode-locking and Q switching fiber lasers with WS_2 SAs is shown in Figure 28b. The laser cavity consists of a gain fiber (such as Er-doped fiber) and a standard single mode fiber. A pump light is injected into the cavity via a wavelength division multiplexer. The cavity birefringence is adjusted by two polarization controllers. By tuning the birefringence in the laser cavity, the wavelength position of the spectral loss can be varied so that the loss of Q-switching or mode locking can be tuned. As a result, Q-switching or mode-locking lasers can be realized.[237] The repetition rate of the pulsed laser in mode-locking operation is determined by the cavity length, whereas the repetition ratio of the Q-switching pulse is determined by pump power (Figure 28c).[238] For mode-locking mode, using different gain fibers, the pulsed laser operated at different wavelengths are achieved, such as 1.06,[235] 1.55,[232] and 1.91 μm.[234] In addition, WS_2 SAs can be used to generate dark solitons in Er-doped fiber lasers as demonstrated by Liu et al.[239] The generated dark solitons have a center wavelength of 1530 nm (Figure 28d) with a repetition rate of 116.5 Hz. Furthermore, the pulsed laser shows the good signal-to-noise ratio, which is better than 94 dB. Recently, Du et al. found that the graphene-WS_2 heterostructure showed the better performance than WS_2 acting as SA for the mode-locking laser.[233] The pulse duration of graphene-WS_2 SA-based pulsed laser is 660 fs (Figure 28e), which is smaller than that of WS_2 SA-based pulsed laser (Figure 28f). Q-switching lasers based on WS_2 SAs also exhibit the excellent performance.[240–242] For instance, Wang et al. reported that Q-switching pulsed laser with WS_2 SA had a pulse of 430 ns, a pulse energy of 5.4 μJ, and a repetition rate from 64 to 90 kHz operating at 1.9 μm.[240] All these results indicate that WS_2 is an attractive material for good SAs and has promising applications in pulsed lasers.

Except serving as a saturable absorber in pulsed lasers, 2D WS_2 can also act as a gain medium in lasers. Since monolayer WS_2 is a semiconductor with direct band gap and strong excitonic features, the exciton in monolayer WS_2 can allow the formation of long-lived population inversion, which leads to optical gain and possible stimulated emissions.[243] The first report on monolayer WS_2-based excitonic laser was reported by Ye et al.[243] For single-layer TMD-based lasers, high optical

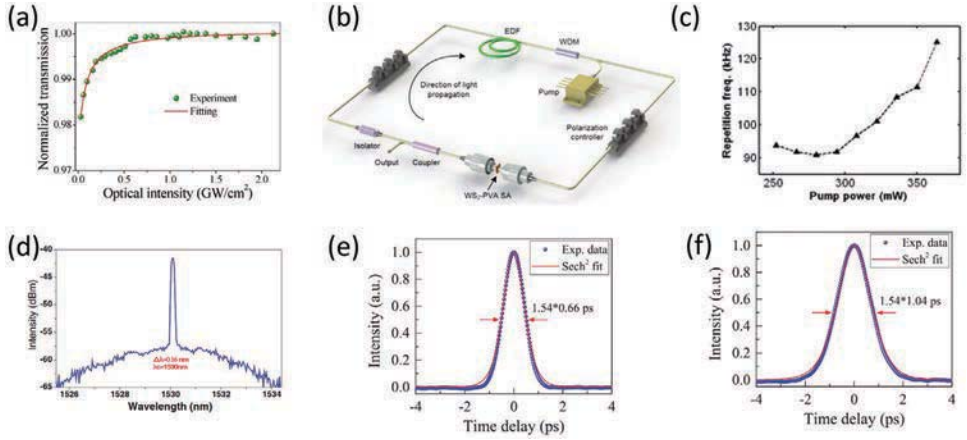

Figure 28. Pulsed lasers based on WS_2. a) Normalized transmission of WS_2 saturable absorbers (SA). b) Typical setup for passive Q-switching and mode-locking pulsed lasers. c) Repetition frequency as a function of pump power for the Q-switching laser. d) Dark soliton spectrum of the mode-locking laser. e,f) Autocorrection trace of the mode-locked pulses for graphene-WS_2 and WS_2 SA-based lasers, respectively. a) Reproduced with permission.[232] Copyright 2015, Springer Nature. b,c) Reproduced with permission.[237] Copyright 2015, Optical Society of America. d) Reproduced with permission.[239] Copyright 2016, Chinese Laser Press. e,f) Reproduced with permission.[233] Copyright 2020, Optical Society of America.

mode confinement and high-quality factor (Q) microcavities is crucial.[244,245] This way, WS_2 is embedded between two dielectric layers (i.e., Si_3N_4/WS_2/hydrogen silsequioxane), forming a micro-disk cavity. Due to the strong light confinement and large modal gain, lasing can be achieved at 10 K with an emission line at 612.2 nm when the device is optically pumped with an ultrafast laser at 473 nm. The low temperature operation of the laser is not suitable for practical applications whereas the room temperature operation is highly desired. Shang et al. achieved the room-temperature low-threshold lasing from monolayer WS_2 activated vertical-cavity surface emitting laser.[246] The structure of the laser is shown in **Figure 29**a. Dielectric oxides are used to fabricate the half-wavelength-thick cavity and distributed Bragg reflectors. Monolayer WS_2 is embedded in the center of the cavity as the gain medium. The cavity photon mode locates at 639.5 nm with a width of 1.0 ± 0.2 nm, indicating a typical Q value of ≈640. Once the device is pumped by a continuous-wave 532 nm laser, lasing at 637.5 nm is achieved for the pumping power density exceeding 6 nW. The typical emission spectrum is depicted in Figure 29b. In addition, the lasing emission is mainly from the cavity surface from the z-direction-dependent light intensity obtained from confocal PL measurements (Figure 29c,d). In order to increase the active region and the lasing beam quality, Ge et al. designed the photonic crystal surface-emitting laser (PCSEL) cavity.[247] The schematic of the PCSEL cavity is illustrated in Figure 29e. Monolayer WS_2 is directly transferred onto the cavity surface as shown in the inset of Figure 29e. The fundamental cavity mode of the cavity locates at 637 nm with a linewidth of 0.25, corresponding to a Q value of 2500. Under optical pumping (450 nm), the transition from spontaneous emission to lasing can be obviously observed from the light-in light-out curve (Figure 29f). The resonant peak locates at 637 nm and the linewidth narrows down to 0.2–0.3 above 144 W cm^{-2} of the pump power density (Figure 29f). Due to the PCSEL structure, the emission is surface-normal emission in the far field (Figure 29g). Although much progresses have been made, the realization of compact and electrically pumped laser is still a big challenge.

4.3.4. Optical Modulators

As demonstrated above, the optical refractive index of 2D WS_2 can be tuned by electrical gating even at the optical communication band. Datta et al. utilized this property to fabricate a phase modulator based on single-layer WS_2.[56] A Mach–Zehnder interferometer (MZI) structure is used for the phase modulator. A capacitor of TMD-HfO_2-ITO is formed on the SiN waveguide. It is found that only the phase of TE mode, of which the electrical field is in plane with WS_2, can be adjusted. With applied voltage on one arm of the MZI, the interference pattern at the MZI output is changed. The modulation efficiency ($V_\pi L$)

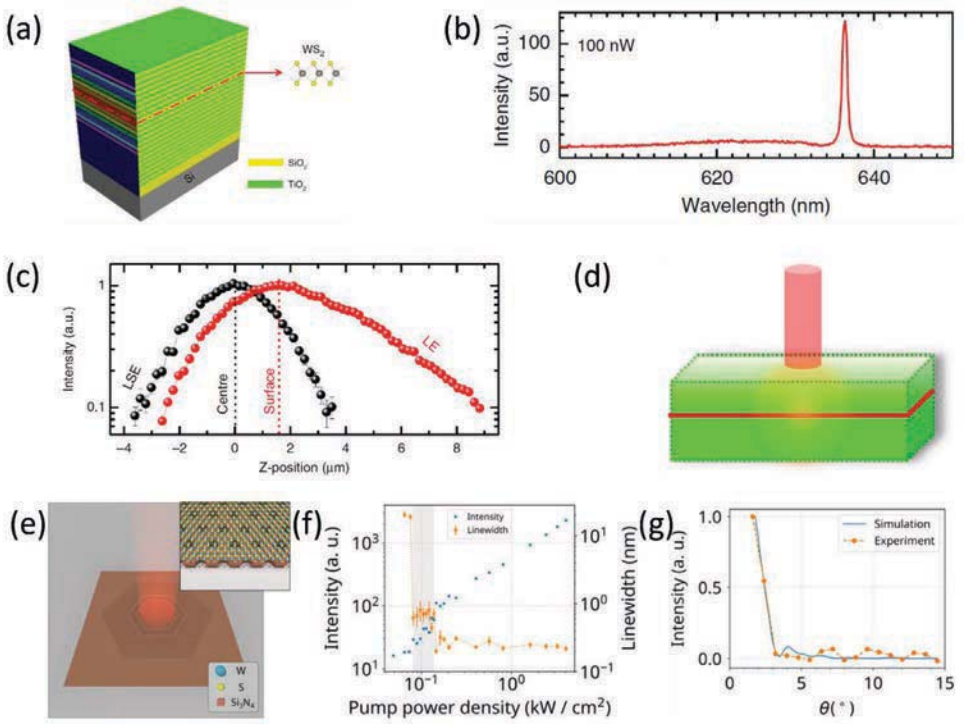

Figure 29. Lasers based on monolayer WS_2. a) Schematic of the 2D semiconductor-embedded microcavity on the SiO_2/Si substrate. b) PL spectrum with an excitation power of 100 nW. c) Normalized integrated intensities of the lasing emission (LE) and the leaked spontaneous emission band (LSE) at various Z-positions. d) Schematic of the emission. e) Schematic of the PCSEL cavity with surface-normal emission from the active region. The insets show the cross-section view of the WS_2 integrated cavity. f) Light-in light-out curve. g) Simulated and measured emission profile depending on the collection angle of θ. a–d) Reproduced with permission.[246] Copyright 2017, Springer Nature. e–g) Reproduced with permission.[247] Copyright 2019, Springer Nature.

of the phase modulator is estimated to be 1.33 V cm. Importantly, the modulator performance can be further enhanced by capping the arm with high-index SU-8 photoresist, leading to increased optical mode overlap with monolayer WS_2. As a result, the change of refractive index of the composite waveguide increases and the modulation efficiency reduces to 0.8 V cm. In this case, the modulation efficiency already outperforms state-of-the-art $LiNbO_3$ modulators with $V_\pi L$ in the range of 1.8–2.4 V cm.[248,249] In addition, the modulation efficiency can as well be increased by reducing the dielectric thickness and embedding the monolayer WS_2 within the waveguide mode.[56]

5. Summary and Outlook

In summary, the comprehensive review on the fundamental properties, wafer-scale synthesis methods, and various kinds of electronic and optoelectronic applications of 2D WS_2 have been presented in a systematic and thorough approach. This review does not only serve as a design guideline to enhance and elevate the material quality of 2D WS_2 films via enhanced synthesis approaches, but also provides valuable insights to various strategies to improve their device performances. Even though there has been some progress achieved in the area of synthesis and device applications, there are still significant challenges and opportunities for the further development of the synthesis methods of WS_2 and devices.

At first, the vast practical applications require the reliable production methods of 2D WS_2. However, wafer-scale synthesis of high-quality 2D WS_2 with controlled thickness is still a big hurdle. At the moment, large-area monolayer WS_2 film can be readily obtained by different CVD methods. But, the quality of these CVD grown WS_2 films is still not sufficient for industrial deployment. Wafer-scale single-layer WS_2 merged from large single domain flakes with aligned orientation is highly desired. Despite the thickness of WS_2 can be roughly controlled by the seed layer sulfurization technique, MOCVD or ALD, the required film uniformity for large-scale devices is not yet achieved. Also, the domain size obtained from those methods is small, restricting the carrier mobility of WS_2. Therefore, the deep understanding of growth behaviors of WS_2 is urgently needed, especially to develop a strictly layer-by-layer growth scheme with the large single-crystal domain size.

Second, high temperature is always needed for the synthesis of high-quality WS_2 films, where this required temperature is not necessarily compatible with the standard COMS technology. In this case, it is essential to develop low temperature synthesis techniques or effective process schemes to transfer WS_2 from growth substrates to target substrates. Although there have been low temperature synthesis methods developed, such as ALD, the quality of obtained 2D WS_2 is regrettably poor, which is not suitable for most of the device applications. Fortunately, transferring high-quality WS_2 from growth substrates to target substrates is feasible at present. Among various established transfer methods, the dry transfer method is preferred due to the little damage and contamination resulted to the 2D materials.[250] Nevertheless, the effectiveness of this particular method is highly depended on the adhesive force between substrates and 2D materials.[251] The strong interaction between WS_2 films and substrates is vital for the transfer of high-quality WS_2.[127] Thus, developing effective, nondestructive, and contamination-free transfer methods is critical.

Third, the effective contact scheme between metal electrodes and 2D WS_2 films is not maturely developed, where the reliable electrical contact is important for all device applications. Until now, there are several contact schemes explored for reducing the contact resistance between metal electrodes and WS_2 channels. It is still a challenge to achieve reliable and ohmic contact for WS_2 devices. Developing a versatile and universal electrical contact scheme is a must.

Moreover, although the light–matter interaction of 2D WS_2 is strong, the light absorption is inevitably low owing to its atomic thickness, restricting its photodetection performance. The incorporation of plasmonic and/or photonic structures can enhance the light absorption of WS_2 device with improved photodetection performance. Nonetheless, the enhanced spectrum range is limited arising from the characteristics of corresponding plasmonic and/or photonic structures. Introducing defects to induce photoconductive gain would also lead to enhanced photodetection. But the response speed becomes low and the response with light intensity becomes nonlinear, which is not beneficial for practical applications. New device structures have to be investigated to substantially elevate the photoresponsivity with wider spectrum and faster response.

The research of 2D WS_2 for applications in memristors, LEDs, lasers, optical modulators, and other optoelectronic devices is indeed in their infancy. Based on the existing findings, it is evident that 2D WS_2 materials have the bright potentials for next-generation high-performance electronics and optoelectronics. More works are urgently needed to be done in order to develop WS_2 toward practical applications with enhanced functionalities in the near future.

Acknowledgements

This work was supported by the National Key Research and Development Program of China (no. 2019YFB2203504), Innovation Research Groups of the National Natural Science Foundation of China (grant no. 61421002), the National Natural Science Foundation of China (grant nos. 61475030, 61605024, 61775031, and 61975024), Fundamental Research Funds for the Central Universities (ZYGX2018J056), UESTC Foundation for the Academic Newcomers Award, the Open Fund of Wuhan National Laboratory for Optoelectronics (2018WNLOKF013), the General Research Fund (CityU 11204618), and the Theme-based Research (T42-103/16-N) of the Research Grants Council of Hong Kong SAR, China.

Conflict of Interest

The authors declare no conflict of interest.

Keywords

chemical vapor deposition, electronics, optoelectronics, synthesis, WS_2

Received: June 29, 2020
Revised: August 5, 2020
Published online: September 11, 2020

[1] K. S. Novoselov, A. K. Geim, S. V. Morozov, D. Jiang, Y. Zhang, S. V. Dubonos, I. V. Grigorieva, A. A. Firsov, *Science* **2004**, *306*, 666.
[2] S. Z. Butler, S. M. Hollen, L. Cao, Y. Cui, J. A. Gupta, H. R. Gutiérrez, T. F. Heinz, S. S. Hong, J. Huang, A. F. Ismach, *ACS Nano* **2013**, *7*, 2898.
[3] M. Chhowalla, H. S. Shin, G. Eda, L.-J. Li, K. P. Loh, H. Zhang, *Nat. Chem.* **2013**, *5*, 263.
[4] V. K. Sangwan, M. C. Hersam, *Ann. Rev. Phys. Chem.* **2018**, *69*, 299.
[5] Q. H. Wang, K. Kalantar-Zadeh, A. Kis, J. N. Coleman, M. S. Strano, *Nat. Nanotechnol.* **2012**, *7*, 699.
[6] H. Huang, B. Jiang, X. Zou, X. Zhao, L. Liao, *Sci. Bull.* **2019**, *64*, 1067.
[7] F. Zhao, Y. Feng, Y. Wang, X. Zhang, X. Liang, Z. Li, F. Zhang, T. Wang, J. Gong, W. Feng, *Nat. Commun.* **2020**, *11*, 1443.
[8] F. Zhao, Y. Wang, X. Zhang, X. Liang, F. Zhang, L. Wang, Y. Li, Y. Feng, W. Feng, *Carbon* **2020**, *161*, 287.
[9] P. Zhang, F. Zhao, P. Long, Y. Wang, Y. Yue, X. Liu, Y. Feng, R. Li, W. Hu, Y. Li, W. Feng, *Nanoscale* **2018**, *10*, 15989.
[10] Z. Li, Z. W. Liu, Z. Li, T. X. Wang, F. Zhao, X. Ding, W. Feng, B. H. Han, *Adv. Funct. Mater.* **2020**, *30*, 1909267.
[11] N. Mounet, M. Gibertini, P. Schwaller, D. Campi, A. Merkys, A. Marrazzo, T. Sohier, I. E. Castelli, A. Cepellotti, G. Pizzi, *Nat. Nanotechnol.* **2018**, *13*, 246.
[12] X. Du, I. Skachko, A. Barker, E. Y. Andrei, *Nat. Nanotechnol.* **2008**, *3*, 491.
[13] K. I. Bolotin, K. J. Sikes, Z. Jiang, M. Klima, G. Fudenberg, J. Hone, P. Kim, H. Stormer, *Solid State Commun.* **2008**, *146*, 351.
[14] R. R. Nair, P. Blake, A. N. Grigorenko, K. S. Novoselov, T. J. Booth, T. Stauber, N. M. Peres, A. K. Geim, *Science* **2008**, *320*, 1308.
[15] K. F. Mak, M. Y. Sfeir, Y. Wu, C. H. Lui, J. A. Misewich, T. F. Heinz, *Phys. Rev. Lett.* **2008**, *101*, 196405.
[16] C. Lee, X. Wei, J. W. Kysar, J. Hone, *Science* **2008**, *321*, 385.
[17] F. Liu, P. Ming, J. Li, *Phys. Rev. B* **2007**, *76*, 064120.
[18] F. Xia, T. Mueller, Y.-M. Lin, A. Valdes-Garcia, P. Avouris, *Nat. Nanotechnol.* **2009**, *4*, 839.
[19] S. Manzeli, D. Ovchinnikov, D. Pasquier, O. V. Yazyev, A. Kis, *Nat. Rev. Mater.* **2017**, *2*, 17033.
[20] B. Liu, A. Abbas, C. Zhou, *Adv. Electron. Mater.* **2017**, *3*, 1700045.
[21] J. R. Schaibley, H. Yu, G. Clark, P. Rivera, J. S. Ross, K. L. Seyler, W. Yao, X. Xu, *Nat. Rev. Mater.* **2016**, *1*, 16055.
[22] W. Zhang, Z. Huang, W. Zhang, Y. Li, *Nano Res.* **2014**, *7*, 1731.
[23] Z. Ye, T. Cao, K. O'brien, H. Zhu, X. Yin, Y. Wang, S. G. Louie, X. Zhang, *Nature* **2014**, *513*, 214.
[24] Z. Y. Zhu, Y. C. Cheng, U. Schwingenschlögl, *Phys. Rev. B* **2011**, *84*, 153402.
[25] W. Zhao, Z. Ghorannevis, L. Chu, M. Toh, C. Kloc, P.-H. Tan, G. Eda, *ACS Nano* **2013**, *7*, 791.
[26] J. Kumar, M. A. Kuroda, M. Z. Bellus, S.-J. Han, H.-Y. Chiu, *Appl. Phys. Lett.* **2015**, *106*, 123508.
[27] Y. Fan, Y. Zhou, X. Wang, H. Tan, Y. Rong, J. H. Warner, *Adv. Opt. Mater.* **2016**, *4*, 1573.
[28] Y. Sheng, T. Chen, Y. Lu, R.-J. Chang, S. Sinha, J. H. Warner, *ACS Nano* **2019**, *13*, 4530.
[29] W. Schutte, J. De Boer, F. Jellinek, *J. Solid State Chem.* **1987**, *70*, 207.
[30] A. V. Kolobov, J. Tominaga, *Two-Dimensional Transition-Metal Dichalcogenides*, Springer Nature, Switzerland **2016**.
[31] A. Klein, S. Tiefenbacher, V. Eyert, C. Pettenkofer, W. Jaegermann, *Phys. Rev. B* **2001**, *64*, 205416.
[32] H. Zeng, G.-B. Liu, J. Dai, Y. Yan, B. Zhu, R. He, L. Xie, S. Xu, X. Chen, W. Yao, *Sci. Rep.* **2013**, *3*, 1608.
[33] W. S. Yun, S. Han, S. C. Hong, I. G. Kim, J. Lee, *Phys. Rev. B* **2012**, *85*, 033305.
[34] E. Cappelluti, R. Roldán, J. Silva-Guillén, P. Ordejón, F. Guinea, *Phys. Rev. B* **2013**, *88*, 075409.
[35] G.-B. Liu, D. Xiao, Y. Yao, X. Xu, W. Yao, *Chem. Soc. Rev.* **2015**, *44*, 2643.
[36] D. W. Latzke, W. Zhang, A. Suslu, T.-R. Chang, H. Lin, H.-T. Jeng, S. Tongay, J. Wu, A. Bansil, A. Lanzara, *Phys. Rev. B* **2015**, *91*, 235202.
[37] I. Tanabe, M. Gomez, W. C. Coley, D. Le, E. M. Echeverria, G. Stecklein, V. Kandyba, S. K. Balijepalli, V. Klee, A. E. Nguyen, *Appl. Phys. Lett.* **2016**, *108*, 252103.
[38] B. Zhu, H. Zeng, J. Dai, Z. Gong, X. Cui, *Proc. Natl. Acad. Sci. U. S. A.* **2014**, *111*, 11606.
[39] J. Xiao, M. Zhao, Y. Wang, X. Zhang, *Nanophotonics* **2017**, *6*, 1309.
[40] J. Shang, X. Shen, C. Cong, N. Peimyoo, B. Cao, M. Eginligil, T. Yu, *ACS Nano* **2015**, *9*, 647.
[41] M. D. Tran, J.-H. Kim, Y. H. Lee, *Curr. Appl. Phys.* **2016**, *16*, 1159.
[42] Y. Wang, C. Cong, W. Yang, J. Shang, N. Peimyoo, Y. Chen, J. Kang, J. Wang, W. Huang, T. Yu, *Nano Res.* **2015**, *8*, 2562.
[43] L. Wang, A. Kutana, B. I. Yakobson, *Ann. Phys.* **2014**, *526*, L7.
[44] T. C. Berkelbach, M. S. Hybertsen, D. R. Reichman, *Phys. Rev. B* **2013**, *88*, 045318.
[45] A. Chernikov, T. C. Berkelbach, H. M. Hill, A. Rigosi, Y. Li, O. B. Aslan, D. R. Reichman, M. S. Hybertsen, T. F. Heinz, *Phys. Rev. Lett.* **2014**, *113*, 076802.
[46] C. Sourisseau, F. Cruege, M. Fouassier, M. Alba, *Chem. Phys.* **1991**, *150*, 281.
[47] A. Berkdemir, H. R. Gutiérrez, A. R. Botello-Méndez, N. Perea-López, A. L. Elías, C.-I. Chia, B. Wang, V. H. Crespi, F. López-Urías, J.-C. Charlier, *Sci. Rep.* **2013**, *3*, 1755.
[48] C. Cong, J. Shang, X. Wu, B. Cao, N. Peimyoo, C. Qiu, L. Sun, T. Yu, *Adv. Opt. Mater.* **2014**, *2*, 131.
[49] C. Lan, Z. Zhou, Z. Zhou, C. Li, L. Shu, L. Shen, D. Li, R. Dong, S. Yip, J. C. Ho, *Nano Res.* **2018**, *11*, 3371.
[50] W. Zhao, Z. Ghorannevis, K. K. Amara, J. R. Pang, M. Toh, X. Zhang, C. Kloc, P. H. Tan, G. Eda, *Nanoscale* **2013**, *5*, 9677.
[51] G. Lucovsky, R. White, J. Benda, J. Revelli, *Phys. Rev. B* **1973**, *7*, 3859.
[52] H. M. Khalil, M. F. Khan, J. Eom, H. Noh, *ACS Appl. Mater. Interfaces* **2015**, *7*, 23589.
[53] M. W. Iqbal, M. Z. Iqbal, M. F. Khan, M. A. Kamran, A. Majid, T. Alharbi, J. Eom, *RSC Adv.* **2016**, *6*, 24675.
[54] N. Peimyoo, W. Yang, J. Shang, X. Shen, Y. Wang, T. Yu, *ACS Nano* **2014**, *8*, 11320.
[55] Y. Yu, Y. Yu, L. Huang, H. Peng, L. Xiong, L. Cao, *Nano Lett.* **2017**, *17*, 3613.
[56] I. Datta, S. H. Chae, G. R. Bhatt, M. A. Tadayon, B. Li, Y. Yu, C. Park, J. Park, L. Cao, D. Basov, *Nat. Photonics* **2020**, *14*, 256.
[57] L. Britnell, R. Ribeiro, A. Eckmann, R. Jalil, B. Belle, A. Mishchenko, Y.-J. Kim, R. Gorbachev, T. Georgiou, S. Morozov, *Science* **2013**, *340*, 1311.
[58] M. Bernardi, M. Palummo, J. C. Grossman, *Nano Lett.* **2013**, *13*, 3664.
[59] Y. Li, A. Chernikov, X. Zhang, A. Rigosi, H. M. Hill, A. M. Van Der Zande, D. A. Chenet, E.-M. Shih, J. Hone, T. F. Heinz, *Phys. Rev. B* **2014**, *90*, 205422.
[60] Z. Jin, X. Li, J. T. Mullen, K. W. Kim, *Phys. Rev. B* **2014**, *90*, 045422.
[61] H. Li, J. K. Huang, Y. Shi, L. J. Li, *Adv. Mater. Interfaces* **2019**, *6*, 1900220.
[62] Y. Zhang, Y. Yao, M. G. Sendeku, L. Yin, X. Zhan, F. Wang, Z. Wang, J. He, *Adv. Mater.* **2019**, *31*, 1901694.
[63] J. R. Brent, N. Savjani, P. O'Brien, *Prog. Mater. Sci.* **2017**, *89*, 411.
[64] M. Samadi, N. Sarikhani, M. Zirak, H. Zhang, H.-L. Zhang, A. Z. Moshfegh, *Nanoscale Horiz.* **2018**, *3*, 90.
[65] J. Yu, X. Hu, H. Li, X. Zhou, T. Zhai, *J. Mater. Chem. C* **2018**, *6*, 4627.
[66] L. Huang, Y. Yu, C. Li, L. Cao, *J. Phys. Chem. C* **2013**, *117*, 6469.
[67] J. D. Cain, F. Shi, J. Wu, V. P. Dravid, *ACS Nano* **2016**, *10*, 5440.

[68] X. Zhang, T. H. Choudhury, M. Chubarov, Y. Xiang, B. Jariwala, F. Zhang, N. Alem, G.-C. Wang, J. A. Robinson, J. M. Redwing, *Nano Lett.* **2018**, *18*, 1049.
[69] A. Aljarb, Z. Cao, H.-L. Tang, J.-K. Huang, M. Li, W. Hu, L. Cavallo, L.-J. Li, *ACS Nano* **2017**, *11*, 9215.
[70] Y. Gao, Z. Liu, D.-M. Sun, L. Huang, L.-P. Ma, L.-C. Yin, T. Ma, Z. Zhang, X.-L. Ma, L.-M. Peng, *Nat. Commun.* **2015**, *6*, 8569.
[71] S. Jo, J.-W. Jung, J. Baik, J.-W. Kang, I.-K. Park, T.-S. Bae, H.-S. Chung, C.-H. Cho, *Nanoscale* **2019**, *11*, 8706.
[72] Z.-Q. Xu, Y. Zhang, S. Lin, C. Zheng, Y. L. Zhong, X. Xia, Z. Li, P. J. Sophia, M. S. Fuhrer, Y.-B. Cheng, *ACS Nano* **2015**, *9*, 6178.
[73] X. Zhang, H. Nan, S. Xiao, X. Wan, X. Gu, A. Du, Z. Ni, K. K. Ostrikov, *Nat. Commun.* **2019**, *10*, 598.
[74] A. L. Elías, N. Perea-López, A. Castro-Beltrán, A. Berkdemir, R. Lv, S. Feng, A. D. Long, T. Hayashi, Y. A. Kim, M. Endo, *ACS Nano* **2013**, *7*, 5235.
[75] R. Xiao, C. Lan, Y. Li, C. Zeng, T. He, S. Wang, C. Li, Y. Yin, Y. Liu, *Adv. Mater. Interfaces* **2019**, *6*, 1901304.
[76] N. Perea-López, A. L. Elías, A. Berkdemir, A. Castro-Beltran, H. R. Gutiérrez, S. Feng, R. Lv, T. Hayashi, F. López-Urías, S. Ghosh, *Adv. Funct. Mater.* **2013**, *23*, 5511.
[77] P. K. Chow, E. Singh, B. C. Viana, J. Gao, J. Luo, J. Li, Z. Lin, A. L. Elias, Y. Shi, Z. Wang, *ACS Nano* **2015**, *9*, 3023.
[78] H. R. Gutiérrez, N. Perea-López, A. L. Elías, A. Berkdemir, B. Wang, R. Lv, F. López-Urías, V. H. Crespi, H. Terrones, M. Terrones, *Nano Lett.* **2013**, *13*, 3447.
[79] Z. Mutlu, M. Ozkan, C. S. Ozkan, *Mater. Chem. Phys.* **2016**, *176*, 52.
[80] C. M. Orofeo, S. Suzuki, Y. Sekine, H. Hibino, *Appl. Phys. Lett.* **2014**, *105*, 083112.
[81] S. Hussain, M. F. Khan, M. A. Shehzad, D. Vikraman, M. Z. Iqbal, D.-C. Choi, W. Song, K.-S. An, Y. Seo, J. Eom, *J. Mater. Chem. C* **2016**, *4*, 7846.
[82] Y. Jung, J. Shen, Y. Liu, J. M. Woods, Y. Sun, J. J. Cha, *Nano Lett.* **2014**, *14*, 6842.
[83] H. Guo, C. Lan, Z. Zhou, P. Sun, D. Wei, C. Li, *Nanoscale* **2017**, *9*, 6246.
[84] C. Lan, C. Li, S. Wang, T. He, T. Jiao, D. Wei, W. Jing, L. Li, Y. Liu, *ACS Appl. Mater. Interfaces* **2016**, *8*, 18375.
[85] J. L. Verble, T. J. Wietling, P. R. Reed, *Solid State Commun.* **1972**, *11*, 941.
[86] J.-G. Song, J. Park, W. Lee, T. Choi, H. Jung, C. W. Lee, S.-H. Hwang, J. M. Myoung, J.-H. Jung, S.-H. Kim, *ACS Nano* **2013**, *7*, 11333.
[87] W. Zeng, L.-P. Feng, J. Su, H.-X. Pan, Z.-T. Liu, *J. Alloys Compd.* **2018**, *745*, 834.
[88] Y.-H. Lee, L. Yu, H. Wang, W. Fang, X. Ling, Y. Shi, C.-T. Lin, J.-K. Huang, M.-T. Chang, C.-S. Chang, *Nano Lett.* **2013**, *13*, 1852.
[89] K. C. Kwon, C. Kim, Q. V. Le, S. Gim, J.-M. Jeon, J. Y. Ham, J.-L. Lee, H. W. Jang, S. Y. Kim, *ACS Nano* **2015**, *9*, 4146.
[90] O. A. Abbas, I. Zeimpekis, H. Wang, A. H. Lewis, N. P. Sessions, M. Ebert, N. Aspiotis, C.-C. Huang, D. Hewak, S. Mailis, *Sci. Rep.* **2020**, *10*, 1696.
[91] Y. Chen, L. Gan, H. Li, Y. Ma, T. Zhai, *Adv. Mater.* **2017**, *29*, 1603550.
[92] S. H. Choi, S. Boandoh, Y. H. Lee, J. S. Lee, J.-H. Park, S. M. Kim, W. Yang, K. K. Kim, *ACS Appl. Mater. Interfaces* **2017**, *9*, 43021.
[93] S. H. Choi, C. S. Oh, S. Boandoh, W. Yang, S. M. Kim, K. K. Kim, *Appl. Sci. Convergence Technol.* **2019**, *28*, 60.
[94] H. Cun, M. Macha, H. Kim, K. Liu, Y. Zhao, T. LaGrange, A. Kis, A. Radenovic, *Nano Res.* **2019**, *12*, 2646.
[95] Z. Qin, L. Loh, J. Wang, X. Xu, Q. Zhang, B. Haas, C. Alvarez, H. Okuno, J. Z. Yong, T. Schultz, *ACS Nano* **2019**, *13*, 10768.
[96] T. Zhang, K. Fujisawa, F. Zhang, M. Liu, M. C. Lucking, R. N. Gontijo, Y. Lei, H. Liu, K. Crust, T. Granzier-Nakajima, *ACS Nano* **2020**, *14*, 4326.
[97] J. S. Lee, S. H. Choi, S. J. Yun, Y. I. Kim, S. Boandoh, J.-H. Park, B. G. Shin, H. Ko, S. H. Lee, Y.-M. Kim, *Science* **2018**, *362*, 817.
[98] Q. Cao, Y.-W. Dai, J. Xu, L. Chen, H. Zhu, Q.-Q. Sun, D. W. Zhang, *ACS Appl. Mater. Interfaces* **2017**, *9*, 18215.
[99] K. Kang, S. Xie, L. Huang, Y. Han, P. Y. Huang, K. F. Mak, C.-J. Kim, D. Muller, J. Park, *Nature* **2015**, *520*, 656.
[100] A. Grundmann, D. Andrzejewski, T. Kümmell, G. Bacher, M. Heuken, H. Kalisch, A. Vescan, *MRS Adv.* **2019**, *4*, 593.
[101] T. H. Choudhury, H. Simchi, R. L. Boichot, M. Chubarov, S. E. Mohney, J. M. Redwing, *Cryst. Growth Des.* **2018**, *18*, 4357.
[102] M. Leskelä, M. Mattinen, M. Ritala, *J. Vac. Sci. Technol., B: Microelectron. Nanometer Struct.* **2019**, *37*, 030801.
[103] A. Delabie, M. Caymax, B. Groven, M. Heyne, K. Haesevoets, J. Meersschaut, T. Nuytten, H. Bender, T. Conard, P. Verdonck, *Chem. Commun.* **2015**, *51*, 15692.
[104] B. Groven, A. Nalin Mehta, H. Bender, J. Meersschaut, T. Nuytten, P. Verdonck, T. Conard, Q. Smets, T. Schram, B. Schoenaers, *Chem. Mater.* **2018**, *30*, 7648.
[105] B. Groven, M. Heyne, A. Nalin Mehta, H. Bender, T. Nuytten, J. Meersschaut, T. Conard, P. Verdonck, S. Van Elshocht, W. Vandervorst, *Chem. Mater.* **2017**, *29*, 2927.
[106] B. Groven, A. N. Mehta, H. Bender, Q. Smets, J. Meersschaut, A. Franquet, T. Conard, T. Nuytten, P. Verdonck, W. Vandervorst, *J. Vac. Sci. Technol., A* **2018**, *36*, 01A105.
[107] M. H. Heyne, J.-F. de Marneffe, T. Nuytten, J. Meersschaut, T. Conard, M. Caymax, I. Radu, A. Delabie, E. C. Neyts, S. De Gendt, *J. Mater. Chem. C* **2018**, *6*, 4122.
[108] J. Park, W. Lee, T. Choi, S.-H. Hwang, J. M. Myoung, J.-H. Jung, S.-H. Kim, H. Kim, *Nanoscale* **2015**, *7*, 1308.
[109] H. Kim, D. Ovchinnikov, D. Deiana, D. Unuchek, A. Kis, *Nano Lett.* **2017**, *17*, 5056.
[110] M. Okada, N. Okada, W.-H. Chang, T. Endo, A. Ando, T. Shimizu, T. Kubo, Y. Miyata, T. Irisawa, *Sci. Rep.* **2019**, *9*, 17678.
[111] T. Irisawa, N. Okada, W. Mizubayashi, T. Mori, W.-H. Chang, K. Koga, A. Ando, K. Endo, S. Sasaki, T. Endo, *IEEE J. Electron Devices Soc.* **2018**, *6*, 1159.
[112] L. Tang, T. Li, Y. Luo, S. Feng, Z. Cai, H. Zhang, B. Liu, H.-M. Cheng, *ACS Nano* **2020**, *14*, 4646.
[113] N. Peimyoo, J. Shang, C. Cong, X. Shen, X. Wu, E. K. Yeow, T. Yu, *ACS Nano* **2013**, *7*, 10985.
[114] F. Lan, R. Yang, S. Hao, B. Zhou, K. Sun, H. Cheng, S. Zhang, L. Li, L. Jin, *Appl. Surf. Sci.* **2020**, *504*, 144378.
[115] Y. Sheng, H. Tan, X. Wang, J. H. Warner, *Chem. Mater.* **2017**, *29*, 4904.
[116] T. He, Y. Li, Z. Zhou, C. Zeng, L. Qiao, C. Lan, Y. Yin, C. Li, Y. Liu, *2D Mater.* **2019**, *6*, 025030.
[117] Y. Zhou, S. G. Sarwat, G. S. Jung, M. J. Buehler, H. Bhaskaran, J. H. Warner, *ACS Appl. Mater. Interfaces* **2019**, *11*, 10189.
[118] Z. Jia, J. Dong, L. Liu, J. Xiang, A. Nie, F. Wen, C. Mu, B. Wang, K. Zhai, Z. Yu, *Appl. Phys. Lett.* **2019**, *115*, 163104.
[119] Y. H. Lee, X. Q. Zhang, W. Zhang, M. T. Chang, C. T. Lin, K. D. Chang, Y. C. Yu, J. T. W. Wang, C. S. Chang, L. J. Li, *Adv. Mater.* **2012**, *24*, 2320.
[120] X. Ling, Y.-H. Lee, Y. Lin, W. Fang, L. Yu, M. S. Dresselhaus, J. Kong, *Nano Lett.* **2014**, *14*, 464.
[121] P. Yang, A.-G. Yang, L. Chen, J. Chen, Y. Zhang, H. Wang, L. Hu, R.-J. Zhang, R. Liu, X.-P. Qu, *Nano Res.* **2019**, *12*, 823.
[122] C. Lan, C. Li, Y. Yin, Y. Liu, *Nanoscale* **2015**, *7*, 5974.
[123] J. Liang, L. Zhang, X. Li, B. Pan, T. Luo, D. Liu, C. Zou, N. Liu, Y. Hu, K. Yang, *Nano Res.* **2019**, *12*, 2802.
[124] A. Patsha, V. Sheff, A. Ismach, *Nanoscale* **2019**, *11*, 22493.
[125] Y. Zhang, Y. Zhang, Q. Ji, J. Ju, H. Yuan, J. Shi, T. Gao, D. Ma, M. Liu, Y. Chen, *ACS Nano* **2013**, *7*, 8963.
[126] C. Lan, X. Kang, R. Wei, Y. Meng, S. Yip, H. Zhang, J. C. Ho, *ACS Appl. Mater. Interfaces* **2019**, *11*, 35238.

[127] H. G. Ji, Y.-C. Lin, K. Nagashio, M. Maruyama, P. Solís-Fernández, A. Sukma Aji, V. Panchal, S. Okada, K. Suenaga, H. Ago, *Chem. Mater.* **2018**, *30*, 403.
[128] Y. Kobayashi, S. Sasaki, S. Mori, H. Hibino, Z. Liu, K. Watanabe, T. Taniguchi, K. Suenaga, Y. Maniwa, Y. Miyata, *ACS Nano* **2015**, *9*, 4056.
[129] G. Bianco, M. Losurdo, M. Giangregorio, A. Sacchetti, P. Prete, N. Lovergine, P. Capezzuto, G. Bruno, *RSC Adv.* **2015**, *5*, 98700.
[130] C. Lan, C. Li, S. Wang, T. He, Z. Zhou, D. Wei, H. Guo, H. Yang, Y. Liu, *J. Mater. Chem. C* **2017**, *5*, 1494.
[131] F. Fabbri, F. Dinelli, S. Forti, L. Sementa, S. Pace, G. Piccinini, A. Fortunelli, C. Coletti, P. Pingue, *J. Phys. Chem. C* **2020**, *124*, 9035.
[132] H. Büch, A. Rossi, S. Forti, D. Convertino, V. Tozzini, C. Coletti, *Nano Res.* **2018**, *11*, 5946.
[133] M. Okada, T. Sawazaki, K. Watanabe, T. Taniguch, H. Hibino, H. Shinohara, R. Kitaura, *ACS Nano* **2014**, *8*, 8273.
[134] S. J. Yun, S. H. Chae, H. Kim, J. C. Park, J.-H. Park, G. H. Han, J. S. Lee, S. M. Kim, H. M. Oh, J. Seok, *ACS Nano* **2015**, *9*, 5510.
[135] S. Li, S. Wang, D.-M. Tang, W. Zhao, H. Xu, L. Chu, Y. Bando, D. Golberg, G. Eda, *Appl. Mater. Today* **2015**, *1*, 60.
[136] J. Zhou, J. Lin, X. Huang, Y. Zhou, Y. Chen, J. Xia, H. Wang, Y. Xie, H. Yu, J. Lei, *Nature* **2018**, *556*, 355.
[137] F. Reale, P. Palczynski, I. Amit, G. F. Jones, J. D. Mehew, A. Bacon, N. Ni, P. C. Sherrell, S. Agnoli, M. F. Craciun, *Sci. Rep.* **2017**, *7*, 14911.
[138] P. Yang, X. Zou, Z. Zhang, M. Hong, J. Shi, S. Chen, J. Shu, L. Zhao, S. Jiang, X. Zhou, *Nat. Commun.* **2018**, *9*, 979.
[139] C. Liu, X. Xu, L. Qiu, M. Wu, R. Qiao, L. Wang, J. Wang, J. Niu, J. Liang, X. Zhou, *Nat. Chem.* **2019**, *11*, 730.
[140] Y. Rong, Y. Fan, A. L. Koh, A. W. Robertson, K. He, S. Wang, H. Tan, R. Sinclair, J. H. Warner, *Nanoscale* **2014**, *6*, 12096.
[141] Y. Yue, J. Chen, Y. Zhang, S. Ding, F. Zhao, Y. Wang, D. Zhang, R. Li, H. Dong, W. Hu, Y. Feng, W. Feng, *ACS Appl. Mater. Interfaces* **2018**, *10*, 22435.
[142] A. Zafar, Z. Zafar, W. Zhao, J. Jiang, Y. Zhang, Y. Chen, J. Lu, Z. Ni, *Adv. Funct. Mater.* **2019**, *29*, 1809261.
[143] J. Gao, Y. D. Kim, L. Liang, J. C. Idrobo, P. Chow, J. Tan, B. Li, L. Li, B. G. Sumpter, T. M. Lu, *Adv. Mater.* **2016**, *28*, 9735.
[144] Y. Jin, Z. Zeng, Z. Xu, Y.-C. Lin, K. Bi, G. Shao, T. S. Hu, S. Wang, S. Li, K. Suenaga, *Chem. Mater.* **2019**, *31*, 3534.
[145] E. Schellkes, X. Hong, M. Holz, U. Huniar, R. Ahlrichs, W. Freyland, *Phys. Chem. Chem. Phys.* **2003**, *5*, 5536.
[146] L.-P. Feng, W.-Z. Jiang, J. Su, L.-Q. Zhou, Z.-T. Liu, *Nanoscale* **2016**, *8*, 6507.
[147] Y. Yue, Y. Feng, J. Chen, D. Zhang, W. Feng, *J. Mater. Chem. C* **2017**, *5*, 5887.
[148] S. Susarla, A. Kutana, J. A. Hachtel, V. Kochat, A. Apte, R. Vajtai, J. C. Idrobo, B. I. Yakobson, C. S. Tiwary, P. M. Ajayan, *Adv. Mater.* **2017**, *29*, 1702457.
[149] F. Wang, Z. Wang, C. Jiang, L. Yin, R. Cheng, X. Zhan, K. Xu, F. Wang, Y. Zhang, J. He, *Small* **2017**, *13*, 1604298.
[150] M. Chhowalla, D. Jena, H. Zhang, *Nat. Rev. Mater.* **2016**, *1*, 16052.
[151] Y. K. Hong, N. Liu, D. Yin, S. Hong, D. H. Kim, S. Kim, W. Choi, Y. Yoon, *J. Phys. D: Appl. Phys.* **2017**, *50*, 164001.
[152] K.-T. Chen, S.-T. Chang, *Vacuum* **2017**, *140*, 172.
[153] L. Liu, S. B. Kumar, Y. Ouyang, J. Guo, *IEEE Trans. Electron Devices* **2011**, *58*, 3042.
[154] W. Sik Hwang, M. Remskar, R. Yan, V. Protasenko, K. Tahy, S. Doo Chae, P. Zhao, A. Konar, H. Xing, A. Seabaugh, *Appl. Phys. Lett.* **2012**, *101*, 013107.
[155] D. Ovchinnikov, A. Allain, Y.-S. Huang, D. Dumcenco, A. Kis, *ACS Nano* **2014**, *8*, 8174.
[156] X. Liu, J. Hu, C. Yue, N. Della Fera, Y. Ling, Z. Mao, J. Wei, *ACS Nano* **2014**, *8*, 10396.
[157] C. Zhou, W. Yang, H. Zhu, *J. Chem. Phys.* **2015**, *142*, 214704.
[158] Y. Cui, R. Xin, Z. Yu, Y. Pan, Z. Y. Ong, X. Wei, J. Wang, H. Nan, Z. Ni, Y. Wu, *Adv. Mater.* **2015**, *27*, 5230.
[159] J. Jiang, Q. Zhang, A. Wang, Y. Zhang, F. Meng, C. Zhang, X. Feng, Y. Feng, L. Gu, H. Liu, *Small* **2019**, *15*, 1901791.
[160] Z. Yu, Y. Pan, Y. Shen, Z. Wang, Z.-Y. Ong, T. Xu, R. Xin, L. Pan, B. Wang, L. Sun, *Nat. Commun.* **2014**, *5*, 5290.
[161] S. Ghatak, A. N. Pal, A. Ghosh, *ACS Nano* **2011**, *5*, 7707.
[162] C. R. Dean, A. F. Young, I. Meric, C. Lee, L. Wang, S. Sorgenfrei, K. Watanabe, T. Taniguchi, P. Kim, K. L. Shepard, *Nat. Nanotechnol.* **2010**, *5*, 722.
[163] M. W. Iqbal, M. Z. Iqbal, X. Jin, J. Eom, C. Hwang, *J. Mater. Chem. C* **2014**, *2*, 7776.
[164] F. Withers, T. H. Bointon, D. C. Hudson, M. F. Craciun, S. Russo, *Sci. Rep.* **2015**, *4*, 4967.
[165] M. W. Iqbal, M. Z. Iqbal, M. F. Khan, M. A. Shehzad, Y. Seo, J. H. Park, C. Hwang, J. Eom, *Sci. Rep.* **2015**, *5*, 10699.
[166] A. Allain, J. Kang, K. Banerjee, A. Kis, *Nat. Mater.* **2015**, *14*, 1195.
[167] K. Liu, P. Luo, W. Han, S. Yang, S. Zhou, H. Li, T. Zhai, *Sci. Bull.* **2019**, *64*, 1426.
[168] D. S. Schulman, A. J. Arnold, S. Das, *Chem. Soc. Rev.* **2018**, *47*, 3037.
[169] Y. Zhao, K. Xu, F. Pan, C. Zhou, F. Zhou, Y. Chai, *Adv. Funct. Mater.* **2017**, *27*, 1603484.
[170] Y. J. Kim, W. Park, J. H. Yang, Y. Kim, B. H. Lee, *IEEE J. Electron Devices Soc.* **2017**, *6*, 164.
[171] A. S. Aji, P. Solís-Fernández, H. G. Ji, K. Fukuda, H. Ago, *Adv. Funct. Mater.* **2017**, *27*, 1703448.
[172] L. Yang, K. Majumdar, H. Liu, Y. Du, H. Wu, M. Hatzistergos, P. Hung, R. Tieckelmann, W. Tsai, C. Hobbs, *Nano Lett.* **2014**, *14*, 6275.
[173] M. Liu, S. Wei, S. Shahi, H. N. Jaiswal, P. Paletti, S. Fathipour, M. Remškar, J. Jiao, W. Hwang, F. Yao, *Nanoscale* **2020**, https://doi.org/10.1039/d0nr01573c.
[174] Y. Wang, J. C. Kim, R. J. Wu, J. Martinez, X. Song, J. Yang, F. Zhao, A. Mkhoyan, H. Y. Jeong, M. Chhowalla, *Nature* **2019**, *568*, 70.
[175] Y. Liu, J. Guo, E. Zhu, L. Liao, S.-J. Lee, M. Ding, I. Shakir, V. Gambin, Y. Huang, X. Duan, *Nature* **2018**, *557*, 696.
[176] C. Kim, I. Moon, D. Lee, M. S. Choi, F. Ahmed, S. Nam, Y. Cho, H.-J. Shin, S. Park, W. J. Yoo, *ACS Nano* **2017**, *11*, 1588.
[177] S. Das, H.-Y. Chen, A. V. Penumatcha, J. Appenzeller, *Nano Lett.* **2013**, *13*, 100.
[178] W. Park, Y. Kim, U. Jung, J. H. Yang, C. Cho, Y. J. Kim, S. M. N. Hasan, H. G. Kim, H. B. R. Lee, B. H. Lee, *Adv. Electron. Mater.* **2016**, *2*, 1500278.
[179] S. Lee, A. Tang, S. Aloni, H.-S. Philip Wong, *Nano Lett.* **2016**, *16*, 276.
[180] X. Cui, E.-M. Shih, L. A. Jauregui, S. H. Chae, Y. D. Kim, B. Li, D. Seo, K. Pistunova, J. Yin, J.-H. Park, *Nano Lett.* **2017**, *17*, 4781.
[181] S. Zheng, H. Lu, H. Liu, D. Liu, J. Robertson, *Nanoscale* **2019**, *11*, 4811.
[182] Y. Pak, W. Park, N. Alaal, Y. Kumaresan, S. A. Aravindh, S. Mitra, B. Xin, J.-W. Min, H. Kim, N. Lim, *ACS Appl. Electron. Mater.* **2020**, *2*, 838.
[183] L. Wang, I. Meric, P. Huang, Q. Gao, Y. Gao, H. Tran, T. Taniguchi, K. Watanabe, L. Campos, D. Muller, *Science* **2013**, *342*, 614.
[184] Z. Cheng, Y. Yu, S. Singh, K. Price, S. G. Noyce, Y.-C. Lin, L. Cao, A. D. Franklin, *Nano Lett.* **2019**, *19*, 5077.
[185] M. H. Guimarães, H. Gao, Y. Han, K. Kang, S. Xie, C.-J. Kim, D. A. Muller, D. C. Ralph, J. Park, *ACS Nano* **2016**, *10*, 6392.
[186] Y. Li, Z. Wang, R. Midya, Q. Xia, J. J. Yang, *J. Phys. D: Appl. Phys.* **2018**, *51*, 503002.
[187] C. Tan, Z. Liu, W. Huang, H. Zhang, *Chem. Soc. Rev.* **2015**, *44*, 2615.
[188] L. Zhang, T. Gong, H. Wang, Z. Guo, H. Zhang, *Nanoscale* **2019**, *11*, 12413.

[189] A. Thomas, *J. Phys. D: Appl. Phys.* **2013**, *46*, 093001.
[190] S. Seo, J.-J. Lee, H.-J. Lee, H. W. Lee, S. Oh, J. J. Lee, K. Heo, J.-H. Park, *ACS Appl. Electron. Mater.* **2020**, *2*, 371.
[191] M. Kumar, D. K. Ban, S. M. Kim, J. Kim, C. P. Wong, *Adv. Electron. Mater.* **2019**, *5*, 1900467.
[192] X. Yan, C. Qin, C. Lu, J. Zhao, R. Zhao, D. Ren, Z. Zhou, H. Wang, J. Wang, L. Zhang, *ACS Appl. Mater. Interfaces* **2019**, *11*, 48029.
[193] X. Yan, Q. Zhao, A. P. Chen, J. Zhao, Z. Zhou, J. Wang, H. Wang, L. Zhang, X. Li, Z. Xiao, *Small* **2019**, *15*, 1901423.
[194] M. Long, P. Wang, H. Fang, W. Hu, *Adv. Funct. Mater.* **2019**, *29*, 1803807.
[195] C. Lan, C. Li, Y. Yin, Y. Liu, *Nanoscale* **2015**, *7*, 17980.
[196] C. Lan, D. Li, Z. Zhou, S. Yip, H. Zhang, L. Shu, R. Wei, R. Dong, J. C. Ho, *Small Methods* **2019**, *3*, 1800245.
[197] A. Di Bartolomeo, L. Genovese, F. Giubileo, L. Iemmo, G. Luongo, T. Foller, M. Schleberger, *2D Mater.* **2017**, *5*, 015014.
[198] Z. Yin, H. Li, H. Li, L. Jiang, Y. Shi, Y. Sun, G. Lu, Q. Zhang, X. Chen, H. Zhang, *ACS Nano* **2012**, *6*, 74.
[199] X. Zhou, Q. Zhang, L. Gan, H. Li, T. Zhai, *Adv. Funct. Mater.* **2016**, *26*, 4405.
[200] J. Wang, H. Fang, X. Wang, X. Chen, W. Lu, W. Hu, *Small* **2017**, *13*, 1700894.
[201] H. Fang, W. Hu, *Adv. Sci.* **2017**, *4*, 1700323.
[202] H. Tan, Y. Fan, Y. Zhou, Q. Chen, W. Xu, J. H. Warner, *ACS Nano* **2016**, *10*, 7866.
[203] S. Hwan Lee, D. Lee, W. Sik Hwang, E. Hwang, D. Jena, W. Jong Yoo, *Appl. Phys. Lett.* **2014**, *104*, 193113.
[204] N. Huo, S. Yang, Z. Wei, S.-S. Li, J.-B. Xia, J. Li, *Sci. Rep.* **2015**, *4*, 5209.
[205] J. Yao, Z. Zheng, J. Shao, G. Yang, *Nanoscale* **2015**, *7*, 14974.
[206] L. Zeng, L. Tao, C. Tang, B. Zhou, H. Long, Y. Chai, S. P. Lau, Y. H. Tsang, *Sci. Rep.* **2016**, *6*, 20343.
[207] Y. Liu, Y. Huang, X. Duan, *Nature* **2019**, *567*, 323.
[208] Q. Lv, F. Yan, X. Wei, K. Wang, *Adv. Opt. Mater.* **2018**, *6*, 1700490.
[209] H. Tan, W. Xu, Y. Sheng, C. S. Lau, Y. Fan, Q. Chen, M. Tweedie, X. Wang, Y. Zhou, J. H. Warner, *Adv. Mater.* **2017**, *29*, 1702917.
[210] G. Wang, L. Li, W. Fan, R. Wang, S. Zhou, J. T. Lü, L. Gan, T. Zhai, *Adv. Funct. Mater.* **2018**, *28*, 1800339.
[211] Y. F. Xiong, J. H. Chen, Y. Q. Lu, F. Xu, *Adv. Electron. Mater.* **2019**, *5*, 1800562.
[212] Y. Xue, Y. Zhang, Y. Liu, H. Liu, J. Song, J. Sophia, J. Liu, Z. Xu, Q. Xu, Z. Wang, *ACS Nano* **2016**, *10*, 573.
[213] J. D. Mehew, S. Unal, E. Torres Alonso, G. F. Jones, S. Fadhil Ramadhan, M. F. Craciun, S. Russo, *Adv. Mater.* **2017**, *29*, 1700222.
[214] C. Lan, Z. Zhou, R. Wei, J. C. Ho, *Mater. Today Energy* **2019**, *11*, 61.
[215] C. Xie, C. K. Liu, H. L. Loi, F. Yan, *Adv. Funct. Mater.* **2020**, *30*, 1903907.
[216] C. Lan, R. Dong, Z. Zhou, L. Shu, D. Li, S. Yip, J. C. Ho, *Adv. Mater.* **2017**, *29*, 1702759.
[217] J. Zhou, J. Huang, *Adv. Sci.* **2018**, *5*, 1700256.
[218] C. Ma, Y. Shi, W. Hu, M. H. Chiu, Z. Liu, A. Bera, F. Li, H. Wang, L. J. Li, T. Wu, *Adv. Mater.* **2016**, *28*, 3683.
[219] C. Lan, C. Li, S. Wang, Y. Yin, H. Guo, N. Liu, Y. Liu, *RSC Adv.* **2016**, *6*, 67520.
[220] Y. Yu, Y. Zhang, X. Song, H. Zhang, M. Cao, Y. Che, H. Dai, J. Yang, H. Zhang, J. Yao, *ACS Photonics* **2017**, *4*, 950.
[221] Y. Wang, K. Ding, B. Sun, S.-T. Lee, J. Jie, *Nano Res.* **2016**, *9*, 72.
[222] F. Gong, W. Luo, J. Wang, P. Wang, H. Fang, D. Zheng, N. Guo, J. Wang, M. Luo, J. C. Ho, *Adv. Funct. Mater.* **2016**, *26*, 6084.
[223] S. Butun, E. Palacios, J. D. Cain, Z. Liu, V. P. Dravid, K. Aydin, *ACS Appl. Mater. Interfaces* **2017**, *9*, 15044.
[224] Y. Liu, W. Huang, W. Chen, X. Wang, J. Guo, H. Tian, H. Zhang, Y. Wang, B. Yu, T.-L. Ren, *Appl. Surf. Sci.* **2019**, *481*, 1127.
[225] C.-H. Yeh, H.-C. Chen, H.-C. Lin, Y.-C. Lin, Z.-Y. Liang, M.-Y. Chou, K. Suenaga, P.-W. Chiu, *ACS Nano* **2019**, *13*, 3269.
[226] S. Jo, N. Ubrig, H. Berger, A. B. Kuzmenko, A. F. Morpurgo, *Nano Lett.* **2014**, *14*, 2019.
[227] W. Yang, J. Shang, J. Wang, X. Shen, B. Cao, N. Peimyoo, C. Zou, Y. Chen, Y. Wang, C. Cong, *Nano Lett.* **2016**, *16*, 1560.
[228] D. Andrzejewski, E. Hopmann, M. John, T. Kümmell, G. Bacher, *Nanoscale* **2019**, *11*, 8372.
[229] Y. Zhang, T. Oka, R. Suzuki, J. Ye, Y. Iwasa, *Science* **2014**, *344*, 725.
[230] T. Scrace, Y. Tsai, B. Barman, L. Schweidenback, A. Petrou, G. Kioseoglou, I. Ozfidan, M. Korkusinski, P. Hawrylak, *Nat. Nanotechnol.* **2015**, *10*, 603.
[231] U. Keller, *Nature* **2003**, *424*, 831.
[232] D. Mao, Y. Wang, C. Ma, L. Han, B. Jiang, X. Gan, S. Hua, W. Zhang, T. Mei, J. Zhao, *Sci. Rep.* **2015**, *5*, 7965.
[233] W. Du, H. Li, C. Lan, C. Li, J. Li, Z. Wang, Y. Liu, *Opt. Express* **2020**, *28*, 11514.
[234] H. Yu, X. Zheng, K. Yin, T. Jiang, *Laser Phys.* **2017**, *27*, 015102.
[235] D. Mao, S. Zhang, Y. Wang, X. Gan, W. Zhang, T. Mei, Y. Wang, Y. Wang, H. Zeng, J. Zhao, *Opt. Express* **2015**, *23*, 27509.
[236] H. Zhang, S. Lu, J. Zheng, J. Du, S. Wen, D. Tang, K. Loh, *Opt. Express* **2014**, *22*, 7249.
[237] K. Wu, X. Zhang, J. Wang, X. Li, J. Chen, *Opt. Express* **2015**, *23*, 11453.
[238] R. Khazaeinezhad, T. Nazari, H. Jeong, K. J. Park, B. Y. Kim, D.-I. Yeom, K. Oh, *IEEE Photon. J.* **2015**, *7*, 1503507.
[239] W. Liu, L. Pang, H. Han, Z. Shen, M. Lei, H. Teng, Z. Wei, *Photonics Res.* **2016**, *4*, 111.
[240] X. Wang, J. Xu, S. Gao, Y. Liu, Z. You, C. Tu, *RSC Adv.* **2017**, *7*, 47565.
[241] L. Li, Y. Wang, Z. F. Wang, X. Wang, G. Yang, *Opt. Commun.* **2018**, *406*, 80.
[242] Y. Yang, S. Yang, C. Li, X. Lin, *Opt. Laser Technol.* **2019**, *111*, 571.
[243] Y. Ye, Z. J. Wong, X. Lu, X. Ni, H. Zhu, X. Chen, Y. Wang, X. Zhang, *Nat. Photonics* **2015**, *9*, 733.
[244] S. Wu, S. Buckley, J. R. Schaibley, L. Feng, J. Yan, D. G. Mandrus, F. Hatami, W. Yao, J. Vučković, A. Majumdar, X. Xu, *Nature* **2015**, *520*, 69.
[245] C. Lan, Z. Shi, R. Cao, C. Li, H. Zhang, *Nanoscale* **2020**, *12*, 11784.
[246] J. Shang, C. Cong, Z. Wang, N. Peimyoo, L. Wu, C. Zou, Y. Chen, X. Y. Chin, J. Wang, C. Soci, W. Huang, T. Yu, *Nat. Commun.* **2017**, *8*, 543.
[247] X. Ge, M. Minkov, S. Fan, X. Li, W. Zhou, *npj 2D Mater. Appl.* **2019**, *3*, 16.
[248] C. Wang, M. Zhang, X. Chen, M. Bertrand, A. Shams-Ansari, S. Chandrasekhar, P. Winzer, M. Lončar, *Nature* **2018**, *562*, 101.
[249] C. Wang, M. Zhang, B. Stern, M. Lipson, M. Lončar, *Opt. Express* **2018**, *26*, 1547.
[250] K. Kang, K.-H. Lee, Y. Han, H. Gao, S. Xie, D. A. Muller, J. Park, *Nature* **2017**, *550*, 229.
[251] B. Li, J. Yin, X. Liu, H. Wu, J. Li, X. Li, W. Guo, *Nat. Nanotechnol.* **2019**, *14*, 567.
[252] J. Chen, K. Shao, W. Yang, W. Tang, J. Zhou, Q. He, Y. Wu, C. Zhang, X. Li, X. Yang, *ACS Appl. Mater. Interfaces* **2019**, *11*, 19381.
[253] A. Ramasubramaniam, *Phys. Rev. B* **2012**, *86*, 115409.
[254] B. Zhu, X. Chen, X. Cui, *Sci. Rep.* **2015**, *5*, 9218.
[255] A. Hanbicki, M. Currie, G. Kioseoglou, A. Friedman, B. Jonker, *Solid State Commun.* **2015**, *203*, 16.
[256] T. Chen, Y. Sheng, Y. Zhou, R.-J. Chang, X. Wang, H. Huang, Q. Zhang, L. Hou, J. H. Warner, *ACS Appl. Mater. Interfaces* **2019**, *11*, 6421.

Changyong Lan received his B.S. degree in Applied Physics from the University of Electronic Science and Technology of China (UESTC) in 2007 and his Ph.D. degree in Physics from Nanjing University in 2012. Then, he joined UESTC as a lecturer. From 2016 to 2019, he worked as a post-doctoral researcher in Johnny C. Ho's group at City University of Hong Kong. Currently, he is an associate professor of Optical Engineering at UESTC. His research interests are the controlled synthesis of low-dimensional functional materials and their applications in electronics and optoelectronics.

Chun Li received the Ph.D. degree in Physics from Wuhan University, China, in 2008. After that, he worked at National Institute of Material Science (NIMS, Japan), University of California, San Diego (UCSD, USA), and North Carolina State University (NCSU, USA) as a postdoctoral researcher. In September 2012, he joined the University of Electronic Science and Technology of China (UESTC) as a full professor. His current research interests mainly focus on 2D materials for integrated optoelectronics.

Johnny C. Ho received his B.S. with high honors in Chemical Engineering in 2002 and his M.S. and Ph.D. in Materials Science and Engineering from the University of California, Berkeley, in 2005 and 2009, respectively. From 2009 to 2010, he worked as a post-doctoral research fellow in the nanoscale synthesis and characterization group at Lawrence Livermore National Laboratory, California. Currently, he is a professor of Materials Science and Engineering at City University of Hong Kong. His research interests focus on the synthesis, characterization, integration, and device applications of nanoscale materials for various technological applications, including nano-electronics, sensors, and energy harvesting.